



Miikka Karhu

**ON WELDABILITY OF THICK SECTION
AUSTENITIC STAINLESS STEEL USING
LASER PROCESSES**



Miikka Karhu

ON WELDABILITY OF THICK SECTION AUSTENITIC STAINLESS STEEL USING LASER PROCESSES

Dissertation for the degree of Doctor of Science (Technology) to be presented with due permission for public examination and criticism in the Auditorium 1314 at Lappeenranta-Lahti University of Technology LUT, Lappeenranta, Finland on the 25th of October, 2019, at noon.

Acta Universitatis
Lappeenrantaensis 869

- Supervisors Docent Veli Kujanpää
LUT School of Energy Systems
Lappeenranta-Lahti University of Technology LUT
Finland
- Professor Harri Eskelinen
LUT School of Energy Systems
Lappeenranta-Lahti University of Technology LUT
Finland
- Reviewers Professor Michael Rethmeier
TU Berlin
Bundesanstalt für Materialforschung und –prüfung (BAM)
Germany
- Professor Victor Karkhin
Peter the Great St. Petersburg Polytechnic University
Department of Welding and Laser Technologies
Russia
- Opponents Professor Michael Rethmeier
TU Berlin
Bundesanstalt für Materialforschung und –prüfung (BAM)
Germany
- Professor Jukka Kömi
Materials and Mechanical Engineering, Faculty of Technology
University of Oulu
Finland

ISBN 978-952-335-416-6
ISBN 978-952-335-417-3 (PDF)
ISSN-L 1456-4491
ISSN 1456-4491

Lappeenranta-Lahti University of Technology LUT
LUT University Press 2019

Abstract

Miikka Karhu

On weldability of thick section austenitic stainless steel using laser processes

Lappeenranta 2019

80 pages

Acta Universitatis Lappeenrantaensis 869

Diss. Lappeenranta-Lahti University of Technology LUT

ISBN 978-952-335-416-6, ISBN 978-952-335-417-3 (PDF), ISSN-L 1456-4491, ISSN 1456-4491

Laser welding and its different process variations using filler metal addition have increasingly become the preferred joining technology of the metal structure fabrication industry.

The essential characteristics of laser welding methods enable deep and narrow welds to be produced at high welding speed, which is beneficial for productivity enhancement. However, these inherent process characteristics can cause weldability issues in certain applications. Such challenges include solidification cracking susceptibility of welds produced in thick section joints of rigid constructional arrangements. In keyhole mode laser-arc hybrid multi-pass welding applications, the width of the groove geometry is limited because of the narrow fusion zone produced. In single-side thick section multi-pass welding, this groove width restriction limits the applicability of root pass welding and, consequently, limits maximum usable joint thickness. Moreover, inhomogeneous distribution and mixture of filler metal across the fusion zone has been encountered in deep and narrow single-pass laser-arc hybrid and laser cold-wire welds where an over-alloyed filler metal is needed for alloying purposes. Inhomogeneous filler metal mixing can have an adverse effect on weld metal corrosion resistance and ductility properties, and in certain cases can cause enhanced susceptibility to weld solidification cracking.

The research scope of this article-based doctoral dissertation covers scientific study of welding technology development and improvement of laser-arc hybrid and cold-wire welding of thick section austenitic stainless steels. The research focuses on weldability, in particular, assessment of solidification cracking in multi-pass laser-arc hybrid welding, enhancement of the process capabilities of thick-section welding by defocusing of the laser beam in laser-arc hybrid and cold-wire processes, and study of mixing behavior in thick section laser welding with filler addition, especially improvements to mixing homogeneity as a result of appropriate combinations of groove geometry and process parameters.

The research objective was to develop a self-restraint test set-up and verify whether the set-up is able to provide conditions that promote solidification cracking in multi-pass laser-arc hybrid welding of thick section austenitic stainless steel joints with different groove geometries. A further objective was to develop a defocusing technique for thicker weld joint filling and to investigate how filler metal mixing phenomena change as a result

of different torch orientation, groove geometry, specific defocusing technique and laser welding method, for example, laser arc-hybrid and laser cold-wire processes.

The research methods used comprised experimental investigations, numerical simulation studies and theoretical background studies. The laser types considered in the dissertation are solid-state lasers operating in continuous wave mode and at 1 micrometre wavelength. The welded joint thicknesses studied in the experiments were between 10 mm and 60 mm.

A self-restraint welding test sample set-up was developed to help analysis of solidification cracking susceptibility in multi-pass laser welding. The developed test set-up enables assessment of the weldability of thick-section austenitic stainless steels using laser-arc hybrid multi-pass welding with respect to the base metal chemistry, produced weld geometry, base metal dilution, filler metal selection and overall propensity to weld metal solidification cracking susceptibility. The developed defocusing technique for multi-pass procedures offers a new alternative approach to enhancing efficiency in intermediate-power laser welding of thick sections. The results of the mixing studies provide new knowledge about the mixing behavior of weld metals produced in thick section joints using laser-arc hybrid and laser cold-wire welding. Furthermore, the results produce enhanced understanding of the effect of welding parameters, for example, the effects of filler wire feeding configuration and groove geometry on filler metal mixing homogeneity and distribution intensity throughout the fusion zone of thick section welds.

Keywords: laser arc-hybrid welding, laser cold-wire welding, austenitic stainless steel, thick sections, weldability, solidification cracking, laser beam, defocusing, multi-pass welding, filler metal mixing

Acknowledgements

This dissertation is based on research that was initially carried out by the author while working in research and development projects at the VTT Technical Research Centre of Finland Ltd and Lappeenranta University of Technology between 2007 and 2019. The work presented in the dissertation was completed in the Laboratory of Welding Technology of the Department of Mechanical Engineering at Lappeenranta-Lahti University of Technology LUT, Finland, between 2018 and 2019.

First and foremost, I would like to express my heartfelt gratitude to my supervisors, Professor Emeritus, Docent Veli Kujanpää and Professor Harri Eskelinen, for the guidance, support and encouragement they gave me during the course of my studies and research.

I would like to thank the reviewers of the dissertation, Professor Michael Rethmeier and Professor Victor Karkhin for their time and effort and for all the valuable advice that they gave me.

I would like to thank all my co-workers at the Laboratory of Welding Technology and throughout the Welded Metal Structures unit for the supportive and inspiring working atmosphere in the unit. I want to especially thank my close colleague Esa Hiltunen for his support of my efforts at the Welding Lab. I would also like to thank Professor Antti Salminen for many inspirational discussions about topics related to laser welding.

I would like to express thanks to Pertti Kokko for his help and expertise with the welding experiments, Antti Heikkinen for help with the metallographic preparations and Toni Väkiparta for carrying out the EDS-measurements. I express my appreciation to Peter Jones for his help with the English language. I would like to acknowledge the role of earlier projects, IHYB, ADFAB, Tri-Laser and FiDiPro-Na, and the ongoing DigRob-project of Business Finland for financial support.

Finally, I would like to express my deepest gratitude to my family – especially Mom and Dad, my parents-in-law and my dear wife, Marita, who have always supported me with their love, encouragement and faith in my abilities.

Miikka Karhu

Miikka Karhu
September 2019
Lappeenranta, Finland

Contents

Abstract

Acknowledgements

Contents

List of publications	9
Nomenclature	11
1 Introduction	13
1.1 Research background and motivation	13
1.2 Research problem	14
1.3 Scope and research environment	15
1.4 Objective and research question	16
1.5 Structure of the thesis	17
1.6 Contribution to welding science and welding industry	17
1.7 Research limitations	18
2 Theoretical background	21
2.1 Weldability of metallic materials	21
2.2 Weldability of austenitic stainless steels	23
2.2.1 Solidification cracking of welds	23
2.2.2 The effect of solidification mode and δ -ferrite on solidification cracking	25
2.2.3 Use of weldability diagrams in prediction of solidification cracking susceptibility	29
2.2.4 Modified welding diagrams which take impurity elements into account	32
2.2.5 Effect of high cooling rate and rapid solidification	34
2.2.6 Prevention of weld solidification cracking	37
2.3 Thick section laser welding	38
2.3.1 Single-pass welding	39
2.3.2 Multi-pass welding	44
2.4 Mixing in thick section laser welding	48
2.5 Recognized needs for improvements	54
3 Research materials and methods	55
3.1 Materials	55
3.2 Methods	56
4 Overview of the publications and research findings	61
4.1 Publication I	61

4.2	Publication II.....	62
4.3	Publication III.....	63
4.4	Publication IV.....	64
5	Conclusions	67
6	Suggestions for further study	71
	References	73
	Part II: Publications	81

List of publications

This dissertation is based on the following papers. The rights have been granted by publishers to include the papers in the dissertation.

- I. Karhu, M. and Kujanpää, V. (2011). Solidification cracking studies in multi pass laser hybrid welding of thick section austenitic stainless steel. In: Hot Cracking Phenomena in Welds III, Part II Steels and Stainless Steels, pp. 161-182. Eds. Lippold, J., Boellinghaus, T. and Cross, C., 1st ed., Germany: Springer-Verlag Berlin Heidelberg.
- II. Karhu, M. and Kujanpää, V. (2015). Defocusing techniques for multi-pass laser welding of austenitic stainless steel. *Physics Procedia*, 78, pp. 53-64.
- III. Sohail, M., Karhu, M., Na S-J., Han, S-W. and Kujanpää, V. (2017). Effect of leading and trailing torch configuration on mixing and fluid behavior of laser-gas metal arc hybrid welding. *Journal of Laser Applications*, 29(4), pp. 1-14.
- IV. Karhu, M., Kujanpää, V., Eskelinen, H. and Salminen, A. (2019). Filler metal mixing behaviour of 10 mm thick stainless steel butt-joint welds produced with laser-arc hybrid and laser cold-wire processes. *Applied Sciences*, 9(8), pp. 1-20.

Author's contribution

The author is the principal author and main researcher in papers I, II and IV. In these studies, the author planned the experiments, designed experimental procedures, supervised the welding experiments and carried out analysis of the test results. Scientific supervisor and co-author V. Kujanpää provided valuable suggestions and comments in the planning phase of the work and during writing of the manuscripts. He also participated in responding to the peer-review referees. In paper IV, the other co-authors contributed by reviewing the manuscript.

In paper III, the author is the second author and researcher. The author designed and supervised the welding experiments, participated in writing of the manuscript and analysed the experimental and modelling results together with V. Kujanpää. M. Sohail was the principal author and writer. He conducted the modelling and numerical simulation studies and their analysis together with S-J. Na and S-W. Han.

Nomenclature

Greek alphabet

α	ferrite
γ	austenite

Dimensionless numbers

C_{req}	Chromium equivalent
C_{req}/Ni_{eq}	Chromium / nickel equivalent ratio
Ni_{eq}	Nickel equivalent

Abbreviations

A	Fully austenitic solidification
A-F	Austenitic - Ferritic solidification
AISI	American Iron and Steel Institute
AWS	American Welding Society
CFD	Computational Fluid Dynamics
DDC	Ductility-Dip Cracking
EDS	Energy Dispersive Spectroscopy
F-A-F	Ferritic - Austenitic - Ferritic solidification
F-A	Ferritic - Austenitic solidification
F	Ferritic solidification
FZ	Fusion Zone
GMA	Gas Metal Arc
GMAW	Gas Metal Arc Welding
HAZ	Heat Affected Zone
ISO	International Organization for Standardization
ITER	International Thermonuclear Experimental Reactor
LAHW	Laser-arc hybrid welding
LCW	Laser cold-wire welding
Nd:YAG	Neodymium-doped Yttrium Aluminum Garnet
PA	Flat position used in welding
PF	Vertical up welding position
PG	Vertical down welding position
PMZ	Partial Melted Zone
RT	Room Temperature
SS	Stainless Steel

Symbols

d_f	[μm]	Focused laser spot diameter
d_{fibre}	[μm]	Core diameter of process fibre

D_{LA}	[mm]	Horizontal distance between laser beam and arc/wire tip
F_l	[mm]	Focal length
F_r	[mm]	Length between collimation lenses
G	[°C/mm]	Thermal gradient
GR	[°C/s]	Cooling rate
R	[mm/s]	Growth rate

1 Introduction

Laser welding and its different process variations with filler metal addition, such as laser-arc hybrid welding (LAHW), have increasingly become the preferred joining technology of the metal structure fabrication industry. From the perspective of the medium and heavy section welding industry, in particular, the key benefit that makes laser welding process variants attractive is the ability to use the laser high-energy density beam source to weld thicker sections with one pass and with reduced welding distortion, which can shorten production times and enhance overall manufacturing performance. In spite of the considerable advances that have been achieved, ever-growing competition in the manufacturing sector is acting as a driver for further welding research and development and obliging manufacturers and research institutions to continue exploring new technologies, revise and optimize current process know-how, and through production gains, both quantitative and qualitative, help welding companies remain competitive and profitable.

1.1 Research background and motivation

The research background and motivation for this study originates from research and development work done by the author some years ago. The sub-projects with which the candidate was involved were related to weldability studies of the vacuum vessel of the International Thermonuclear Experimental Reactor (ITER). At the time, weldability studies of the ITER vacuum vessel focused on high energy density beam welding processes. One of the main areas of interest was exploring the potential of laser beam welding techniques as an alternative to narrow-gap gas tungsten arc welding, which is the reference method used in manufacturing and assembly welding of the ITER vacuum vessel. Another important research topic was solidification cracking susceptibility of the austenitic stainless steel construction material of ITER in laser-arc hybrid welding and development of an assessment set-up for cracking studies. (Jones et al., 2003) (Jones et al., 2005) (Karhu and Kujanpää, 2008) (Ahn et al., 2011)

The vacuum vessel of ITER is one of the most critical components in the fusion reactor because its primary function is to provide a high quality vacuum environment for the fusion plasma and simultaneously act as the first confinement barrier from the nuclear safety perspective. The vacuum vessel of ITER is designed as a massive and rigid double-walled torus structure made of 60 mm thick austenitic 316L(N)-IG stainless steel material. The vessel structure weighs about 5200 tons in total and comprises nine 40 degree, 420 ton sectors measuring 13 meters in height and 7 meters in width. The sectors are designed in such a way that they will be assembled and joined together into a ring doughnut-shaped structure with field welding at the construction site. (Koizumi et al., 1998) (Ioki et al., 2012) (Ahn et al., 2011) The ITER-facility is currently under construction in Cadarache in southern France and the assembly phase of the sectors at the construction site is expected to start in autumn 2020 (Arnoux, 2018) (Griffith, 2012). Completion of the field joint welding and testing of the vacuum vessel assembly is

estimated to take four years. It was estimated that the total length of deposited weld metal would arise to 50 kilometres depending on the needed amount of build-up passes and required amount of welding wire would be at least 25 000 kilograms (Dulon, 2015). In view of the magnitude and complexity of the vacuum vessel structure and the stringent fit-up and assembly tolerances, the assembly welding task can be considered a major welding engineering challenge requiring holistic consideration of metallurgical, operative and constructional weldability. (Guirao et al., 2009) (Ioki et al., 2012) (Kim et al., 2013) (Choi et al., 2014)

In recent years, laser-arc hybrid welding has partly achieved maturity and gained acceptance in many areas of industrial fabrication, for instance, shipbuilding and pipeline manufacture (Webster et al., 2008) (Koga et al., 2010) (Kristensen, 2013) (Turichin et al., 2017). In addition, new generation disc and fiber laser sources offer continuous wave (CW) mode for laser or laser-arc hybrid welding at power levels of 10-20 kW and higher (up to 100 kW), enabling greater material thickness, even several tens of millimetres, to be welded in a single pass (Rominger et al., 2015) (Rethmeier et al., 2009) (Katayama et al., 2015). In order to be able to exploit the full potential of such developments, many areas related to laser-arc hybrid and laser welding with filler metal processes require further study. One such area is non-autogenous thick section laser welding, especially in application cases where the resulting weld chemistry needs careful alloying with appropriate filler metal addition in order to improve and ensure the metallurgical quality of the weldments. If an over-alloyed filler metal is needed and the welds produced are deep and narrow, as is usually the case in thick section laser welding, it may be challenging to ensure that the filler metal and its elements are homogeneously mixed and evenly distributed throughout the fusion zone. (Karhu et al., 2013) (Gook et al., 2014) (Gook et al., 2015) (Westin et al., 2011)

1.2 Research problem

Inhomogeneous filler metal mixing can cause unfavourable changes in weld metal chemistry and microstructure, which can lead to inferior mechanical properties, reduced corrosion resistance, or even increased weld solidification cracking susceptibility. Currently, relatively little published information is available that specifically addresses mixing behavior and factors influencing mixing in thick section laser welding with filler addition. In view of the rapid development in available high-power thick section laser technology, scientific research in this area is clearly needed. In addition, there is a continuing need to increase the productivity of thick section welding applications. These aspects and viewpoints form the core of the research problem of this thesis.

1.3 Scope and research environment

The research scope of this thesis covers scientific study of welding technology development and improvement of laser welding of thick section austenitic stainless steels. The specific welding methods considered are laser-gas metal arc (GMA) hybrid welding and laser welding with a cold-wire (LCW). The laser types used in the welding experiments are solid-state lasers operating in continuous wave mode: a neodymium-doped yttrium aluminium garnet (Nd:YAG) laser and an ytterbium fiber laser with a wavelength of 1064 nm and 1070 nm, respectively. Within the scope of this thesis the term thick section denotes the plate thickness of 10 mm and greater. The used plate thicknesses in the experiments were between 10 mm and 60 mm. It should be noted that numerical modelling was utilized as a tool in order to gain understanding of the melt flow behavior of laser-gas metal arc hybrid welding with the help of simulation. For that reason, the addressing of theories behind modelling and numerical simulation in welding and discussion concerning their utilization are left out of the scope of the work.

The scope of the dissertation does not include any modelling and numerical simulation software work by the candidate. The required modelling and numerical simulation work has been carried out by South-Korean research team at Korea Advanced Institute of Science and Technology (KAIST) in the mechanical engineering department under the supervision of the team leader professor Suck-Joo Na.

This article-based dissertation focuses on a number of key areas related to weldability of thick section austenitic stainless steel. Figure 1.1 gives an overview of the research topics of the publications on which the dissertation is based and outlines some important considerations incorporated into the scope of the research.

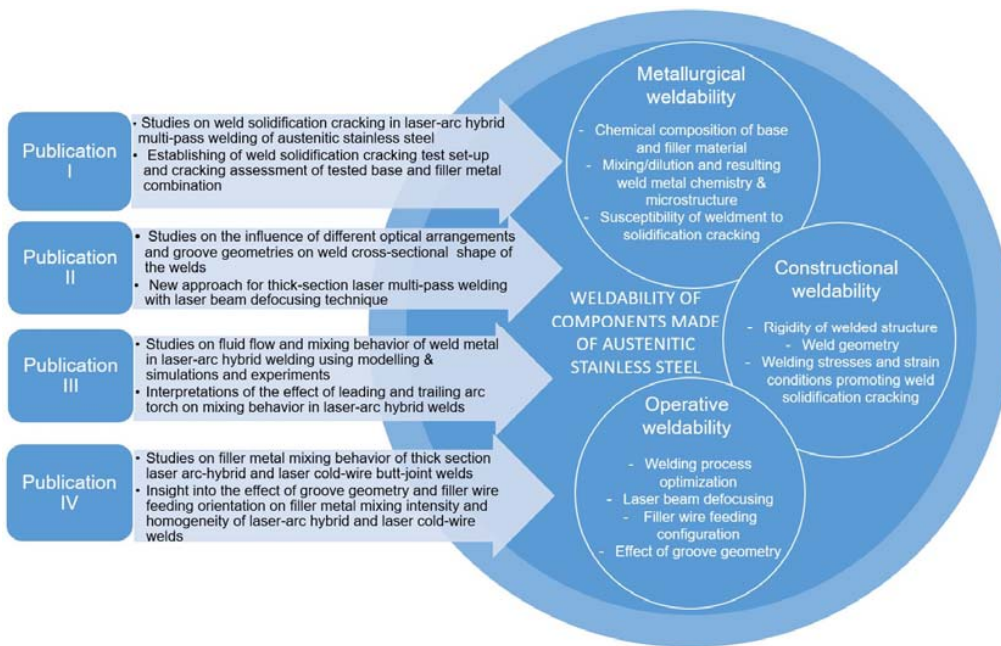


Figure 1.1: Research topics and the main contribution of each publication with respect to the scope of the research.

1.4 Objective and research question

This research produces new scientific information about laser-arc hybrid and laser cold-wire processes used for welding thick austenitic stainless steels and weldability aspects of them. The research objective and research question of the dissertation is presented as follows:

Research objective

Objective is to develop a self-restraint test set-up and verify, if it is able to provide the conditions that promote solidification cracking in multi-pass laser-arc hybrid welding of thick section austenitic stainless steel joints with different groove geometries. This verification was based on the utilization of AISI 316 ITER-grade austenitic stainless steel base material. In addition, the objective is to develop a defocusing technique feasible for thicker weld joint filling and describe how filler metal mixing phenomena changes due to different torch orientation, different groove geometry, specific defocusing technique and different laser welding applications such as laser arc-hybrid and laser cold-wire processes.

Research question

How specific defocusing technique of laser arc-hybrid and laser cold-wire welding together with different torch orientation affects the shape of fusion zones and filler metal mixing with different groove geometries and what kind of test set-up could be used to analyse solidification cracking phenomena in multi-pass laser-arc hybrid welding of thick section austenitic stainless steel joints?

1.5 Structure of the thesis

This doctoral dissertation is based on four peer-reviewed scientific publications. The dissertation consists of two main parts. The first part is divided into the following sections:

Chapter 1 presents an introduction to the research background and the motivation for the work and describes the studied topics within the framework of the research environment. The research problem, research question, scientific contribution and limitations of the scope of the dissertation are also presented in this chapter.

Chapter 2 discusses the theoretical background including, for example, weldability aspects of austenitic stainless steel, process variations of thick section laser welding with filler metal and characteristics relating to weld metal mixing in thick section joints.

Chapter 3 describes the research methods and materials used.

Chapter 4 provides a recap of the research publications included in this dissertation.

Chapter 5 presents the conclusions from the main research results and key findings with respect to the research hypotheses and research questions.

Chapter 6 addresses future work and identifies possible research topics for further exploration and as an extension to the research carried out in this dissertation.

The second part of the dissertation comprises the four scientific publications forming the basis of the dissertation.

1.6 Contribution to welding science and welding industry

This dissertation addresses fundamental issues related to weldability with the aim of development of and improvement to laser welding of thick section austenitic stainless steels. Within the scope of the study, the dissertation makes the following contributions to scientific knowledge in the field:

1) New knowledge appertaining to development of the specific method and a proposal for a self-restraint welding test set-up for assessment of the hot cracking susceptibility of

a base and filler material combination in multi-pass laser-arc hybrid welding; and production of experimental data on the effect of weld bead cross-sectional geometry on weld solidification cracking in laser-arc hybrid multi-pass welds.

2) New knowledge about how to enhance the applicability of 1 micrometre wavelength lasers with laser-arc or laser cold wire based welding processes in thick section welding with the help of the proposed combination of beam defocusing and multi-pass technique.

3) New knowledge about the mixing behavior of weld metal produced in thick section joints in laser-arc hybrid and laser cold-wire welding. Enhanced understanding of the effect of welding parameters, for example, the effects of filler wire feeding configuration and groove geometry on filler metal mixing homogeneity and distribution intensity throughout the fusion zone of thick section welds.

The scientific contributions are of particular relevance to welding procedure development for heavy component fabrication involving thick section welding assemblies. The expected practical benefits of this work can be described as follows:

1) Helping welding fabricators perform assessments and comparisons of weld solidification cracking susceptibility of possible base and filler metal solutions prior to the production phase, for example, in parallel with a pre-production welding test. Moreover, fabricators can use the test set-up to evaluate the weld solidification cracking susceptibility of candidate alloys in response to various welding parameter changes.

2) Enabling new alternative procedures to be implemented for enhancing efficiency in intermediate power laser welding of thick section applications.

3) Supporting understanding of how mixing can be considered in welding parameter planning and filler metal alloy selection for thick section welding with laser-arc or laser cold wire-based processes. Such applications could be, for example, cases where specific crevice corrosion resistant requirements in thick section high molybdenum concentration alloyed austenitic stainless steel weldments need to be guaranteed with proper filler metal mixing. Another example could be welding applications of transition joints, for example, in welding of a dissimilar metal joint between a carbon steel and an austenitic stainless steel.

1.7 Research limitations

The findings and conclusions are limited to the considered welding procedures, laser types and laser wavelengths, and studied base and filler material grades. The laser-arc hybrid experiments were carried out with Nd:YAG laser + gas metal arc welding (GMAW) and fiber laser + GMAW. The laser types used in the experiments operate at 1 micrometre wavelength and the research findings are thus not directly comparable or

directly applicable to lasers operating at other wavelengths, for example, carbon dioxide (CO₂) lasers working at 10 micrometre wavelength. Available resources imposed limits as regards the number of experiments and possible weld sample examinations. Thus, it was only possible to consider flat position (PA) welding and the energy dispersive spectroscopy (EDS) studies of weld cross-sections examined only one transversal cross-section sample per produced test weld joint. In modelling and simulation studies, development of a unified complete modelling solution for the welding process is extremely challenging. The laser-arc hybrid welding process is governed by very complex multi-physical phenomena that are difficult to fully describe numerically because of a lack of comprehensive knowledge of synergistic interactions between the laser and electric arc. Consequently, only rather limited modelling and simulation solutions are available and some simplifications and generalizations have to be used. Nevertheless, the modelling method used in this work can serve as a precursor to more advanced models and development of more sophisticated modelling approaches.

2 Theoretical background

This chapter presents theoretical background from the themes associated with the research topics of this work. The chapter considers especially the following subjects: weldability aspects of austenitic stainless steel, thick section laser welding with filler metal process variations and characteristics relating to weld metal mixing in thick section joints.

2.1 Weldability of metallic materials

Welding can be considered to be one of the important fabrication techniques for metallic materials. In welding engineering, common attributes associated with welded constructions and their weldments are for example adequate strength or fatigue strength, good toughness, resistance against cracking and/or corrosion. From the perspective of materials to be welded, a thorough consideration of materials weldability is usually needed in order to reclaim above attributes. But what aspects term weldability is consisted of and what is meant by if a material possesses good weldability? There has been international standards and national regulatory documents constituted for describing and defining the characteristics of weldability of materials. For example the ISO/TR 581:2005 is pointing out three interrelated factors which are governing the overall weldability. They are metallurgical, operative and constructional weldability (ISO/TR 581:2005, 2005). In Figure 2.1 it can be seen the representation from above factors.

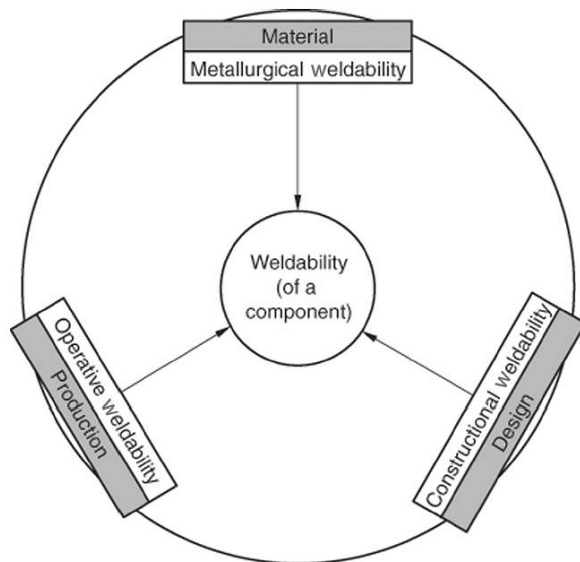


Figure 2.1: Representation of weldability according to ISO/TR 581:2005 (ISO/TR 581:2005, 2005).

Each of the mentioned factors is associated with different attributes. A recap showing some of the main influencing attributes is compiled into Table 2-1.

Table 2-1: Factors associating with weldability and examples of influencing attributes for each factors (ISO/TR 581:2005, 2005).

WELDABILITY of a component		
Metallurgical weldability in material point of view	Constructional weldability in production point of view	Operative weldability in design point of view
a) Chemical composition of material, critical for, e.g. <ul style="list-style-type: none"> - Tendency to hardening - Tendency to hot cracking - Tendency to brittle fracture 	a) Design of the structure, e.g. <ul style="list-style-type: none"> - Distribution of forces - Work piece thickness - Arrangement of welds - Differences in stiffness 	a) Preparation for welding, e.g. <ul style="list-style-type: none"> - Joint type - Shape of joint
b) Metallurgical properties inherited from production methods, e.g. <ul style="list-style-type: none"> - Crystalline structure - Grain size - Segregations - Anisotropy 	b) Condition regarding loading, e.g. <ul style="list-style-type: none"> - Type and magnitude of stresses in the component - Speed of stressing - Effect of corrosion 	b) Welding procedure, including e.g. <ul style="list-style-type: none"> - Welding processes - Types of filler materials - Welding parameters - Welding sequence - Welding positions
c) Physical properties, e.g. <ul style="list-style-type: none"> - Melting point - Thermal conductivity - Strength and toughness 		c) Pre- and post-treatment <ul style="list-style-type: none"> - Preheating - Post weld heat treatment - Mechanical and chemical treatment

As can be noticed the term weldability is a multi-faceted issue, but some attempts have been made to define it in condensed manner. The standard ISO/TR 581:2005 formulates weldability to be as follows: “A component consisting of metallic material is considered to be weldable by a given process when metallic continuity can be obtained by welding using a suitable welding procedure. At the same time, the welds shall comply with the requirements specified in regard to both their metallurgical and mechanical properties and their influence on the construction of which they form a part” (ISO/TR 581:2005, 2005). The American Welding Society (AWS), on the other hand, has given the following definition for weldability: “The capability of material to be welded under the imposed

fabrication conditions into a specific, suitably designed structure and to perform satisfactorily in the intended service” (ANSI/AWS A3.0-89, 1989). Easterling states (Easterling, 1983) that from a practical point of view a material can be said to have a good weldability if it can be reliably welded on a production scale. According to Easterling the term good weldability is a function of four interacting factors: 1) type of welding process, 2) environment, 3) alloy composition and 4) joint design and size. All of the mentioned factors can be decisive together, or on the other hand even if one of them is unsuitable it may lead to detrimental outcome of weldability (Easterling, 1983).

2.2 Weldability of austenitic stainless steels

Austenitic stainless steels are widely used engineering material in a variety of applications because of their corrosion resistance, good ductility and toughness and they are rather easy fabricable. The 300 series alloys designated by American Iron and Steel Institute (AISI), are the most used of the austenitic grades. Most of the 300 series alloys are nominally based on 18Cr-8Ni system with slight modifications or with additional alloying elements. Such example are standard Type 316 (equivalent to for example EN 1.4436 grade) austenitic stainless steels, which have chromium and nickel weight-% levels between 16-18 and 10-14, respectively. To improve pitting corrosion resistance of Type 316 grade, molybdenum with 2-3 weight-% is used as an additional alloying element.

Although the austenitic stainless steel grades are commonly considered to be quite easily weldable, there can be arisen weldability problems if adequate precautions are not taken into account well in advance. Above problems are usually related to loss of corrosion properties or solidification cracking of weldments. (Lippold, 2005)

2.2.1 Solidification cracking of welds

Hot cracking which is also called high temperature cracking are divided sub-types based on the microstructural characteristics they possess. While hot cracking is considered to be a general term, it can be classified into solidification cracking and liquation cracking (Lippold, 2015). According to Lippold (2015) solidification cracking occurs in the fusion zone (FZ) while the liquation cracking typically occurs in the partial melted region (PMZ) of the heat affected zone (HAZ). Lippold (2015) points out that the presence of liquid films along grain boundaries are normally associated with the above-mentioned cracking sub-types. Another sub-species of elevated temperature cracking which takes place in the solid state and may occur in both fusion zone and HAZ is called ductility-dip cracking (DDC). For example, in the case of stainless steels and Ni-base materials, alloys that are susceptible to DDC exhibit a sharp reduction in ductility at the temperature range between 800 °C and 1150 °C upon cooling (Lippold, 2015). Lippold also mentions (Lippold, 2015) that the characteristic for DDC phenomenon in weld metals is that grain boundary liquation is not playing a role in cracking and cracks are always occurring intergranular.

Solidification cracks are considered as weld defect. For example standard SFS-EN ISO 12932 which defines quality levels for imperfections in laser-arc hybrid welding of steels, nickel and nickel alloys, is not permitting cracks in any of the quality levels B, C or D.

In the research work of this dissertation, solidification cracking is under the main interest and that is why other cracking types are intentionally left to less attention. The author likes to bring out that hereafter the terms hot cracking and solidification cracking are equally used in order to designate the same thing.

Solidification cracking occurs at high temperatures where weld metal is in the process of liquid-solid transition. During the last stage of solidification in the transition from liquid to solid state, liquid films are present at grain boundaries in partially liquid, “mushy” region trailing the weld pool. At that stage solid matter consists of dendritic array structure separated by liquid films, Figure 2.2(b). Solidified weld exposes under the stresses because of the used welding heat. Welding heat produced by e.g. arc or beam source induces stresses due to expansion and contraction of welded material. Both heating and cooling sequence could induce expansion and contraction stresses, depending on e.g. degree of constraint, shape and thickness of the work piece to be welded. Stresses for their part induce strains to the welded material and if those stresses and strains rise over the critical value, which exceed the level what solidified partially liquid region can resist, a rupture of liquid film is developed: A solidification crack has formed, Figure 2.2(a) and 2.2(b). Solidification cracks are defects which usually formed in weld centreline and when opened to the surface of the weld, they are distinctively detectable with naked eye. (Kujanpää, 1984) (Kujanpää et al. 1986) (Ploshikhin et al., 2005) (Cross, 2005) (Kurz and Trivedi, 1995)

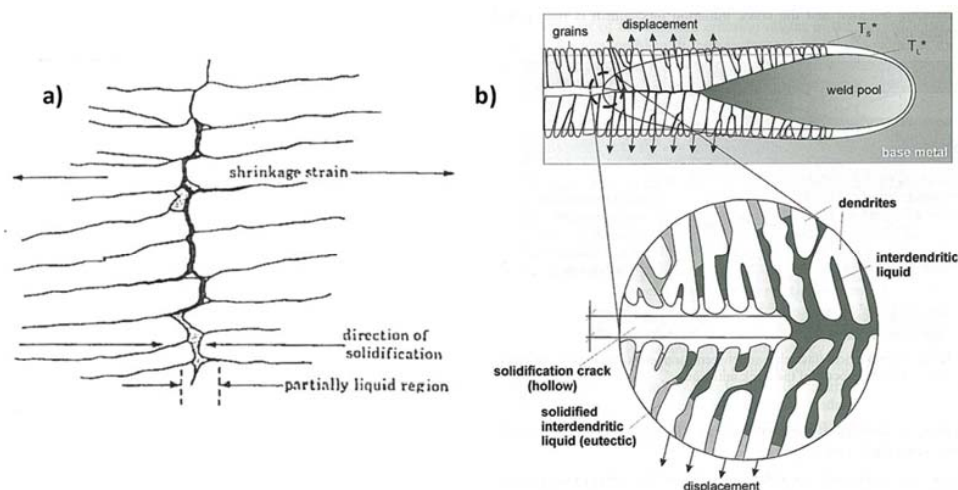


Figure 2.2: Schematic illustration of mechanism of solidification cracking. a) (Baker, 1975); b) (Ploshikhin et al., 2005)

2.2.2 The effect of solidification mode and δ -ferrite on solidification cracking

Solidification mode of austenitic stainless steels is strongly determined by chemical balance of austenite and ferrite forming elements. Ferrite favouring elements are e.g. : Cr, Mo, Si, Nb and Ti. Austenitic favouring elements are e.g. : Ni, Mn, C and N. Solidification modes are named after depending on which order of sequence delta (δ)-ferrite and austenite phase is started to form from the solidifying melt. Solidification modes can be divided in five sub-types which are schematically presented in Figure 2.3 Those types are:

- Fully austenitic solidification (Type A)
- Austenitic - Ferritic solidification (Type A-F)
- Ferritic - Austenitic - Ferritic solidification (Type F-A-F)
- Ferritic - Austenitic solidification (Type F-A)
- Ferritic solidification (Type F)

Types A and A-F is called primary austenitic solidification modes, whereas types F-A-F, F-A and F are called primary ferritic solidification modes.

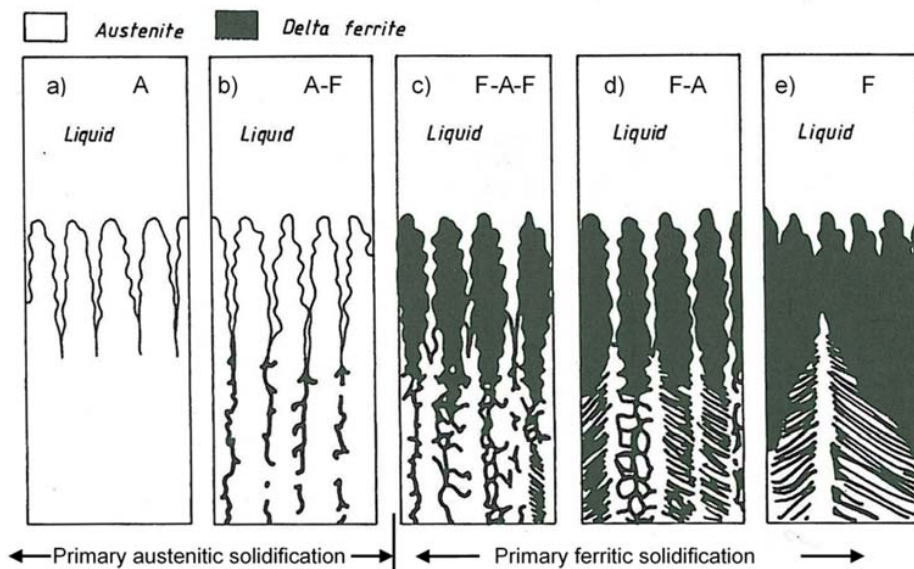


Figure 2.3: Schematic presentation of different solidification modes of austenitic stainless steel weld. (Modified from Suutala and Moisiso, 1980)

Following phase transformations are taken place during cooling and solidification of the above mentioned solidification types. The descriptions from phase transformations below

are from the references of (Suutala, 1982b) (Kujanpää, 1984) (Lippold and Kotecki, 2005).

Type A: Melt solidifies as fully austenitic to the solid state and remains austenitic upon cooling to room temperature. Weld microstructure which is a result from fully austenitic (Type A) solidification is shown in Figure 2.4.

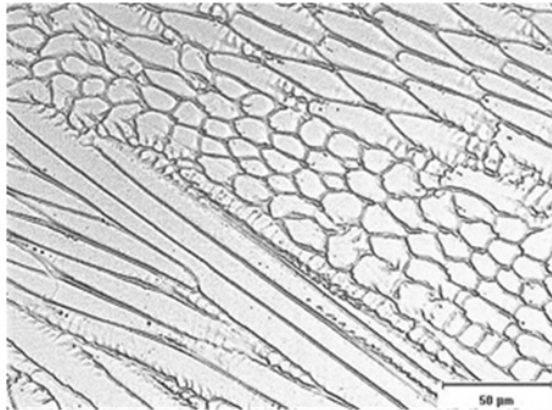


Figure 2.4: Weld microstructure which is a result from fully austenitic (Type A) solidification. (Lippold and Kotecki, 2005)

Type A-F: Austenite is the leading phase and delta ferrite is formed from ferrite promoting remaining melt which has enriched concentration of Cr, Mo and Si elements. Weld microstructure which is a result from austenitic-ferritic (Type A-F) solidification is shown in Figure 2.5.

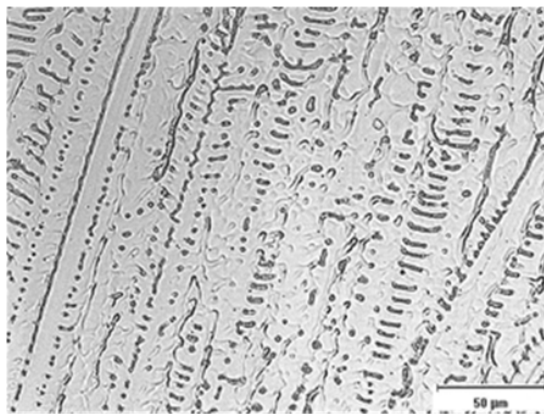


Figure 2.5: Weld microstructure which is a result from austenitic-ferritic (Type A-F) solidification. (Lippold and Kotecki, 2005)

Type F-A-F: Delta ferrite is the leading phase in solidification front and austenite is formed between the ferrite dendrites. At the very terminal phase the solidification of austenite leads to very strong diffusion generated segregation of alloying elements which generates a tiny amount of highly concentrated (Cr, Mo, Si) ferrite.

Type F-A: Delta ferrite solidifies as a leading phase and austenite is formed between the ferrite dendrites. During the cooling, austenite grows into the melt which is resulted in drastic decrease of ferrite content. Weld microstructure which is a result from ferritic-austenitic (Type F-A) solidification is shown in Figure 2.6.



Figure 2.6: Weld microstructure which is a result from ferritic-austenitic- (Type F-A) solidification. Ferrite shows as dark skeletal like morphology. (Lippold and Kotecki, 2005)

Type F: Melt solidifies as a single phase ferrite. Austenite is formed only within the solid state. Austenite nucleates from the grain boundaries of ferrite and grows into the ferrite during the cooling. Weld microstructure which is a result from ferritic (Type F) solidification is shown in Figure 2.7.

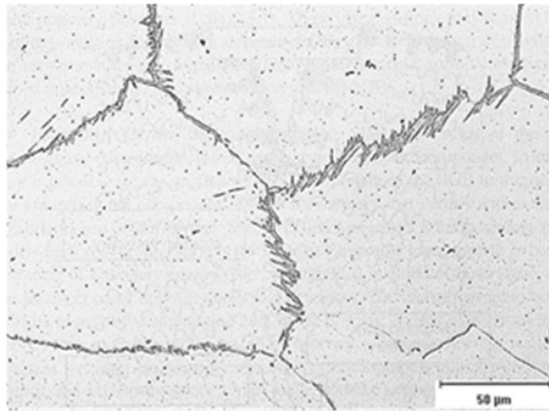


Figure 2.7: Weld microstructure which is a result from ferritic (Type F) solidification. Ferrite grains show lighter whereas austenite shows as dark Wittmanstätten-like structures along ferrite grain boundaries. (Lippold and Kotecki, 2005)

As Figures 2.5-2.7 suggest, the amount of residual delta ferrite which is remained in weld microstructure in room temperature increases when solidification type is shifted from A-type to the utmost F type respectively.

Various research studies have shown that delta ferrite has a beneficial effect on prevention of hot cracking in welding of austenitic stainless steels. E.g. the research results from Hull, showed that 5-10 % ferrite gives very beneficial effect in preventing hot cracking. Moreover, the studies of Hull demonstrated that excessive amount of ferrite is detrimental concerning cracking susceptibility, namely at high ferrite levels (~30%) cracking susceptibility increases again (Hull, 1967). Above mentioned effect of ferrite levels on solidification cracking susceptibility were also confirmed e.g. by Kujanpää et al. (1979), Cieslak et al. (1982) and Brooks et al. (1984).

The beneficial effect of ferrite is generally considered to correlate with the residual ferrite content which is resulted after the weld is cooled to the room temperature. This room temperature (RT) ferrite assumption can be roughly used as a normative base. However, extensive studies have revealed that a beneficial effect is related in existing ferrite content at high temperatures (near liquidus/solidus) rather than in room temperature. Why and how high temperature ferrite is being interacted as a cracking inhibitor? This is tried to interpret by the researchers and at least following three proposals have been met consensus among researchers: 1) Ferrite has higher solubility than austenite for impurities such as sulphur and phosphorous (see Table 2-3 in Section 2.2.4), which restricts the aggregating of these low melting point elements to interdendritic region (see Figure 2.2 in Section 2.2.1) during the primary ferrite solidification. 2) The presence of duplex structure as ferrite (δ) and austenite (γ) grain boundaries are present during A-F and F-A type solidification; δ - γ boundaries are less wetted by liquid films than γ - γ or δ - δ boundaries. 3) In F-A type solidification ferrite-austenite (δ - γ) boundaries form irregular

paths compared to A type solidification, where grain boundaries are much straighter. When weld solidification cracking occurs along the grain boundaries, crack propagation is much difficult to develop in tortuous ferrite-austenite (δ - γ) boundaries than in more planar and straight austenite-austenite (γ - γ) grain boundaries. Above mentioned difference in grain boundary morphology between A type and F-A type is schematically pictured in Figure 2.8. (Hull, 1967) (Matsuda et al., 1979) (Matsuda et al., 1982) (Suutala, 1982b) (Kujanpää, 1984) (Kujanpää et al., 1986) (Brooks et al., 1984) (Brooks and Thompson, 1991) (Lippold and Kotecki, 2005)

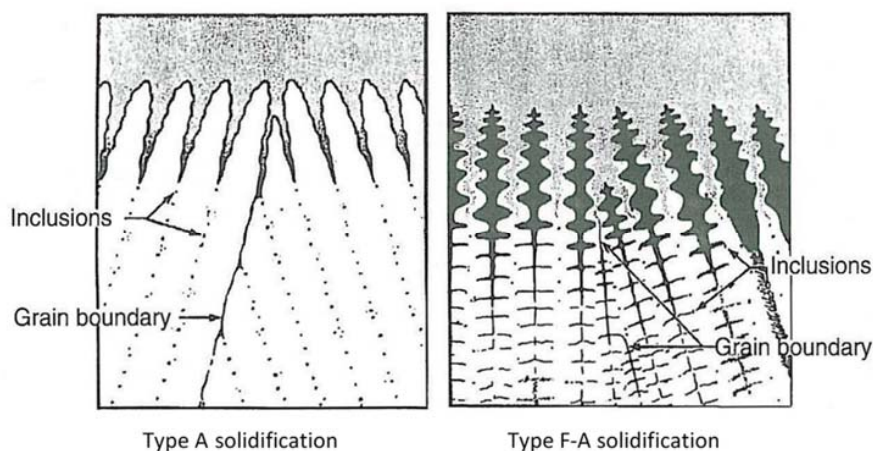


Figure 2.8: Difference in grain boundary morphology between A type and F-A type solidification. (Brooks et al., 1984)

2.2.3 Use of weldability diagrams in prediction of solidification cracking susceptibility

Different weldability diagrams which predict resulting room temperature microstructure and/or reigning solidification type have been developed in order to evaluate solidification cracking susceptibility of stainless steels. Common for all those diagrams are that they use certain equations to calculate chromium (Cr_{eq}) and nickel (Ni_{eq}) equivalents which are based on the known composition of material. Weldability diagrams are developed by using the data from very extensive experiments. One of the very first weldability diagrams was developed by Anton Schaeffler in 1949 and it is known as Schaeffler-diagram. Since then, several enhancement and upgrade proposal has been made to affiliating with the original Schaeffler-diagram: E.g. Delong 1956, Hull 1973, Hammar & Svensson 1979 and Kotecki & Sievert 1992 (known as WRC-1992 diagram), among others. Above mentioned diagrams with their chromium and nickel equivalents can be shown in Table

2-2. (Schaeffler, 1949) (DeLong, 1956) (Hull, 1973) (Hammar & Svensson, 1979) (Kotecki & Sievert, 1992)

Table 2-2: Chromium and nickel equivalents of different welding diagrams.

Author / name of diagram	Chromium equivalent (Cr_{eq})	Nickel equivalent (Ni_{eq})
Schaeffler (1949)	$Cr_{eq} = Cr + Mo + 1.5Si + 0.5Nb$	$Ni_{eq} = Ni + 0.5Mn + 30C$
DeLong (1956)	$Cr_{eq} = Cr + Mo + 1.5Si + 0.5Nb$	$Ni_{eq} = Ni + 0.5Mn + 30C + 30N$
Hull (1973)	$Cr_{eq} = Cr + 1.21Mo + 0.48Si + 0.14Nb + 2.20Ti + 0.72W + 0.21Ta + 2.27V + 2.48Al$	$Ni_{eq} = Ni + [0.11Mn - (0.0086Mn^2)] + 24.5C + 18.4N + 0.44Cu + 0.41Co$
Hammar & Svensson (1979)	$Cr_{eq} = Cr + 1.37Mo + 1.5Si + 2Nb + 3Ti$	$Ni_{eq} = Ni + 0.31Mn + 22C + 14.2N + Cu$
WRC-1992 (by Kotecki & Sievert, 1992)	$Cr_{eq} = Cr + Mo + 0.7Nb$	$Ni_{eq} = Ni + 35C + 20N + 0.25Cu$

In Figure 2.9(a) and 2.9(b), it can be seen Schaeffler diagram (on the left) and Hammar & Svensson diagram (on the right), in which several materials of known compositions is plotted according to their calculated chromium and nickel equivalents and known solidification mode (Suutala and Moisio, 1980) (Kujanpää et al., 1979). A certain trend can be found between the chromium / nickel equivalents and solidification modes. Depending on classification of solidification types, three or four different fields are perceivable: as in small chromium / nickel equivalent ratios like $Cr_{eq}/Ni_{eq} = 1.1$ (which means steep slope in trend line), solidification happens primarily austenitic mode, and as Cr_{eq}/Ni_{eq} -ratio increases (declined slope) near to $Cr_{eq}/Ni_{eq} = 1.5$, plot markings showed that solidification mode shifts ferritic-austenitic. Whereas the ratio is increased to value of 2.0 and more, solidification mode is regularized to exhibit ferritic solidification mode.

It has been confirmed by extensive investigations that compositions which solidifies in ferritic-austenitic (F-A) type, offer best resistance to solidification cracking, whereas primary austenitic solidification (A and A-F type) is tend to be most susceptible to solidification cracking (Kujanpää et al., 1979) (Cieslak et al., 1982) (Brooks et al., 1984). As an example of above, in Figure 2.10, result data from the experiments of Masumoto and Thier are incorporated to Shaeffler diagram. Both borderlines (solid and dashed) formed from the achieved result data, has same tendency as they point cracking and no cracking fields. (Masumoto et al., 1972) (Thier, 1976) (Kujanpää, 1979)

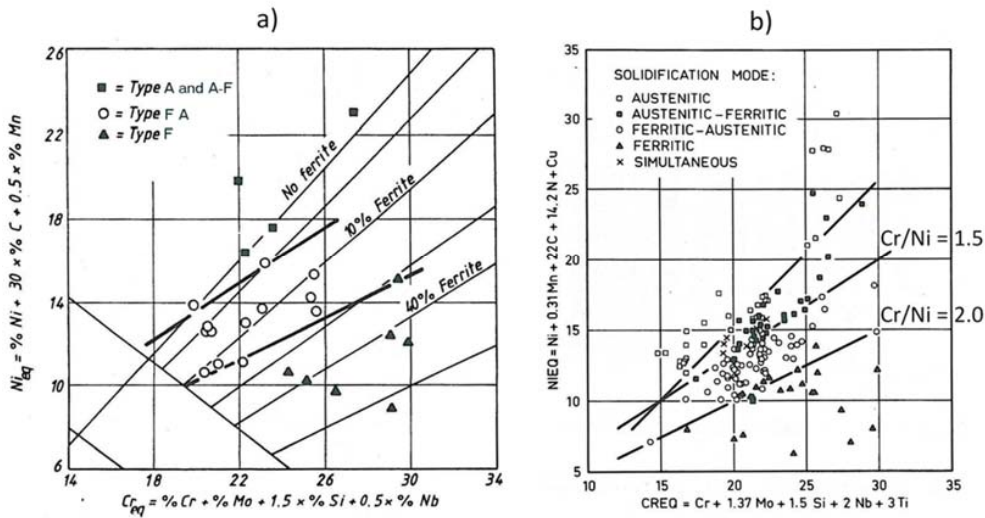


Figure 2.9: Solidification types plotted and located in (a) Schaeffler diagram (Kujanpää, 1979) and (b) Hammar & Svensson diagram. (Suutala and Moision, 1980)

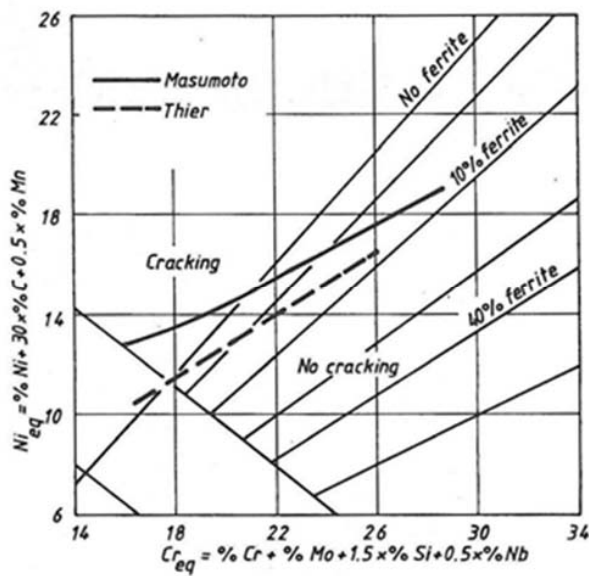


Figure 2.10: Solidification cracking and no cracking fields in Schaeffler diagram. Solid line: According to the work of Masumoto et al., 1972. Dash line: According to the work of Thier, 1976. (Kujanpää, 1979)

2.2.4 Modified welding diagrams which take impurity elements into account

It is commonly recognized that certain impurity elements like sulphur, phosphorous, silicon, boron, etc. enhance solidification cracking susceptibility in steels. Especially, sulphur (S) and phosphorous (P) are ranked to the most detrimental elements. Sulphur and phosphorous have low solubility in iron, (especially in γ -iron, see Table 2-3) chromium and nickel, which are the three major constituents of stainless steel (Borland and Younger, 1960) (Brooks and Thompson, 1991). The detrimental influence of these impurities is explained to relate to their potential to form low-melting eutectics (Table 2-3) which appear as liquid eutectic films along the grain boundary and interdendritic regions during the terminal phase of solidification. This is associated with the origin of cracking as weld solidification cracking is localized to occur as a rupture of above mentioned last solidifying liquid film. (Kujanpää, 1984) (Lippold and Kotecki, 2005) (Cross, 2005)

Table 2-3: Sulphur's and phosphorus's solubility in iron [%], possible low melting phases with melting temperatures. (Folkhard, 1988)

Constituent	Solubility in iron [%]			Low melting phase	Melting point [C°]
	γ austenite	δ ferrite	Temperature [C°]		
Sulphur (S)	0.05	0.14	1365	eutectic Fe-FeS eutectic Ni-NiS	988 630
Phosphorous (P)	0.20	1.6	1250	eutectic Fe-Fe ₃ P eutectic Ni-Ni ₃ P	1048 875

Kujanpää et al. (1979) represented modified welding diagram which coupled the use of Hammar & Svensson chromium and nickel equivalent diagram with the existing sulphur and phosphorous level. They gathered and evaluated wide range of published weld metal hot cracking data and plotted them to the diagram which is shown in Figure 2.11. Hammar & Svensson chromium and nickel equivalent diagram was chosen, because according to the studies of Suutala (1982a), it give the most suitable correlation between composition and solidification mode. (Kujanpää et al., 1979), (Suutala, 1982a) (Suutala, 1983)

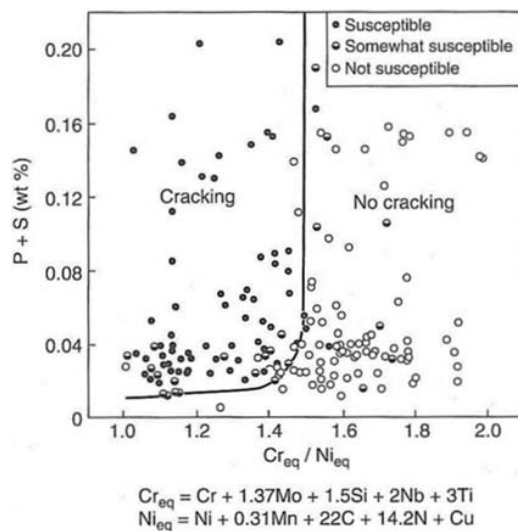


Figure 2.11: Suutala-Kujanpää diagram based on weld metal composition. Diagram is developed to predict solidification cracking according to known impurity content and chromium / nickel (Cr_{eq}/Ni_{eq}) equivalent ratio of produced weld metal. (Kujanpää et al., 1979)

The diagram shown in Figure 2.11 demonstrates how remarkable role the composition of weld metal plays on the effect of solidification cracking susceptibility. When the Cr_{eq}/Ni_{eq} -ratio increases to the critical level, to the value $Cr_{eq}/Ni_{eq} \approx 1.5$ and over the resistance against solidification cracking is increased drastically. This threshold is revealed to be based on the fact that solidification behavior is changed from primary austenitic to primary ferritic when the value of $Cr_{eq}/Ni_{eq} = 1.5$ is reached. As explained previously, primary ferritic solidification of weld metal possess far better resistance to solidification cracking than austenitic solidification. It can be also noticed from the diagram, that if Cr_{eq}/Ni_{eq} -ratio of weld metal is way below the value of 1.5 (that means without exception fully austenitic solidification), combined impurity level of phosphorous (P) and sulphur (S) must be very low, $P+S \approx 0.01\%$ (weight-%) or smaller in order to be resistant to cracking. Such extreme low impurity levels are difficult to achieve in practice and are often economically undesirable. That is why solidification cracking susceptibility is best prevented by balancing weld composition with selecting parent and filler material such a way that primary ferritic type of solidification is secured. (Kujanpää et al., 1979) (Suutala, 1982a) (Suutala, 1983) (Lippold and Kotecki, 2005)

2.2.5 Effect of high cooling rate and rapid solidification

When a weld pool is solidifying, conditions incorporate complex dynamic behaviors, like growth undercooling, growth of dendrites, including changes in dendrite tip composition and primary or secondary arm spacing as well as growth morphology. The terms growth rate R [mm/s] and thermal gradient G [$^{\circ}\text{C}/\text{mm}$] have great importance in solidification theory (Suutala, 1983). The growth rate R , also known as solidification rate correspond to the rate at which the liquid/solid interface advances in the weld pool. The thermal gradient G and growth rate R in the weld pool is a combined function of the material properties, position at the weld pool and heat input together with the used welding process. For example: Thermal gradient increases as the thermal conductivity of material decreases. In addition, in high energy density beam processes, like laser welding and electron beam welding the thermal gradient is larger than in conventional arc welding processes like gas tungsten arc (GTAW) or gas metal arc (GMAW) welding. The ratio G/R affects the growth morphology whereas the product of GR [$^{\circ}\text{C}/\text{s}$], also known as cooling rate, determines the spacing of the dendrite secondary arms. In practice, solidification conditions and evolution of weld microstructure is usually described using the term cooling rate GR . Cooling rates in welds can be greatly varied depending on the used welding processes, namely in laser and electron beam processes cooling rates may exceed the values on the order of $10^4 \dots 10^6$ $^{\circ}\text{C}/\text{s}$, whereas in conventional arc welding processes like gas tungsten arc (GTAW) or gas metal arc (GMAW) welding the cooling rates may vary from 10 to 10^3 $^{\circ}\text{C}/\text{s}$. (Suutala, 1983) (Katayama and Matsunawa, 1984) (Elmer, 1988) (David et al., 1987) (David and Vitek, 1989)

The influence of high cooling rates on the microstructure of stainless steel alloys have been studied by e.g. Katayama and Matsunawa (1984,1985), Lippold (1985), David et al. (1987), Elmer (1988), Vitek and David (1988), Brooks and Thompson (1991), Lippold (1995), Lienert (1998) and Lienert and Lippold (2003). The results from the studies of the above mentioned authors have shown the fact that high cooling rates and rapid solidification have altered the microstructures and solidification mode in stainless steel welds. Namely, the stainless steel material with the identical element compositions showed different solidification modes between slow and rapid solidification conditions. If it is contemplated a preliminary microstructural map for austenitic stainless steel welds constructed by Lippold (Lippold, 1995) in Figure 2.12, it can be pointed out the function of solidification rate on solidification mode. For example, if we have a weld metal with chromium / nickel equivalent ($C_{\text{req}}/N_{\text{req}}$) value of 1.5 and welding process (e.g. gas tungsten arc welding = GTAW) which enables a solidification rate range smaller than 10 mm/s, the map from Figure 2.12 shows that solidification occurs with Ferritic-Austenitic (F-A) mode. On the other hand, if the same weld metal with the same $C_{\text{req}}/N_{\text{req}}$ value of 1.5 undergoes the solidification with the growth rate of 20 mm/s or greater (which is typical for e.g. laser or EB welding process), the prevailing solidification mode will be fully austenitic (A) instead of ferritic-austenitic (F-A) described above.

The conventional welding diagrams e.g. introduced in Figures 2.9 - 2.11 are sufficient for evaluating microstructural characteristics and solidification cracking susceptibility in

conventional arc welding processes, in which solidification and cooling rates are slow or in moderate levels. Despite the fact, they are insufficient to use as such to predict welding products of rapidly cooling welding process like laser, laser-pulsed and EB welding. That is why the existing diagrams are further developed in order to widen the scope for welding process featuring rapid cooling.

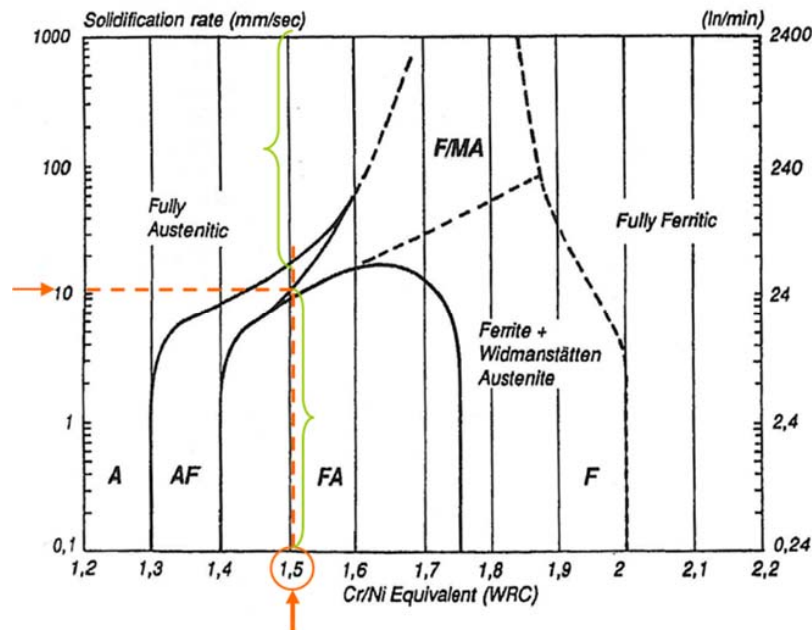


Figure 2.12: Example of microstructural map for austenitic stainless steel welds taking account of the weld composition (Cr_{eq}/Ni_{eq} -value) and solidification growth rate and solidification mode. Key: A=Austenitic, AF=Austenitic-Ferritic, F/MA=transformation of ferrite to austenite through massive transformation, F=Ferritic (Lippold, 1995).

Japanese and U.S. research teams have separately investigated the effect of high cooling rate ($10^4 \dots 10^6$ °C/s) on behavior of laser welded microstructures of several AISI 300 series stainless steels. Research teams have concluded that the original Schaeffler diagram (see Figure 2.9a) needs modification in order to enable predicting the occurring microstructure of rapidly cooled weld metal. Their studies pointed out that in rapid cooling the ferrite content of low-ferrite welds is further reduced whereas the ferrite content of high-ferrite welds is increased. As a result the two-phase (Austenitic-Ferritic or Ferritic-Austenitic) solidification range is radically suppressed while solidification mode is rather shifted to single phase solidification mode (primary austenitic or primary ferritic mode). This suppression of two-phase (Austenitic-Ferritic or Ferritic-Austenitic) solidification field is shown in Figures 2.13 and 2.14. (Katayama and Matsunawa, 1984) (Katayama and Matsunawa, 1985) (David et al., 1987) (Elmer, 1988)

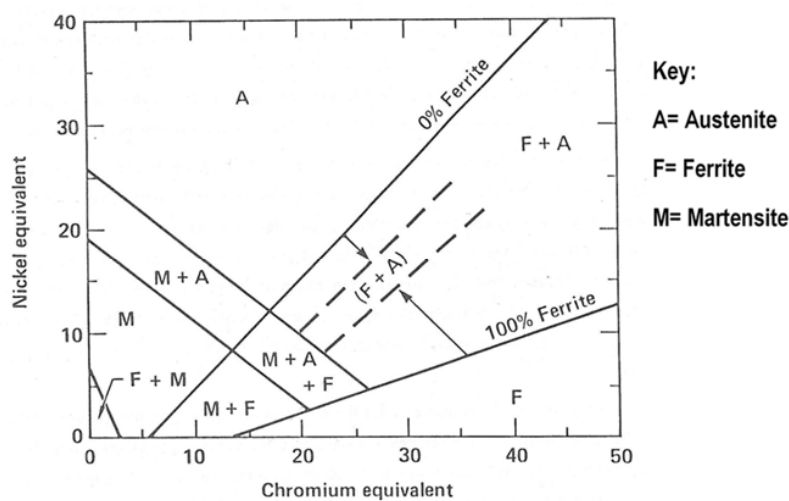


Figure 2.13: Example of modified Schaeffler diagram for rapidly cooling and solidifying welds showing how 0% and 100% ferrite boundaries are shifted towards each other suppressing the two phase (F+A) field dramatically. (Katayama and Matsunawa, 1984)

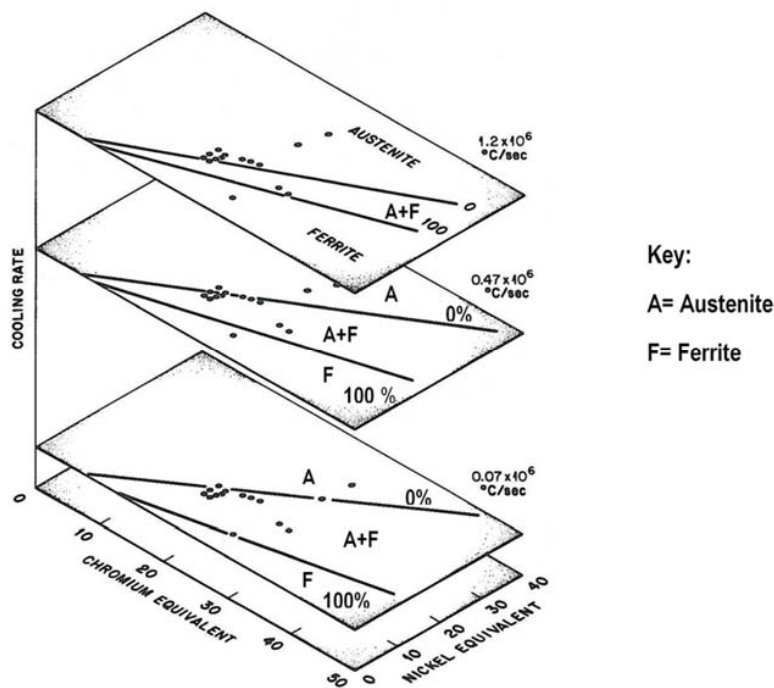


Figure 2.14: Example of modified Schaeffler diagram proposed by David et al. Cooling rate is illustrated as a third dimension. Austenite+Ferrite field is suppressed as weld cooling rate is increased. (David et al., 1989)

Above mentioned microstructural features in rapidly cooling and solidifying welds are evidently reported to be a consequence of shift in solidification mode during the cooling of weld metal. This shift in solidification mode has also implication for other welding diagrams like Suutala-Kujanpää diagram introduced before (Figure 2.11). In Figure 2.15, it is shown modified Suutala-Kujanpää diagram proposed by Pacary (1990). Pacary introduced new demarcation curvature according to the results achieved from the pulsed laser welding studies. It can be noticed that in pulsed laser welding (rapid solidification process) demarcation curvature which divide area cracking or no cracking, has transferred to the chromium / nickel equivalent ratio of $Cr_{eq}/Ni_{eq} \sim 1.68$ whereas in conventional arc welding demarcation lies near the Cr_{eq}/Ni_{eq} value of 1.5. In above case results support the findings that in chromium/nickel equivalent ratio range below ~ 1.68 rapid solidification favours austenite as the first solidifying phase, leading increased solidification cracking susceptibility. Despite the fact that Pacary's modified welding diagram is based on the test carried out by pulsed laser welding, it can be suggestively applied to other processes like continuous wave laser welding and electron beam welding which in known to produce rapid solidifying welds as well. (Suutala, 1983, Lippold and Kotecki, 2005)

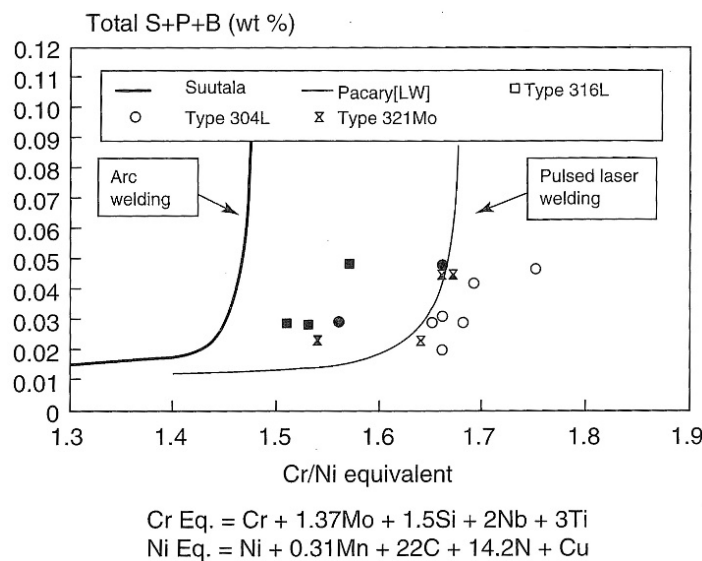


Figure 2.15: Example of modified Suutala-Kujanpää diagram proposed by Pacary for predicting hot cracking in rapid solidification conditions. Key: Solid symbols = cracking, open symbols = no cracking. (Pacary et al., 1990, Re-printed in Lippold and Kotecki, 2005)

2.2.6 Prevention of weld solidification cracking

For the occurrence of weld solidification cracking two prevailing conditions is needed: i) thermally and/or structurally imposed restraint and ii) cracking susceptible microstructure

(Lippold, 2015). When considering thermally imposed restraint and strains, high energy density beam welding of material with low thermal conductivity such as an austenitic stainless steel can produce elongated, teardrop-shaped weld pool. Especially with high welding speeds which are inherently characteristic to laser and electron beam welding processes, grains in solidified weld pool are able to grow from both sides of the fusion boundary towards the centreline without competitive growth. In very rapid cooling conditions, solidifying grain boundary can even be orientated parallel to the fusion boundary. If adjacent tension due to thermal contraction is simultaneously present, the weld centreline can be highly susceptible to weld solidification cracking. (Lippold, 2015)

Preventing or minimizing solidification cracking in welding of austenitic stainless steels is executed simply and most effectively by controlling the composition of base and filler materials. This means that weld metal composition should be balanced such a way that ferritic-austenitic (F-A) solidification mode is secured, because (F-A)-solidification provides far better resistance for solidification cracking than e.g. fully austenitic (A) solidification. Weldability diagrams described earlier can be used to help choosing proper weld composition. It has to remember the proper use of those diagrams: In high energy density welding processes (e.g. laser welding and electron beam welding) the effect of rapid solidification on the solidification mode and resulting microstructures must be taking into consideration. Depending on the service conditions and applications, ferritic-austenitic (F-A) solidification of the welds can not be always produced. As an example could be a case where antimagnetic or cryogenic properties prevails or endurance in harsh corrosion environment exclude the possibility to contain any room temperature ferrite in produced weld. In that case one possibility is to minimize the weld restraint by means of structure, joint and groove designing. However, in assembly welding of very rigid and massive structures, high stresses and restraints can not be usually avoided. Consequently, if weld solidifies in fully austenitic and at the same time it is affected by high level of strains, a danger of weld solidification cracking will be pronounced. In above case the only factor which is left in prevention of weld solidification cracking is to use high-purity base and filler materials which contain very low content of detrimental impurity elements like sulphur and phosphorous. (Lippold and Kotecki, 2005)

2.3 Thick section laser welding

Solid state high brightness lasers of new generation are providing ever increasing power levels for welding. Established high-power levels of disk and fiber lasers for thick section welding applications have been typically around 10-20 kW. Currently, a fiber laser equipment with 100 kW laser power has been commercially available and one such unit has been installed in Japanese research institute. (Rethmeier et al., 2009) (Grupp et al., 2013) (Zhang et al., 2014) (Rominger et al., 2015) (Katayama et al., 2015)

2.3.1 Single-pass welding

In laser beam welding, the available power density (W/cm^2) is much higher than that of conventional arc welding processes (Katayama, 2013). That is why laser welding is considered as a high energy density welding process, in which an ability to use a keyhole welding is exploited. In order to bring e.g. a steel alloy locally in the vapour phase for keyhole welding, the power density of laser beam at the surface of the work piece must be risen to the magnitude of $10^6 \text{ W}/\text{cm}^2$ or greater. (Ion, 2005) (Elmer et al., 2009)

At the power density of $10^6 \text{ W}/\text{cm}^2$ weld cross-sections with high depth (d) to width (w) ratio (d/w) can be produced. The d/w-ratio can yield to 10:1 or even greater (Elmer et al., 2009). Such an example of the butt-joint weld cross-section produced into 12 mm thick type 304 austenitic stainless steel with 10 kW autogenous fiber laser welding can be seen in Figure 2.16 (Zhang et al., 2014).

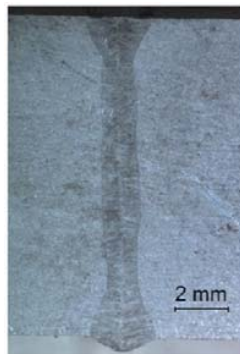


Figure 2.16: Example of high depth to width ratio ($d/w \sim 9:1$) single-pass weld cross-section characteristic for high-power thick section laser welding. Material: type 304 austenitic stainless steel with plate thickness of 12 mm; Laser power 10 kW; Focal spot diameter $\phi 0.4 \text{ mm}$; welding speed 2.4 m/min. (Zhang et al., 2014)

The power density is the quotient of the beam power and cross-sectional area of the beam. Therefore the power density to be used is primarily controlled by the focal spot diameter and the available laser power. In Figure 2.17 it is plotted the mentioned relationship, showing the required laser power to reach a given power density as a function of beam diameter. For example, to achieve a power density of $10^6 \text{ W}/\text{cm}^2$, required for a keyhole mode welding, a 0.5 mm diameter beam only requires approximately 2 kW of laser power, whereas a 1 mm diameter beam requires approximately 8 kW of laser power. (Elmer et al., 2009) Taking advantage of mentioned relationship offers particularly in the case of solid state lasers operating at the 1 micrometre wavelength a chance to scale power density and in that way have a chance to control the shape of produced weld cross-section if necessary. Available laser spot diameter can for example be manipulated by defocusing the beam, using longer focal length optics and/or stepping up to larger diameter process fiber. (Elmer et al., 2009) (Kawahito et al., 2009)

The focused laser spot diameter (d_f) available is dependent on the used optical set-up of a welding head and can be defined with the following equation (Ion, 2005):

$$d_f = d_{fibre} \frac{F_l}{F_r} \quad (2.1)$$

Where d_{fibre} is the core diameter of process fibre, and F_l and F_r are the focal lengths of the launch and recollimation lenses, respectively. The equation 2.1 is useful when assessing the suitable combination of processing fibre diameter and the optical configuration of welding head for a specific welding application. An example of such assessment using equation 2.1 is given in Table 2-4, in which a chosen F_r is kept constant 120 mm while combination of three different process fibre diameter options (A1, A2, A3) and two focal length options (B1, B2) are compared to examine the resulting focused laser spot diameter (d_f) available.

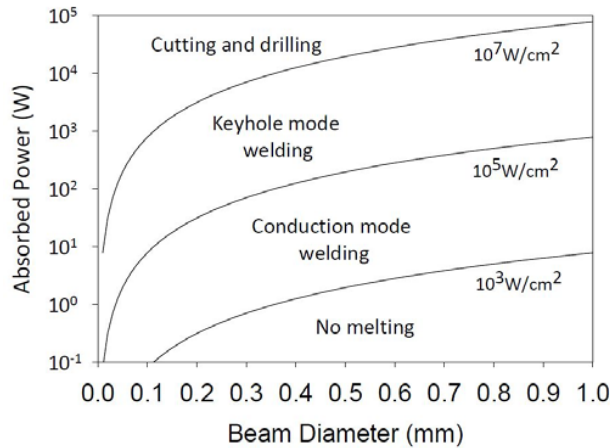


Figure 2.17: Constant power-density boundaries showing the relationship between the applied laser beam diameter and laser power for approximate regions of different laser materials processing applications. (Elmer et al., 2009)

Table 2-4: Example showing the effect of different processing fibre diameter and focal length combination options on available focused laser spot diameter. Calculations were made according to Equation 2.1 and recollimation length is chosen as a constant $F_r = 120$ mm.

Processing fibre diameter [μm]	Focal length B1; 300 mm	Focal length B2; 450 mm
	Focused laser spot diameter [μm]	
A1; 200	500	750
A2; 300	750	1125
A3; 400	1000	1500

Autogenous high-power laser welding can allow efficient joining of thick-sections, but it requires stringent fit-up tolerances from the joints to be welded because of the small diameter of the laser beam. In butt-joints the best practice is to use closed gap preparation. In Figure 2.18 it is presented as an example of a single pass butt-joint weld produced on 20 mm thick AISI 316L austenitic stainless steel plates using a fibre laser with 19 kW laser power and welding speed of 1.5 m/min (Kujanpää, 2014). This demonstrates the modern high-power fibre laser welding equipment's capability to produce ~1 mm weld penetration in austenitic stainless steel per 1 kW of used laser power at a welding speed of 1.5 m/min.



Figure 2.18: Example of a single-pass fibre laser weld produced on 20 mm thick butt-joint of AISI 316L austenitic stainless steel plates. Laser power 19 kW; welding speed 1.5 m/min; Focal position $F = -4$ (Kujanpää, 2014).

When considering welding of thick section joints an autogenous laser beam welding is not always practically feasible and that is why filler metal addition to the welding process is needed. The need for the use of filler addition can be associated with accommodation of the joint fit-up tolerance requirements of the welded parts (Wester et al., 2008) (Rethmeier et al., 2009) or for example, metallurgical and mechanical properties required for the produced weldments (Westin et al., 2011) (Gook et al. 2014) (Gook et al. 2015).

Filler metal can be introduced to the laser process for example, via an arc (laser-arc hybrid) as a molten form or using a cold-wire (Dilthey, et al., 1999) (Dilthey and Wiesschemann, 2002) (Jokinen et al., 2003) (Salminen and Kujanpää, 2003) or pre-heated wire feeding (Ohnishi et al. 2013) (Peng et al., 2016). Also pre-set filler metal foil inserts inside the joint has been used (Kujanpää et al., 1990) (Westin et al., 2011). In addition to the option of using pre-set filler metal foil, Wahba et al. (2016) demonstrated in their investigations that with using fine cut-wire particles of solid filler wire that were pre-set into the groove as an additional filler metal prior welding, a 25 mm thick open square butt-joint could be successfully laser-arc hybrid welded with a single pass. The above-mentioned technique utilizes a relatively wide 2.5 mm root gap and a necessary

backing solution that is realised using a temporary copper backing with an appropriate fusible submerged arc welding flux layer on top of it.

Filler metal addition in a welding wire form with laser welding with wire feeding or via laser-arc hybrid process is currently considered to be the most practical method. In addition, a solid welding wire has the advantage that contaminant pickup is low and there is available wide variety of gas metal arc wires with different chemistry and wire diameters (Ion, 2005).

In laser-arc hybrid and laser cold-wire welding, the filler wire feeding parameters such as wire feeding rate and feeding position, are dependent on the width of the air gap and thickness of the joint to be welded. The wire feeding rate must be adjusted according to welding speed and gap volume. In addition, the wire can be fed either into leading edge or trailing edge of the laser beam / weld pool interaction zone in respect to welding direction. Process fundamentals and parameters involved in laser keyhole cold-wire welding and laser-gas metal arc hybrid processes were thoroughly investigated for example by Arata (1986), Salminen and Kujanpää (1995), Salminen and Kujanpää (2003), Dilthey et al. (1999), Dilthey and Wiesschemann (2003), Jokinen et al. (2003) and encompassing process parameters descriptions can be found from above references.

From industrial point of view one interesting application area which can be mentioned for the use of thick section laser-arc hybrid welding is installation of large diameter pipelines. For example, in order to improve the productivity of pipeline girth welding, Rethmeier et al. (2009) investigated optimum parameter combinations for laser-arc hybrid and laser cold-wire welding with 20 kW fiber laser and developed welding procedures for up to 32 mm thick pipe steel joints with different welding positions. In the experiments, they e.g. demonstrated positional welding of 16 mm thick butt-joints in flat (PA), vertical up (PF) and vertical down (PG) position with single pass using laser-arc hybrid and laser cold-wire processes. Moreover, they concluded that in 16 mm thick butt-joints they tested, up to 2 mm edge misalignment and root gap up to 0.3 mm could be successfully tolerated and bridged, respectively. In Figure 2.19 it can be seen the examples of 16 mm thick butt-joint weld cross-sections from the positional welding experiments of Rethmeier et al. (2009).

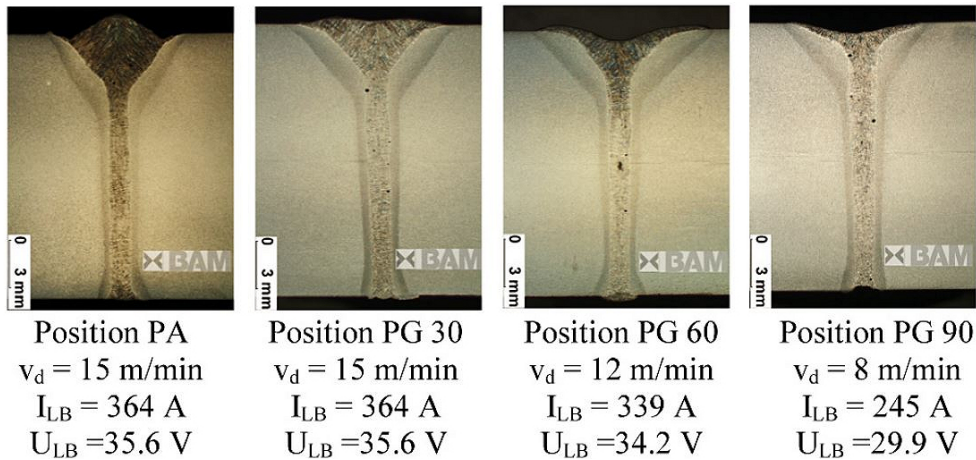


Figure 2.19: Weld cross-section examples of 16 mm thick butt-joint welds from positional laser-arc hybrid welding experiments from Rethmeier et al. (2009). Laser power 17 kW; welding speed 2 m/min.

In further experiments carried out by Gook et al. (2018), which were extended from that of Rethmeier et al. (2009), the investigators managed to enlarge root gap bridging tolerance from 0.3 mm to 0.7 mm using laser beam scanning optics in laser-arc hybrid welding of 16 mm thick butt-joints of X65 pipe steel, Figure 2.20.

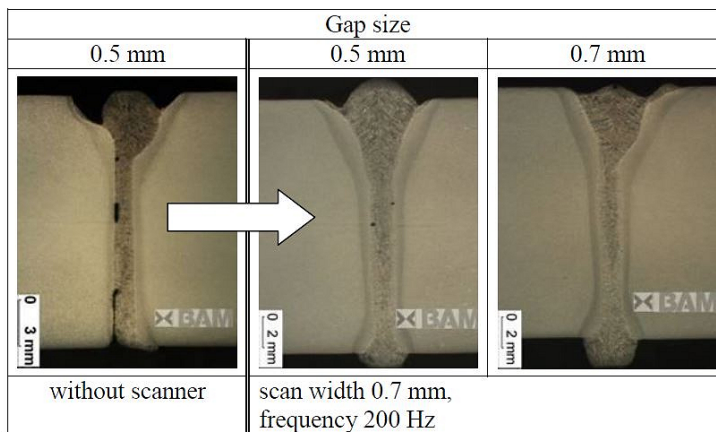


Figure 2.20: Cross-sections of laser-arc hybrid welds produced in 16 mm thick butt-joints with root gaps of 0.5 mm and 0.7 mm. In joints pictured on the middle and right hand side a scanner optics module is applied at a frequency of 200 Hz and an amplitude of 0.7 mm. Laser power 19 kW; welding speed 2.2 m/min. Gook et al. (2018)

2.3.2 Multi-pass welding

Automated or mechanized multi-pass narrow gap (NG) welding with filler wire addition has been traditionally utilized with conventional arc welding methods like gas tungsten arc welding (NG-GTAW), gas metal arc welding (NG-GMAW) and submerged arc welding (NG-SAW) in joining thick-section materials especially in components fabrication for power plants. (Zhang et al., 2011) (Xiao et al., 2015) (Liu et al., 2018)

NG-GTAW and NG-GMAW have the advantage over NG-SAW that they can be used for all-position welding, but they suffer from rather low welding speed (NG-GTAW < 0.15 m/min and NG-GMAW < 0.3 m/min) and high amount of deposited filling passes and increased deposited welding energy accumulation. That is causing limited production efficiency and in addition, resulting in increased heat input per weld unit length and welding distortions. In order to overcome those limitations, laser beam welding combined with arc-hybrid process or filler wire feeding (Jones et al., 2003) are foreseen as alternative welding technologies.

Katayama et al. (2015) demonstrated in their fundamental research on 100 kW fibre laser welding that a 70 mm thick closed square preparation can be autogenously laser welded with two passes, applying one pass from both sides at 100 kW and welding speed of 2 m/min. In corresponding thick section applications with much lower laser power levels, but nevertheless in multi-kilowatt range, an applicable way is to use a combination of narrow gap groove and multi-pass welding with filler wire procedure. Multi-pass laser welding can be performed e.g. with an arc-hybrid process or a filler wire feeding without the arc and from one or both side of the plates that are being joined. A groove design are usually aimed to be such that the total cross-sectional area of the groove can be kept as minimal as possible in order to minimize the amount of required deposited filler metal and number of filling passes. Typical joint preparation is a single or double V-preparation with a root face. Very small groove angles, between 4 to 10 degrees are typically used, Figure 2.21(a). (Zhang, 2013) The height of a root face is normally chosen according to the achievable fusion depth that the laser power available is capable of producing in a root pass welding. Concerning subsequent filling passes, the most convenient practice is to use one pass per layer build-up sequence, Figure 2.21(b) (Zhang, 2013).

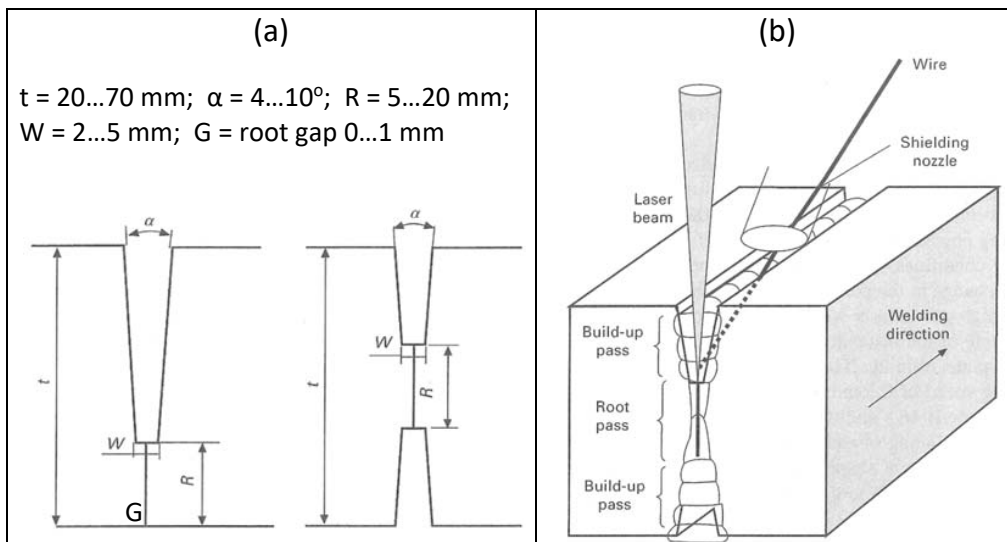


Figure 2.21: (a) Examples of groove configurations used in multi-pass laser welding; (b) Schematic presentation of multi-pass laser welding with filler wire from both sides. (Zhang, 2013)

Although a very narrow groove geometry is desirable in multi-pass welding, there are some welding process related principles that are needed to be taken into account: The diameter of the laser beam changes when it exits from welding head and advances along the vertical direction of its conical path towards work piece to be welded. This beam diameter change is depending on the optical set-up and the beam focusing settings used. That is why a groove angle or gap opening at surface of the joint needs to be wide enough to accommodate the laser beam passage into the bottom of the groove. During the multi-pass welding, some level of inevitable welding deformation will take place. In particularly, transversal shrinkage and angular distortion will constrict the width of groove tighter. If necessary, above effect needs to be also counted in the groove design. Moreover, especially if laser-arc hybrid process is applied to over 30 mm deep grooves, the gap between the fusion faces needs to be adequately wide to accommodate an arc torch / a contact nozzle tip into appropriate position respect to the bottom of the groove. This ascertains the prerequisites for fluent arc generation along with robust process transfer during the laser-arc hybrid welding. For above reason a laser cold-wire welding i.e. without an arc, allows a bit easier approach into a bottom of deep and narrow groove because in cold-wire welding a much longer stick-out length (wire extension between the tip of wire nozzle and work piece) for filler wire can be used.

In Figure 2.22 it is shown as an example of applied narrow gap groove geometry and multi-pass weldment in 50 mm thick type 316L austenitic stainless steel produced by Zhang et al. (2011) with a disk laser welding with filler wire. The welding was carried out on both sides using a 6 kW laser power and 0.4 m/min welding speed: One root pass

was made without filler metal for each side and followed by build-up welding with filler wire requiring 3 filling passes for each side.

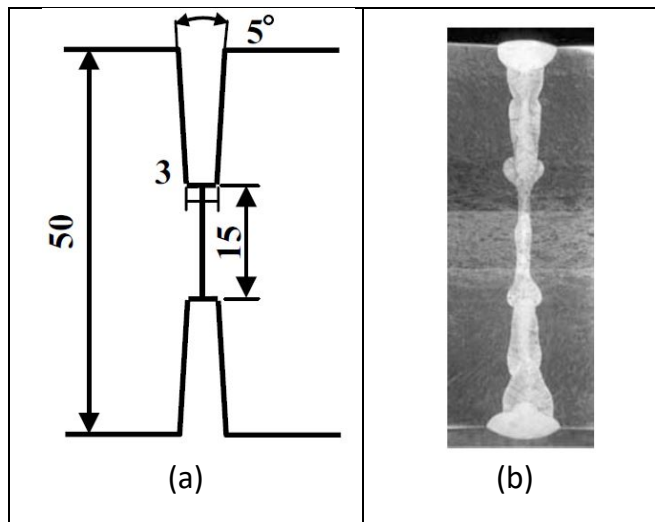


Figure 2.22: Example of double sided narrow gap groove geometry (a) used for welding of 50 thick type 316L austenitic stainless and a resultant multi-pass weld cross-section (b) produced with using a combination of laser welding and laser welding with filler wire. (Zhang et al., 2011)

Yang et al. (2019) investigated narrow gap laser welding with filler wire of 100 mm thick joints of type 304 austenitic stainless steel plates. They used very narrow U-shaped groove with 4 mm width and 5 mm root face thickness. Because of narrow and deep groove, they utilize a long needle-like wire feeding guide nozzle to fit it inside the groove during welding, Figure 2.23(a). Laser power and welding speed used for filling passes were 4.5 kW and 0.6 m/min, respectively. The authors reported that they needed 1 root pass and 42 filling passes to complete 100 mm thick weld joint (Figure 2.23b) and the angular distortion of the joint stayed below one degree.

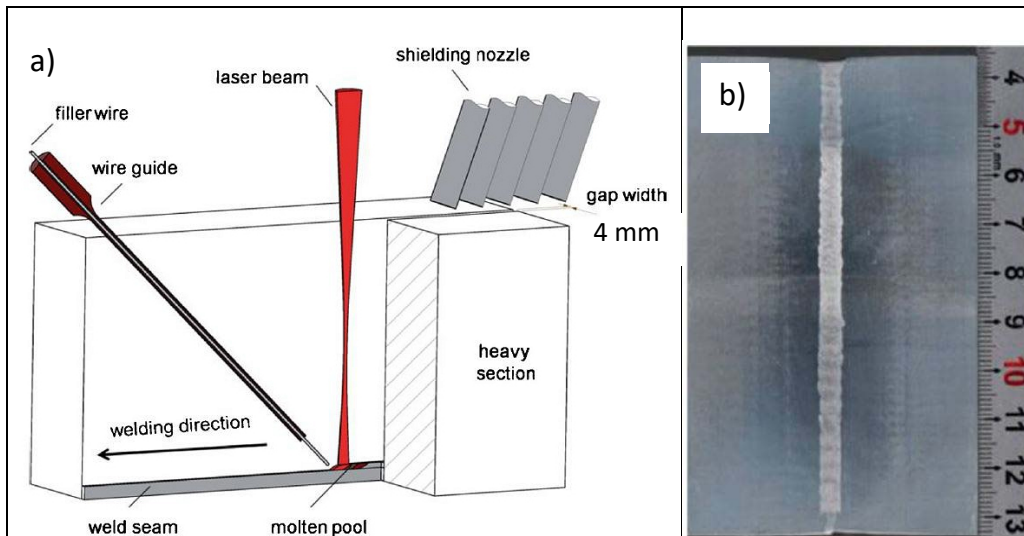


Figure 2.23: (a) Schematic presentation of multi-pass laser welding with filler wire using 4 mm narrow gap design for joining 100 mm thick type 304 austenitic stainless steel plates; (b) resultant multi-pass weld cross-section with a root pass and 42 filling passes. (Yang et al., 2019)

Zhang et al. (2018) performed experiments on 40 mm thick type 316 L austenitic stainless steel using multi-pass laser-arc hybrid welding with V-groove with 10 degree bevel angle and 5 mm thick root face. The schematic presentation of groove configuration and the set-up of laser beam and arc torch arrangements used in the experiments can be seen in Figure 2.24(a). Optimized laser-arc hybrid welding parameters for multi-pass procedure with a root pass and 13 subsequent filling passes (Figure 2.24b) were: The root pass was made with 4 kW laser power and 1 m/min welding speed while the used arc current and voltage was 200 A and 22 V, respectively. For filling passes 2.5 kW laser power, 1 m/min welding speed and arc current and voltage range of 200-250 A and 22-22.4 V were used, respectively. Furthermore, it was reported in above study that if welding parameters were not optimized, due to narrow groove and small distance from the tip of the wire to groove side walls, the arc was easily attracted by side walls, which caused arc deflection and unstable arc burning, Figure 2.25.

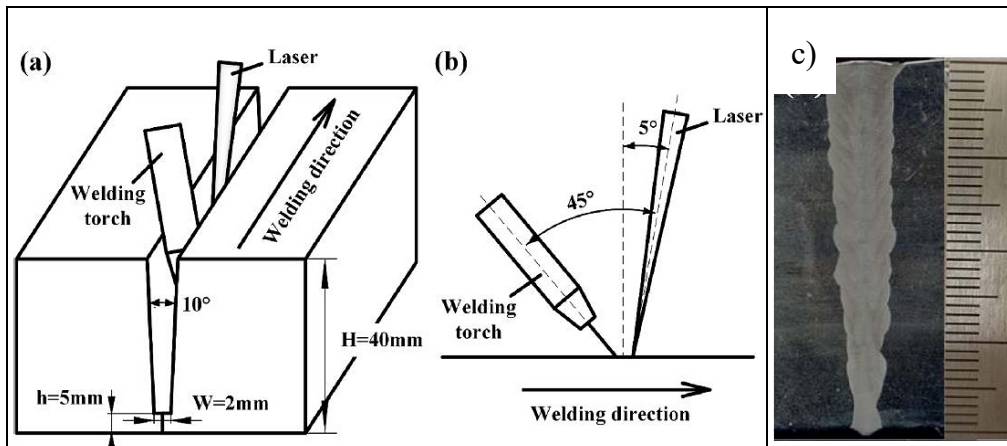


Figure 2.24: (a) Schematic presentation of groove configuration and the set-up of laser beam and arc torch arrangements used in the multi-pass laser-arc hybrid welding of 40 mm thick type 316 L austenitic stainless steel plates; (b) resultant multi-pass weld cross-section with a root pass and 13 filling passes. (Zhang et al., 2018)

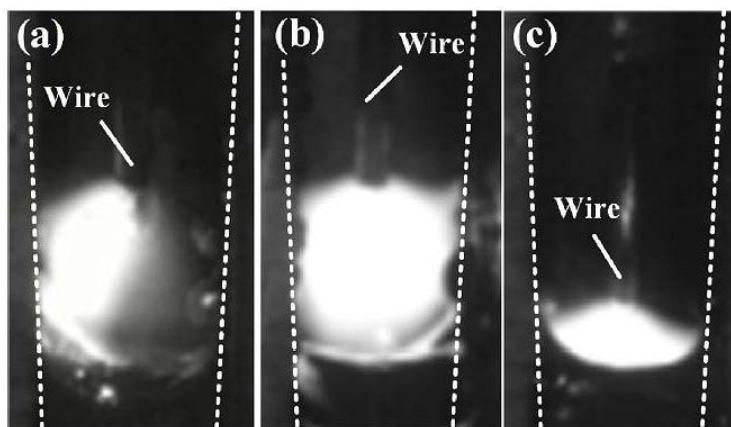


Figure 2.25: High speed photography from narrow gap laser-arc hybrid welding: (a) deflection of the arc, (b) arc burning instability, (c) stable welding process. (Zhang et al., 2018)

2.4 Mixing in thick section laser welding

By mixing in this occasion, it is meant of mixing between a filler metal and base metal in a macroscopic scale when they are added together into a weld metal by welding. Common attribute associated with describing mixing in weld metal is homogeneity. By this it is meant how evenly filler metal and base metal are mixed together across the whole fusion zone. In normal practice it is aimed to homogenous mixing in weld metal as this provides

basis for uniform microstructure and consistent resultant chemical and mechanical properties across the produced weld metal.

As it was discussed in earlier sub-sections, there can be several practical reasons why a use of filler metal addition is required in thick section laser welding. Usually, the need for the use of filler metal arises from joint fit-up tolerances. In those applications quite often used suitable practice is to choose a filler metal chemistry which closely matches to the welded base material. In above cases mixing is not a concern if there are no discernible elemental contrast between the base and filler metal chemistry. But concerns can be arisen in certain thick-section application where besides of enhancing gap bridgeability, a weld metal chemistry needs to be alloyed with a filler metal containing an over-alloying composition compared with that of a welded base metal. For example, Westin et al. (2011) studied laser-arc hybrid single-pass welding of 13.5 mm thick type 2205 duplex stainless steel using a leading torch configuration. They found that the duplex ferrite-austenite microstructure in produced welds are not in balance while at the mid-thickness and root portion of the weld cross-section showed too high ferrite proportions respect to austenite counterpart. In conducted corrosion tests they pointed out that excessive ferrite content at root side had decreased the weld metal pitting resistance. They concluded that the improved austenite formation from the use of filler wire was limited to the upper half of the weld cross-section. Gook et al. (2013), reported also from the challenges of getting a filler wire elements mixed into the deep bottom of the closed butt-joint in laser-arc hybrid welding of thick root pass of pipe steels grade X80 and X120. They studied the possibility to enhance weld toughness properties with applying nickel alloying into weld metal with a help of filler metal. They used a leading torch configuration and concluded that beyond a 14 mm thick square root face preparation, no filler metal addition could be detected from the weld metal. In laser cold-wire and laser-arc hybrid welding experiments of 11.5 mm thick cryogenic 9%Ni-steel for LNG (large-size liquefied natural gas) storage tanks, Gook et al., (2015) used a nickel base type 625 filler wire for closed butt-joints. Both cold-wire and hybrid process experiments were made using leading wire feeding. In weld cross-sectional analysis they observed inhomogeneous filler metal mixing in the welds from both welding processes. In the laser cold-wire weld the distribution of nickel base filler metal was weaker and more inhomogeneous compared to the laser-arc hybrid weld. The elemental mapping studies showed that only a minor part of filler metal exists at mid-thickness of the cold-wire weld while at the root portion no filler material could be detected, Figure 2.26(a). In the hybrid weld, however, the filler metal distribution was homogeneous from the upper part of the weld cross-section till the depth of about 6 mm and below that level filler metal mixing is getting weaker and inhomogeneous, Figure 2.26(b).

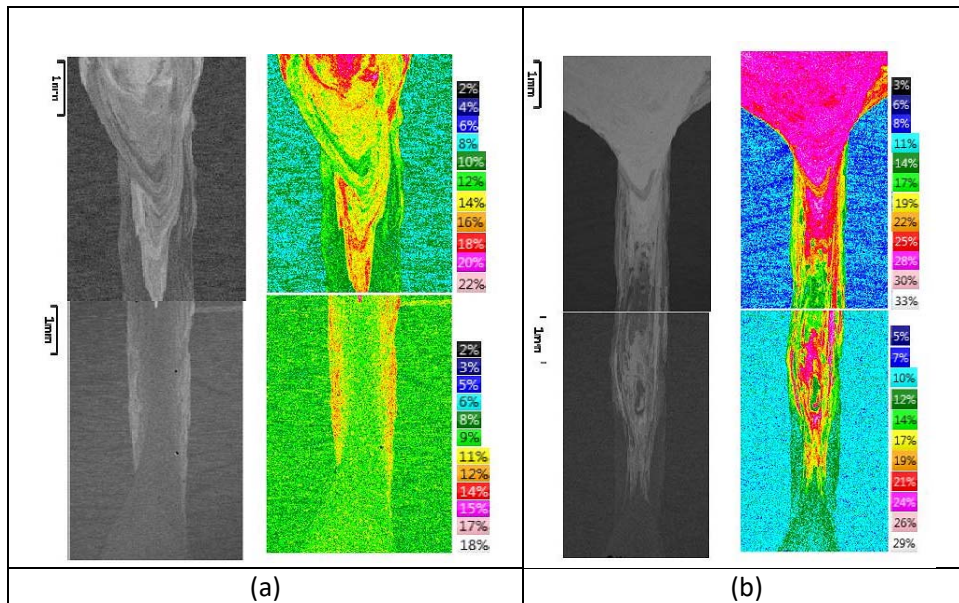


Figure 2.26: Ni concentration EDS mapping from the laser cold-wire weld cross-section (a) and from the laser-arc hybrid weld cross-section (b). Monochrome profile shown on the left and colour element map on the right. (Gook et al., 2015)

In all experimental examples presented above, a closed butt-joint geometry was used, filler wire feeding was introduced in leading configuration respect to the laser beam and welding direction. In addition, the horizontal wire tip distance to laser beam in hybrid welding was between 3-5mm, whereas in the cold-wire example it was zero. Furthermore, a recap from the main process parameter values used in the welding experiment references presented on the basis of mixing discussion in this sub-section can be found later in Table 2-5 located at the end of the section.

Victor et al. (2008) studied laser-arc hybrid welding of 9.5 mm thick carbon steel with a 10-kW fibre laser. They evaluated the effect of process orientation on filler metal mixing in closed butt-joint. Austenitic stainless steel type 308 filler wire was chosen to reveal contrast between the low alloyed carbon steel base metal and the over-alloyed filler metal from the etched weld cross-sections. The welding experiments were performed in both the leading and trailing arc torch configuration and with two horizontal wire tip distance to laser beam (D_{LA}) of 2 mm and 5 mm. The weld cross-sections presented in Figure 2.27(a-d), show filler metal rich portions etched on brighter grey colour while darker grey colouration represents more of weld portions with the base metal level. The mixing in the welds made with leading arc torch configuration appears to be quite similar for both D_{LA} settings, Figure 2.27 (a) and (b). The welds made with trailing arc torch configuration and the D_{LA} of 2 mm (Figure 2.27c) produced better mixing than both leading arc torch configuration cases. When considering combination of longer $D_{LA}= 5$ mm and trailing torch, Figure 2.27(d) indicates that filler metal remains mainly on the weld surface

resulting poor mixing towards the weld root. In mixing point of view above results suggest that with leading torch configuration setting D_{LA} is not so strictly defining than with trailing torch configuration where D_{LA} needs to remain much shorter than 5 mm. In overall hybrid process point of view, D_{LA} needs to be biased that both the laser and arc co-operates in mutual weld pool.

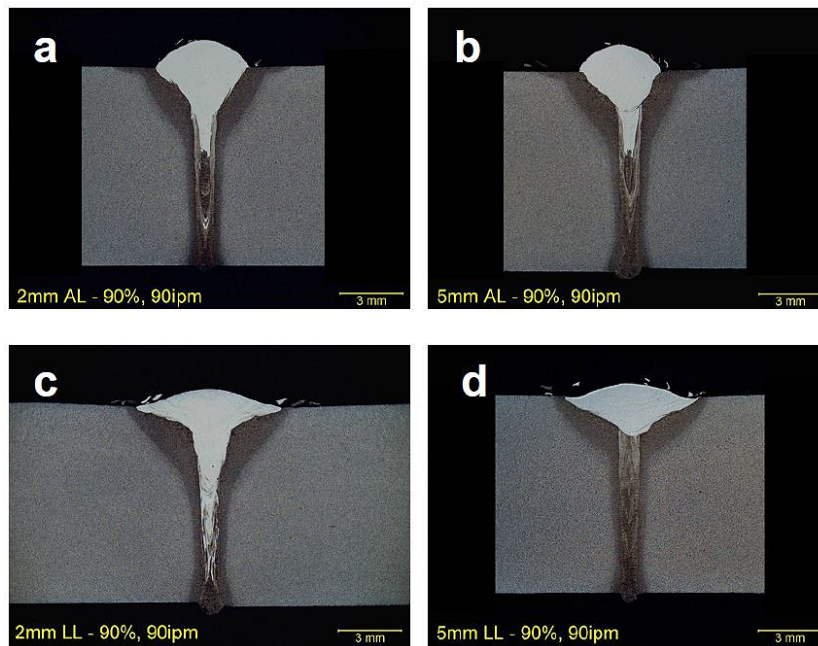


Figure 2.27: Filler metal mixing indications in single-pass closed square butt-joint laser-arc hybrid welds. (a) Leading arc torch and $D_{LA} = 2$ mm; (b) Leading arc torch and $D_{LA} = 5$ mm; (c) Trailing arc torch and $D_{LA} = 2$ mm; (d) Trailing arc torch and $D_{LA} = 5$ mm. (Victor et al., 2008)

In addition to mentioned mixing experiments, Victor et al. (2008) demonstrated in the same research study, that the experimental welding set-up they used, D_{LA} setting around 3 mm produced the deepest bead-on-plate weld penetration on both leading and trailing torch configuration, Figure 2.28.

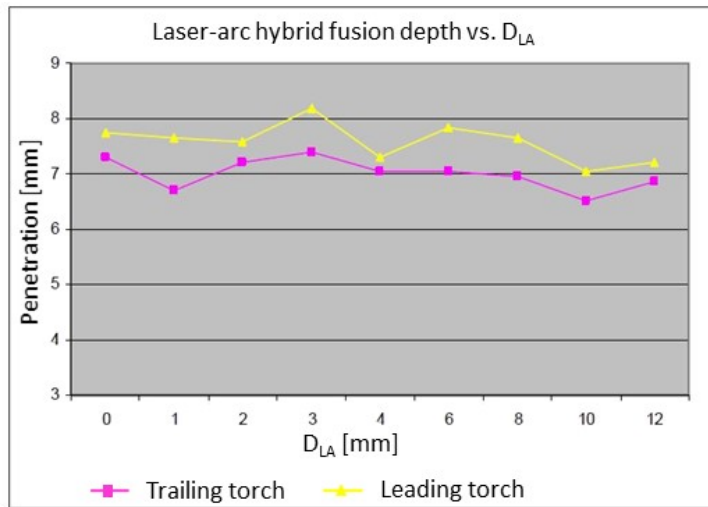


Figure 2.28: Bead-on-plate weld penetration plotted against different D_{LA} settings used in laser-arc hybrid welding with trailing torch and leading torch configuration. Laser power 5 kW, focal position 0 (surface), welding speed 2 m/min, wire feeding 8.9 m/min. (According to Victor et al., 2008)

Karhu et al. (2013) studied the effect of root gap (0-0.4mm) and wire feeding configurations (leading/trailing) on filler metal mixing of welds produced on 15 mm thick joints of AISI 316L austenitic stainless steel plates with laser-arc hybrid and laser cold-wire welding. In the experiments a constant D_{LA} setting of 3.5 mm and 0 was applied for laser-arc hybrid and laser cold-wire processes, respectively. Laser-arc hybrid welds were produced with leading wire feeding while in laser cold-wire welds also trailing wire feeding was tested. The authors concluded that compared to closed gap, the open gap preparations of 0.2-0.4 mm in laser-arc hybrid tests helped vertical filler mixing only a $\sim 1/3$ depth (~ 5 mm deep from the weld surface) of joint thickness. At near the weld root portions, in depths between 10-15 mm mixing was observed to be by average ~ 2 to 4-fold lesser compared to the mixing values at the near surface region. The results of laser cold-wire welds showed that in closed root gap the mixing was equally poor and inhomogeneous with both leading and trailing wire feeding. The authors pointed out by applying EDS transversal line scans across the weld fusion zones, that quite a large fluctuation in mixing profiles take place at the depth range of ~ 6 mm and deeper from the weld surface in both laser-arc hybrid and laser cold-wire welds. In addition, they reported from very narrow $\sim 100 \dots 200 \mu\text{m}$ band in weld metal area locating adjacent to the fusion line, where filler metal mixing is quite largely decreased while a large local drop in mixing profile is clearly detectable. This can partly be due to epitaxial grain growth from the base metal towards unmixed and partially mixed zone.

Recently, Üstündag et al. (2019) introduced an interesting method to improve filler metal mixing in thick section laser-arc hybrid welding. The authors used an apparatus consisting

of AC magnet providing a maximum output power of 6 kW and an oscillating frequency of 1.2 kHz at the close vicinity of weld root side. The system generates external oscillating magnetic fields during the welding. It is known that when welding current is supplied through an arc torch from the surface side, the magnetic fields the electric current induces generate together the electromagnetic force as known as the Lorentz force (Kou, 2003). The authors (Üstündağ et al., 2018) used the developed system to generate additional corresponding upward Lorentz force from the root side, Figure 2.29. They described that the principle method has been previously successfully used for thick section laser-arc hybrid welding in order to give an electromagnetic weld pool support which gives an opportunity to use reduced welding velocity. With using electromagnetic weld pool support melt pool sagging and gravity drop-out of the weld root can be prevented. The possibility of allowing to use lower welding speed gives means to control cooling rate and weld pool solidification rate. Slower weld pool solidification may also help to introduce filler metal elements deeper in thick and narrow joints.

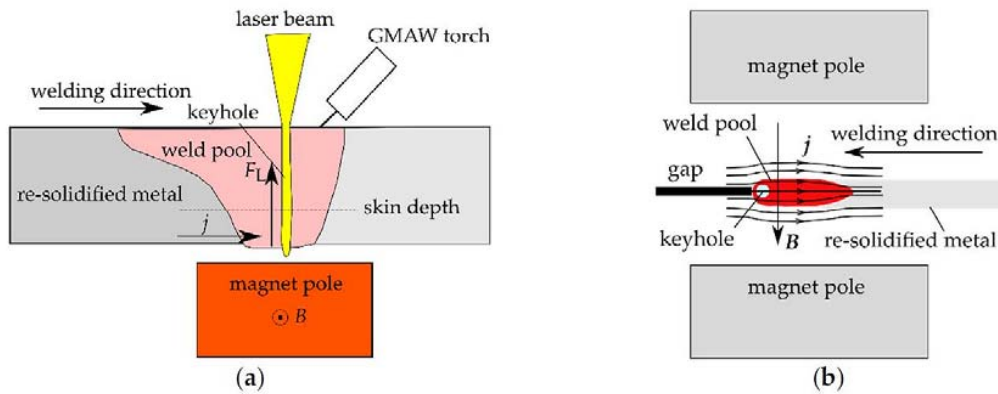


Figure 2.29: (a) Schematic of electromagnetic weld pool support system; (b) root side view. F_L = Lorentz force, B = magnetic flux vector, j = electric current vector. (Üstündağ et al., 2019)

In addition, the authors (Üstündağ et al., 2019) developed the above described system set-up further by finding the optimized turn angle setting for the used magnet poles in order to generate vortical flow of the melt which may have an additional stirring effect for the filler metal mixing. They demonstrated that the optimal balance for both electromagnetic weld pool support and electromagnetic stirring is found at a turn angle of 30° respect to transversal plane of weld pool cross-section and welding direction. With using the developed system the authors produced a 20 mm thick single pass laser-arc hybrid weld on S355 structural steel using a nickel base filler wire and reduced welding speed. Optimized magnet parameters included a turn angle of 30° , an AC power of 1.8 kW and an oscillating frequency of 1.2 kHz. The authors reported that in filler metal mixing point of view the EDS-results confirmed that the use of above set-up improved the homogeneity of the filler material distribution across the weld fusion zone from surface to root.

Table 2-5: Compilation of the main process parameter values used in laser-arc hybrid welding experiment references related to mixing discussion of sub-section 2.4. The values marked with superscript asterisk * denotes process parameter values of laser welding with cold-wire.

Laser power [kW]	Focal position [mm]	Wire feeding configuration	Welding speed / wire feed rate [m/min]	D _{LA} [mm]	Material / joint thickness [mm]	Reference
14	-4	leading	2.2 / 15	3	Duplex SS 2205 / 13.5	Westin et al. 2011
17	?	leading	2.6 / 16	?	X80 and X120 steel / 14	Gook et al. 2013
14	-3	leading	2* / 2* and 3 / 12	0* and 4-5	9%Ni steel / 11.5	Gook et al. 2015
9	0	leading / trailing	2,3 / 8.9	2 and 5	Carbon steel / 9.5	Victor et al. 2008
17	-4	leading / trailing*	1.5* / 1.8* and 15 / 2	0* and 3.5	Austenitic SS 316L / 15	Karhu et al. 2013
12.2	-11	leading	0.5 / 11	4	S355 steel / 20	Üstündag et al. 2019

2.5 Recognized needs for improvements

Derived from the theoretic background study, the following weldability aspects can be pointed out, which are further needed to be paid attention to and need further in-depth research and scientific knowledge for accelerating the progress of deploying laser welding in thick section applications:

- Knowledge from an assessment of solidification cracking in multi-pass laser welding
- Knowledge enabling enhancements in multi-pass laser welding and especially in laser-arc hybrid welding techniques in thick section applications exceeding thickness over 40 mm
- Knowledge concerning mixing behavior and influencing welding parameters on mixing in thick section laser welds

3 Research materials and methods

This chapter presents the materials used in the experiments of this dissertation and describes the research methods used.

3.1 Materials

The base materials used in the welding experiments were austenitic stainless steel alloys with the different plate thickness between 10mm and 60mm as follows:

- Alloy X, plate thickness 10 mm (Publication II)
- AISI 316L-A, plate thickness 10 mm and 20 mm (Publication II, III and IV)
- AISI 316L-B, plate thickness 60 mm. (Publication I and II)

The steels AISI 316L-A and B are both of ITER grade 316L(N)-IG heats.

The test specimens for the welding tests were rectangular pieces of 150 mm in width and 300-400 mm in length. Preparation of the required geometries and fusion faces of the test specimens was done by machining.

The filler materials used were stainless steel solid wires with following types and diameters:

- Thermanit 19/15, Ø1.2 mm (Publication I)
- ESAB OK Autrod 316LSi, Ø1.0 mm (Publication II)
- ESAB OK Autrod 308LSi, Ø0.8 mm (Publication II)
- Avesta 2205, Ø1.0 mm (Publication III and IV)

The exact chemical compositions of the base and filler materials are given in Table 3-1.

Table 3-1: Chemical compositions of base materials and filler materials. (Fe weight-% content = balance)

Element weight-%	C	Si	Mn	P	S	Cr	Ni	Mo	N	Cu	Ti+Ta
Base materials											
Alloy X	0.026	0.30	1.49	0.030	0.001	22.0	5.8	3.09	-	0.16	< 0.01
AISI 316L-A	0.024	0.37	1.70	0.020	0.0002	17.6	12.3	2.43	0.07	0.01	< 0.01
AISI 316L-B	0.025	0.36	1.70	0.021	0.0001	17.6	12.2	2.41	0.07	0.01	< 0.01
Filler materials											
Thermanit 19/15	0.015	0.46	7.32	0.013	0.005	20.2	15.1	2.79	0.18 7	0.09 5	-
Autrod 316LSi	0.020	0.80	1.80	0.018	0.011	18.4	12.2	2.50	0.06	0.09	-
Autrod 308LSi	0.020	0.90	1.00	0.020	0.010	19.7	10.7	0.04	-	0.03	-
Avesta 2205	0.010	0.36	1.60	0.017	0.0001	22.9	8.7	3.20	0.14 7	0.08	-

3.2 Methods

The research methodology of the dissertation utilises triangulation, in which research knowledge from different sources and from multiple perspectives are gathered and synthesised. This supports reliability viewpoints of the research. The triangulation of this study is based on the experimental research, theoretical background from scientific literature and numerical simulation studies, Figure 3.1.

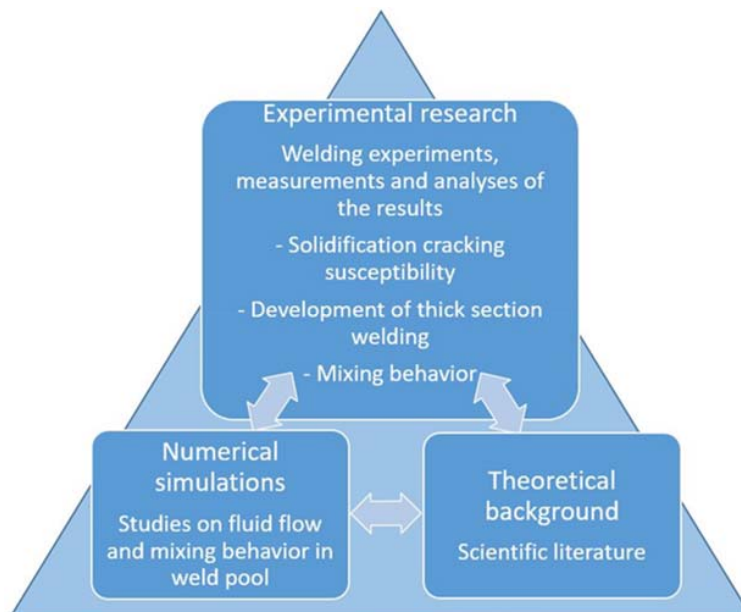


Figure 3.1: Research methodology used is gathering and synthesising research information from different sources and from multiple perspectives.

The laser types used in the experiments of this dissertation were solid state lasers that operate in continuous wave mode and at the 1 micrometre wavelength-range: A neodymium-doped yttrium aluminium garnet (Nd:YAG) laser and an ytterbium-doped fiber laser with a wavelength of 1064 nm and 1070 nm, respectively.

In Publications I and II, welding experiments were performed by using a combination of Nd:YAG-laser and GMAW hybrid and cold wire-processes. The Nd:YAG-laser used was a HAAS-LASER GmbH model HL 3006 D with \varnothing 0.6 mm optical fiber beam delivery system. The laser has a maximum output power of 3 kW at the surface of a work piece. Used lens focusing optic of welding head gives a 200 mm focal length, 6.12 degree focusing angle and can provide a spot diameter of 0.6 mm in the focal point.

Figure 3.2(a) shows the set-up used in the Publication II with multi-pass laser arc-hybrid welding experiments of 60 mm thick single side joint. In Figure 3.2(b) it is presented a principle drawing of the configuration used for the filling passes in laser-arc hybrid welding with defocusing technique.

In Publications III and IV, welding experiments were performed by using a combination of IPG 10 kW YLS-10000 fibre laser and GMAW hybrid and cold wire-processes. Beam delivery from the laser source to the welding station and welding head was with a process fiber of 200 μ m core diameter. The welding head was a laser welding head-unit from Kugler GmbH with copper metal optics and an adjustable GMAW torch unit. The optical

system of the Kugler laser welding head consisted of 120 mm collimation and 300 mm focusing lenses. The optical set-up can provide a focal spot diameter of 500 μm .

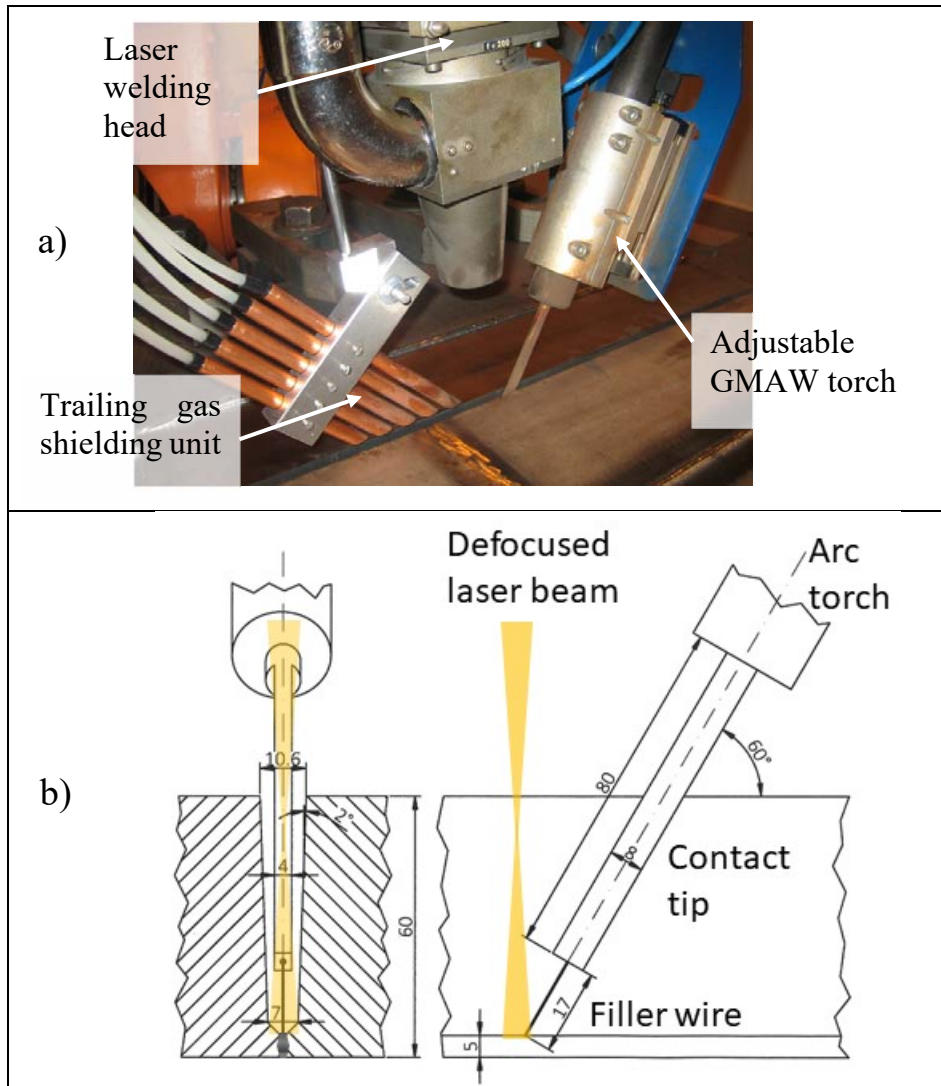


Figure 3.2: (a) Welding head set-up used in multi-pass laser-arc hybrid experiments. (b) Drawing presenting the principle of configuration used for the filling passes of multi-pass laser-arc hybrid welding with defocusing technique.

A Kemppi Pro 5200 gas metal arc welding (GMAW) machine was deployed in the laser arc-hybrid experiments. In laser-arc hybrid welding a pulsed arc mode and welding machine's synergy settings were utilized. In the laser cold-wire experiments, the filler wire was fed and guided through the same GMAW machine and torch as used in the laser-

arc hybrid experiments. A grounding cable shoe was disconnected from the fastening table to enable the use of cold-wire welding.

To execute required welding movements, a KUKA KR 15 articulated arm robot and a custom-built gantry-based X/Y/Z- linear movement station was used in welding experiments of Publication I&II and Publication III&IV, respectively.

In multi-pass laser-arc hybrid welding with defocusing technique proposed in Publication II, laser beam defocusing values were gradually increased within the corresponding groove width of a subsequent fill up pass in question. In Table 3-2 and Figure 3.3 there is given a detailed example how defocusing was used in the case of laser-arc hybrid multi-pass weld E2 presented in Publication II.

Table 3-2: Example showing details of defocusing technique used for multi-pass welding of test weld E2 presented in Publication II.

Multi-pass weld E2, layers	Laser beam defocusing, F [mm]	Diameter of laser beam spot \varnothing [mm]	Filler wire feeding rate [m/min]
Capping pass	+65	≈ 7.5	15
8 th fill up pass	+65	≈ 7.5	14
7 th fill up pass	+60	≈ 7.0	13
6 th fill up pass	+55	≈ 6.5	12
5 th fill up pass	+55	≈ 6.5	11.5
4 th fill up pass	+50	≈ 5.9	11
3 rd fill up pass	+50	≈ 5.9	10
2 nd fill up pass	+40	≈ 4.9	9.5
1 st fill up pass	+35	≈ 4.4	9.0
Root pass	0	0.6	12

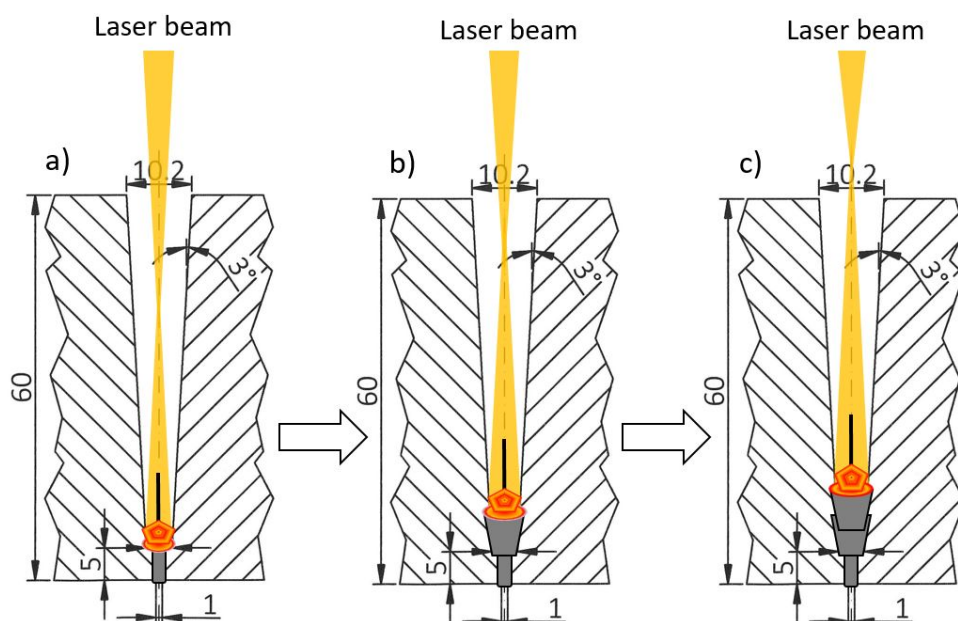


Figure 3.3: Drawing presenting a principle how laser-arc hybrid filling passes are produced in the case of multi-pass weld E2 presented in Publication II. Configurations for (a) the first fill up pass (F=+35); (b) the second fill up pass (F=+40); (c) the third fill up pass (F=+50).

In addition to visual weld inspections carried out with a naked eye and magnifying glass, the metallographic examination of the test welds were made from the etched transversal weld cross-sections using a light microscope. In the weld metal mixing investigations, EDS (Energy Dispersive Spectroscopy) analysis of selected weld cross-sections was done using a Hitachi SU3500 scanning electron microscope and Thermo Scientific Ultradry DSS EDS-detector. Both the EDS stepwise characterisation and EDS mapping techniques were utilised. The techniques are described in Publication IV in detail.

In modelling and simulation studies carried out in the Publication III, a commercially available computational fluid dynamics (CFD) simulation software FLOW-3D[®] from Flow Science Inc. was utilised (FLOW-3D[®], 2019). The numerical analysis and its corresponding process model were built on the FLOW-3D[®] version 9.2. No other commercial add-in software were used, instead several customised user subroutines developed by the South-Korean research team at Korea Advanced Institute of Science and Technology (KAIST) were utilised for the process models.

4 Overview of the publications and research findings

To solve the stated research problem and to answer to the principle research question of this thesis (in Chapter 1.4) each publication includes detailed objectives and hypotheses together with derived specific questions which are discussed in publications I-IV.

4.1 Publication I

Solidification cracking studies in multi pass laser hybrid welding of thick section austenitic stainless steel

Objective: The objective of the work was to develop a test set-up for the study of hot cracking in multi-pass laser hybrid welding of thick section austenitic stainless steel and use the test set-up in evaluation of the hot cracking susceptibility of welds produced with the special customised grade AISI 316L(N)-IG ITER.

Research hypotheses: In constructional arrangements of increased section thickness and high structural rigidity, the studied vessel base material AISI 316L(N)-IG ITER austenitic stainless steel grade is susceptible to hot cracking when the deposited weld metal favours primary austenitic solidification. A welding test set-up that takes advantage of the self-restraint imposed by the rigid configuration of the tested specimen can reveal hot cracking occurrence.

Research questions: Can the developed test set-up produce critical conditions that promote hot cracking in test welds produced with multi-pass laser-arc hybrid welding? Do the tested combination of base and filler metal indicate hot cracking susceptibility? Do the studied groove options (narrow/wide) and depth-to-width ratio of produced weld cross sections show different solidification cracking susceptibility for the studied base and filler metal combination?

Results and contribution to the whole

The results of the welding experiments showed that the developed test set-up can produce critical conditions to promote hot cracking in produced test welds of AISI 316L(N)-IG ITER grade in multi-pass laser-arc hybrid welding. Results confirmed that the used combination of the base and filler material compositions and welding process parameters favored primary austenitic solidification and led in fully austenitic weld metal microstructure. Although all produced individual filling passes had crack susceptible austenitic solidified microstructure and possessed calculated Cr/Ni-equivalent value be in the range of 1.3, the results indicated that the shape of the weld cross-section plays also a role in weld solidification cracking susceptibility. The test series which had narrower filling passes with large depth to width ratio tended to be more susceptible to hot cracking than the wider ones. The research carried out in the Publication I contributes with introducing new means and knowledge to assessing weldability of laser-arc hybrid multi-pass welding of thick-section austenitic stainless steels in respect with base metal

chemistry, produced weld geometry, base-metal dilution, filler metal selection and overall propensity to weld metal solidification cracking susceptibility.

4.2 Publication II

Defocusing techniques for multi-pass laser welding of austenitic stainless steel

Objective: The objective of the work was to study the feasibility of laser beam defocusing as a way to fill and bridge wider groove geometries than can be welded with focused keyhole mode welding with filler metal addition. The used defocusing technique was designed for application with multi-pass welding of thick austenitic stainless steel joints of up to 60 mm with single-side preparations.

Research hypotheses: The laser beam can be adjusted by adequate use of defocusing to enable to production of a broader weld fusion zone in order to accommodate welding of wider groove geometries than conventionally used in keyhole mode welding. The above defocusing technique can enable new approaches to laser-arc and laser filler wire welding of thick sections with multiple passes.

Research questions: How do different defocusing setting values affect the resulting fusion zone cross-section of the produced weld bead? How can defocusing be applied to filling and bridging of wide groove geometries of up to 60 mm joint thickness? Is there potential for using an intermediate laser power (~ 3 kW) and defocusing technique in thick section multi-pass welding?

Results and contribution to the whole

The welding experiments demonstrated that by using the described defocusing technique and conduction limited hybrid method in the welding of filling passes even a gap width of 11 mm can be bridged and filled. In order to avoid lack of fusion defects between the filling passes and the groove sidewalls, the size of the laser beam spot should be properly set to respect with the groove width to be welded. For example, in the case of 60 mm thick bevelled Y-shape groove, starting from the bottom of the groove, the size of the laser spot diameter has to be gradually increased while the build-up welding with filling passes is proceeding. In order to secure the sidewall fusion, the diameter of laser spot size needs to be adjusted by defocusing near to the same as the current groove width is in that particular groove depth.

Results showed that the groove filling efficiency is much better when using laser-arc hybrid welding than in laser welding with cold filler wire. Extra heat source of GMAW enables wire melting before it enters to the laser induced melt pool. When combining laser welding with cold filler wire for the first 20-25 mm weld thickness and then laser-arc hybrid welding for the rest upper 35-40 mm thickness, a total of 15 to 20 passes was needed to complete the 60 mm thick multi-pass weld. As the laser-arc hybrid multi-pass welding was used alone, from the root to the capping weld, it was managed to fill 60 mm

thick joint with the total of 10 passes. The research and development work of process optimization carried out in the Publication II contributes with offering new alternative procedure approach to enhancing efficiency in intermediate-power laser welding of thick section applications. In addition, capability to use wider groove geometries and produce wider weld fusion zones may help to scale down a weld solidification cracking susceptibility which is pointed out in Publication I to be a risk with deep and narrow weld deposits.

4.3 Publication III

Effect of leading and trailing torch configuration on mixing and fluid behavior of laser-gas metal arc hybrid welding

Objective: The aim of the work was to study filler metal mixing and fluid flow in single-pass welds done on 10 mm thick close square preparations of austenitic stainless steel plates using a laser-arc hybrid welding process with a leading and trailing arc torch. The mixing behavior of the filler and base metal is evaluated and compared based on both experimental studies and simulations. The objective of the work was to gain understanding of the melt flow behavior of laser-gas metal arc hybrid welding with the help of simulation. A topic of special interest was the effect of gas-metal-arc (GMA) torch orientation in hybrid welding and its influence on melt flow and weld metal mixing.

Research hypotheses: Simulations can offer enhanced understanding of weld pool mixing and in-depth knowledge related to different mixing behavior between trailing and leading torch configurations in laser-arc hybrid welding.

Research questions: Can simulation results offer explanations for the different mixing behavior observed for trailing and leading torch configurations in laser-arc hybrid welding?

Results and contribution to the whole

The simulation studies of full penetration fibre laser-arc hybrid welding of 10 mm thick closed butt-joint of austenitic stainless steel revealed characteristic weld pool flow patterns and temperature contours both for leading and trailing torch configuration. It was interpreted from the longitudinal sections extracted from the weld pool simulations that when the GMA torch in laser-arc hybrid welding is used with leading configuration, a solidification front at the mid-thickness area of freezing melt pool is proceeding as a lateral peninsula which sections the melt pool into upper and lower part. On the contrary, this behavior was not observed when simulation was carried out using GMA trailing torch configuration. The above mentioned solidification peninsula may obstruct the circulation of the melt flow between the weld surface and the root, which in turn may reduce the mixing of weld metal in the case of leading torch configuration. The explanation for the described different melt pool solidification can be that in the leading torch configuration, the filler metal droplets impinge in the leading edge of the laser induced melt pool,

whereas in the trailing torch configuration the arc heat and the filler metal droplets impinge into behind the laser beam where the molten pool is fully developed.

In additional simulations, tungsten particles were added as tracers into the simulated melt pool of trailing and leading torch simulations. It was found that when the particles were initially placed at the weld surface side and once the particles reached the weld bottom recirculation they were unable to reach the upper recirculation back when the leading torch was used. In the trailing torch configuration, however, the particles that were initially introduced in the surface part of the weld were able to reach the bottom recirculation and then returned back towards the upper recirculation. This phenomenon helps in the mixing of the melt in the trailing torch configuration. The simulation results concluded that in the trailing torch configuration, the flow recirculation is more pronounced, and therefore, mixing is more efficient than in the leading torch variation. The recirculation of melt at the root part will increase the mixing in the root part of the weld. The absence of such recirculation in the leading configuration was the main reason for having low mixing at the bottom part of the weld. The research carried out in the Publication III contributes with providing new knowledge about the mixing behavior of weld metals produced in thick section closed butt-joints in laser-arc hybrid welding. The key contribution in particular is the interpretation and explanations to the difference of mixing behavior between the leading and trailing torch configuration with the help of simulation studies.

4.4 Publication IV

Filler metal mixing behaviour of 10 mm thick stainless steel butt-joint welds produced with laser-arc hybrid and laser cold-wire processes

Objective: The aim of this study was to investigate filler metal mixing behavior in 10 mm thick joints of austenitic stainless steel in single-pass laser-arc hybrid and laser cold-wire welding processes. The objective was to examine the effect of groove geometry and filler wire feeding orientation on filler metal mixing in terms of the intensity and homogeneity of mixing throughout the weld cross-section from the weld surface to the root.

Research hypotheses: Mixing in weld metals can be inhomogeneous in single-pass thick section joints of laser-arc hybrid and laser cold-wire welding processes. Mixing can be studied using the methodologies described in the article. Wire feeding configuration (leading/trailing) and joint preparation have an effect on the behavior of filler metal mixing in the weld cross-sections produced.

Research questions: Can filler metal mixing at the root portion of the weld be enhanced by widening the root gap of an I-groove weld or by using a suitable V-groove? Can any difference be found between the results for leading or trailing wire feeding, that is, when the filler wire is introduced to the melt pool in front of or behind the laser beam with respect to the welding direction? Is there any noticeable difference in filler metal mixing behavior between laser-arc hybrid and laser cold-wire welding?

Results and contribution to the whole

Welding experiments conducted on 10 mm thick austenitic stainless steel butt-joints with I- and V-groove preparation showed that during the weld examination phase, an EDS elemental mapping also proved to be very beneficial tool along with an EDS stepwise characterization method for determining and assessing the filler metal mixing in produced weld cross-sections. The mixing results showed that welds produced in 10 mm thick closed root gap and in 0.4 mm open gap have considerable difference of filler metal mixing between the upper part and the lower part of the weld cross-section. This inhomogeneous distribution of filler metal could be clearly seen from the EDS elemental mapping images. Mentioned mixing behavior was discernible in both the leading and trailing wire feeding and it was more pronounced in laser welding with cold-wire if compared to laser-arc hybrid welding results. When the used root gap of I-groove was widened to the value of 0.8 mm, it clearly helped to introduce filler metal and its elements deep down into the weld root portion. In laser arc-hybrid welding both leading and trailing wire feeding configurations showed enhanced mixing behavior across the whole weld fusion zone. In laser welding with cold-wire, however, in contrary to the trailing wire feeding, the leading wire feeding still showed a distinct contrast of the filler metal distribution between the upper part and lower part of the weld cross-section. Utilization of 10 degree V-groove preparation with trailing wire feeding proved to be the best choice to provide efficient and homogeneous distribution of filler metal across the whole fusion zone in the case of laser cold-wire welding. On the other hand, in laser arc-hybrid welding the results showed that the use of V-groove preparation with both wire feeding configuration produced high level of filler metal mixing but the overall homogeneity of distribution across the whole fusion zone was not that good as it was in the laser-arc hybrid welds produced in I-groove with 0.8 mm root gap. The research carried out in the Publication IV contributes with providing new knowledge about filler metal mixing behavior when using different groove types and wire feeding configurations in laser-arc hybrid and laser cold-wire welding of thick sections. In addition, the research findings produced new means how filler metal mixing can be controlled and optimized using the adequate groove geometry and welding process parameters.

5 Conclusions

This article-based dissertation focuses on research and development of enhancing weldability aspects of thick section austenitic stainless steel in laser-arc hybrid and laser cold-wire welding. The studied joint thicknesses were between 10 mm and 60 mm. The Nd:YAG laser and ytterbium fibre laser used in the welding experiments were solid-state lasers operating in continuous wave mode and at 1 micrometre wavelength. The particular research emphases of weldability studies of the dissertation were arisen from the basis of the recognized research problem and the stated principle research question. The weldability studies carried out were focused on the following key-areas:

- A. Assessment of solidification cracking in multi-pass laser-arc hybrid welding.
- B. Enhancement of the process capabilities of welding thick-sections using adequate controlled defocusing of laser beam in laser-arc hybrid and cold-wire processes.
- C. Fostering of comprehension from mixing behavior in thick section laser welding with filler addition and the knowledge how to affect mixing homogeneity using adequate combination of groove geometry and process parameters.

The main research results and key findings with respect to the studied key-areas can be concluded as follows:

- A. A specific self-restraint welding test set-up was developed to help analysing solidification cracking susceptibility of welds in multi-pass laser welding. That will offer a method for assessing weldability of laser-arc hybrid multi-pass welding of thick-section austenitic stainless steels in respect with base metal chemistry, produced weld geometry, base-metal dilution, filler metal selection and overall propensity to weld metal solidification cracking susceptibility.
- B. The results from the welding experiments demonstrated that the developed defocusing technique with multi-pass procedure can offer new alternative approaches to enhancing efficiency in intermediate-power laser welding of thick section applications. In addition, capability to use wider groove geometries and produce wider weld fusion zones may help to scale down a weld solidification cracking susceptibility. The results showed that when defocusing technique is adequately used in conduction-limited regime with laser-arc hybrid welding, even a gap width of 11 mm can be bridged and filled during the build-up welding of filling passes.

Results showed that the groove filling efficiency is much better in laser-arc hybrid welding than in laser welding with cold wire. The capability of multi-pass welding

of 60 mm thick joints with single side preparation was successfully demonstrated with welding experiments. When combining laser welding with cold filler wire for the first 20-25 mm weld thickness and then adding laser-arc hybrid welding for the rest upper 35-40 mm thickness, a total of 15 to 20 passes was needed to complete the 60 mm thick multi-pass weld. In comparison, when the laser-arc hybrid multi-pass and defocusing technique was used alone from the root to the capping weld, it was managed to fill 60 mm thick joint with the total of 10 passes.

- C. The mixing behavior of 10 mm thick butt-joint welds of austenitic stainless steel was studied both with using empirical welding experiments and with the help of numerical simulations. The simulation studies propose an interpretation and explanations to the different mixing behavior between the leading and trailing torch configuration. The simulation studies of full penetration fibre laser-arc hybrid welding of 10 mm thick closed butt-joints revealed characteristic weld pool flow patterns and temperature contours both for leading and trailing torch configuration. The simulation results concluded that in the trailing torch configuration, the flow recirculation is more pronounced, and therefore, mixing is more efficient than in the leading torch variation. The recirculation of melt observed at the root part will increase the mixing in the root part of the weld. The absence of such recirculation in the leading configuration was the main reason for having low mixing at the bottom part of the weld.

The use of an EDS elemental mapping proved to be very beneficial tool along with an EDS stepwise characterization method for determining and assessing the filler metal mixing in produced weld cross-sections. The mixing results gained from the empirical welding experiments showed that welds produced in 10 mm thick closed root gap and in 0.4 mm open gap of an I-groove have considerable difference of filler metal mixing between the upper part and the lower part of the weld cross-section. Above mentioned mixing behavior was discernible in both the leading and trailing wire feeding and it was more pronounced in laser welding with cold-wire if compared to laser-arc hybrid welding results. When the used root gap of I-groove was widened to the value of 0.8 mm, the results indicated that it clearly helped to introduce filler metal and its elements deep down into the weld root portion: In laser arc-hybrid welding both leading and trailing wire feeding configurations showed enhanced mixing behavior across the whole weld fusion zone. In laser welding with cold-wire, however, in contrary to the trailing wire feeding, the leading wire feeding still showed a distinct contrast of the filler metal distribution between the upper part and lower part of the weld cross-section.

Utilization of 10 degree V-groove preparation with trailing wire feeding proved to be the best choice to provide efficient and homogeneous distribution of filler metal across the whole fusion zone in the case of laser cold-wire welding. On the other hand, in laser arc-hybrid welding the results showed that the use of V-groove preparation with both wire feeding configuration produced high level of filler metal mixing but the overall homogeneity of distribution across the whole fusion zone was not that good as it was in the laser-arc hybrid welds produced in I-groove with 0.8 mm root gap.

Above research findings provide new knowledge about filler metal mixing behavior when using different groove types and wire feeding configurations in laser-arc hybrid and laser cold-wire welding of thick sections. In addition, the findings provide new means how filler metal mixing can be controlled and optimized using the adequate groove geometry and welding process parameters.

6 Suggestions for further study

The following suggestions for further study can be considered in order to complement existing studies:

- Solidification cracking studies using the developed self-restraint set-up with the initial type 316L base material and two or three new comparative filler metal alloy candidates which possess a chemical composition providing Cr/Ni-equivalent values from 1.9 to 2.0. Depending on dilution rates of base material and filling passes, that would change the weld metal composition and the Cr/Ni-equivalent values into range of 1.8-1.9 which would favour primary ferrite solidification. According to theoretical background that will lead to lower solidification cracking susceptibility.
- Concerning the developed defocusing technique, the corresponding experimental studies would be beneficial to carry out using a 10 kilowatt fibre laser. The purpose of above experiments would be to demonstrate whether the capacity of higher laser power can be used to enhance welding speed and process productivity compared to 3 kilowatt laser power and welding speeds used in Publication II.
- Concerning the mixing studies a set of additional EDS examinations from the longitudinal weld cross-sections along the welded joints would be beneficial to carry out because they can supply more statistical augmentation to the interpretation of mixing. Moreover, it is suggested that the effect of a slight defocusing ($F=+20$) on the mixing in closed I-groove preparation should be further studied as a way to affect mixing behavior. In the results of preliminary experiments carried out with laser welding with cold-wire, which have not been published yet, it was seen that the use of defocusing setting with $F=+20$, levels down the abrupt filler metal mixing inhomogeneity observed in Publication IV in the case of normal focal setting with $F= - 4$.

References

Ahn, H. J., Kim, B. C., Sa, J. W., Lee, Y. J., Hong, K. H., Kim, H. S., Bak, J. S., Jung, K. J., Park, K. H., Kim, T. S., Lee, J. S., Kim, Y. K., Sung, H. J., Ioki, K., Giraud, B., Choi, C. H., Utin, Y. (2011). Fabrication design and code requirements for the ITER Vacuum Vessel, In: *Proceedings of the ASME 2011 Pressure Vessels & Piping Division Conference*, PVP2011-57143, July 17-21, 2011, Baltimore, Maryland, USA, pp. 1-9.

Arata, Y., Maruo, H., Miyamoto, I., and Nishio, R. (1986). High power CO₂ laser welding of thick plate, multipass welding with filler wire," *Transaction of JWRI*, vol 15, no 2, pp. 199-206.

Arnoux, R. (2018). ITER NEWSLINE: *Vacuum vessel welding - Rehearsing a grand production* [web document]. [Retrieved March 28, 2019]. Available at: <https://www.iter.org/newsline/-/3178>.

ANSI/AWS A3.0-89, *Standard Welding Terms and Definitions*, American National Standard, American Welding Society, Miami Florida, USA, 1989, 109 p.

Baker, R.G. (1975). Weldability and its implications for materials requirements, In: *Rosenhain Centenary Conference Proceedings, 1975*, p.129.

Barabash, V. (2003). Material Specification for the supply of 316L(N)-IG austenitic stainless steel plates, G 74 SP 12 03-07-09 W 0.1, Rev.2- 08.07.2003.

Borland, J.C. and Younger, R.N. (1960). Some Aspects of Cracking in Welded Cr-Ni Austenitic Steels, British Welding Research Association Report, *British Welding Journal*, January 1960, pp. 22-59.

Brooks J.A., Thompson, A.W. and Williams, J.C. (1984). A fundamental study of the beneficial effects of delta ferrite in reducing weld cracking, *Welding Journal* 63(3):71s-83s.

Brooks, J.A. and Thompson, A.W. (1991). Microstructural development and solidification cracking susceptibility of austenitic stainless steel weld, *International Materials Reviews*, Vol. 36, No. 1, pp. 16-44.

Choi, C.H., Sborchia, C., Ioki, K., Giraud, B., Utin, Yu., Sa, J.W., Wang, X., Teissier, P., Martinez, J.M., Le Barbier, R., Jun, C., Dani, S., Barabash, V., Vertongen, P., Alekseev, A., Jucker, P., Bayon, A., Pathak, H., Raval, J., Ahn, H.J., Kim, B.C., Kuzmin, E., Savrukhin, P. (2014). Status of the ITER vacuum vessel construction, *Fusion Engineering and Design*, 89, pp. 1859–1863.

Cieslak, M.J., Ritter, A.M., Savage, W.F. (1982). Solidification Cracking and Analytical Electron Microscopy of Austenitic Stainless Steel Weld Metals, *Welding Journal*, January 1982, Welding research supplement, pp. 1s-8s.

- Cross, C.E. (2005). On the Origin of Weld Solidification Cracking, In: *Hot Cracking Phenomena in Welds*, Eds. Lippold, J., Boellinghaus, T. and Cross, C., 1st ed., Germany: Springer-Verlag Berlin Heidelberg, pp. 3-18.
- David, S.A., Vitek, J.M. and Hebble, T.L. (1987). Effect of Rapid Solidification on Stainless Steel Weld Metal Microstructures and Its Implications on the Schaeffler Diagram, *Welding Journal* 66(10): 289s-300s.
- David, S.A. and Vitek, J.M. (1989). Correlation between solidification parameters and weld microstructures, *International Materials Review*, Vol. 34, No. 5, pp. 213-245.
- DeLong, W.T., Ostrom, G.A. and Szumachowski, E.R. (1956). Measurement and Calculation of Ferrite in Stainless Steel Weld Metal, *Welding Journal* 35: 521s-528s.
- Dilthey, U., Keller, H., Ghandehari, A. (1999). Laser beam welding with filler metal. *Steel Research*, 70, pp. 199-202.
- Dilthey, U., Wiesschemann, A. (2003). Perspectives offered by combining a laser beam with arc welding procedures, *Welding International*, 16, pp. 711-719.
- Dulon, K. (2015). ITER NEWSLINE: *Preparing for the challenges of vacuum vessel welding* [web document]. [Retrieved March 28, 2019]. Available at: <https://www.iter.org/newsline/-/2340>.
- Easterling, K. (1983). In: *Introduction to the Physical Metallurgy of Welding*, Butterworths & Co Ltd, 231 p.
- Elmer, J.W. (1988). *The Influence of Cooling Rate on the Microstructure of Stainless Steel Alloys*, Ph.D Thesis, Lawrence Livermore National Laboratory, University of California, Livermore, California, USA, 388 p.
- Elmer, J., Hochanadel, P., Lachenberg, K., Webber, T. (2009). Introduction to High Energy Density Electron and Laser Beam Welding, In: *American Society for Metals Welding Handbook*, 11 edition. pp. 1-15.
- EN-ISO 12932 (2013). Welding - Laser-arc hybrid welding of steels, nickel and nickel alloys - Quality levels for imperfections (ISO 12932:2013), Geneva, Switzerland, 38 p.
- FLOW-3D® Version 9.2 [Computer software]. (2019). Santa Fe, New Mexico, U.S.A.: Flow Science, Inc. <https://www.flow3d.com/>
- Folkhard, E. (1988). In: *Welding metallurgy of stainless steels*, New York, Springer-Verlag, 279 p.
- Gook, S., Gumenyuk, A., Rethmeier, M. (2014). Hybrid laser arc welding of X80 and X120 steel grade. *Science and Technology of Welding and Joining*, 19:1, pp. 15-24.

- Gook, S., Forquer, M., Gumenyuk, A., Rethmeier, M., El-Batahgy, A.M. (2015). Laser and Hybrid Laser-Arc Welding of Cryogenic 9% Ni Steel for Construction of LNG Storage Tanks, In: *3rd International Conference in Africa and Asia on Welding and Failure Analysis of Engineering Materials*, WAFA 2015. November 2-5, 2015, Luxor, Egypt. pp. 1-12.
- Gook, S., Gumenyuk, A., Rethmeier, M. (2018). Orbital hybrid laser arc welding using a high power fibre laser for pipeline construction, *Global Nuclear Safety* 26, No.1, pp. 45-54.
- Griffith, S. (2012). ITER NEWSLINE 248. *Bring in the welders* [web document]. [Retrieved March 28, 2019]. Available at: <https://www.iter.org/newsline/248/1414>
- Grupp M., Klinker, K., Cattaneo S. (2013). Welding of high thicknesses using a fibre optic laser up to 30 kW, *Welding International*, 27:2, pp. 109-112.
- Guirao, J., Rodríguez, E., Bayón, A., Jones, L. (2009). Use of a new methodology for prediction of weld distortion and residual stresses using FE simulation applied to ITER vacuum vessel manufacture, *Fusion Engineering and Design*, 84, pp. 2187-2196.
- Hammar, Ö. and Svensson, U. (1979). In: *Solidification and casting of metals*. The Metals Society, London, pp. 401-410.
- Hemsworth, B., Boniszewski, T. and Eaton, N.F. (1969). Classification and definition of high temperature welding cracks in alloys, *Metal Construction and British Welding Journal*, Feb.1969, pp. 5-16.
- Hull, F.C. (1967). The effect of δ -ferrite on the hot cracking of stainless steels, *Welding Journal* 46:399s-409s.
- Hull, F.C. (1973). Delta Ferrite and Martensite Formation in Stainless Steels, *Welding Journal* 52: 193s-203s.
- Ioki, K., Choi, C.H., Daly, E., Dani, S., Davis, J., Giraud, B., Gribov, Y., Hamlyn-Harris, C., Jones, L., Jun, C., Kim, B.C., Kuzmin, E., Le Barbier, R., Martinez, J.-M., Pathak, H., Preble, J., Reich, J., Sa, J.W., Terasawa, A., Utin Yu., Wang, X., Wu, S. (2012). ITER Vacuum Vessel design and construction, *Fusion Engineering and Design*, 87, pp. 828-835.
- Ion, J.C. (2005). *Laser processing of engineering materials – principles, procedures and industrial applications*. Elsevier Butterworth-Heinemann, 556 p.
- ISO/TR 581:2005. *Weldability - Metallic materials - General principles*, The International Organization for Standardization, Geneva, Switzerland, 4 p.

- Jokinen, T., Karhu, M., Kujanpää, V. (2003). Welding of thick austenitic stainless steel using Nd:yttrium–aluminum–garnet laser with filler wire and hybrid process, *Journal of Laser Applications*, 15, pp. 220-224.
- Jones, L.P., Aubert, P., Avilov, F., Coste, F., Daenner, W., Jokinen, T., Nightingale, K.R., Wykes, M. (2003). Towards advanced welding methods for the ITER vacuum vessel sectors, *Fusion Engineering and Design*, 69, pp. 215-220.
- Jones, L., Bianchi, A., Cros, A., di Pietro, E., Giraud, B., Ioki, K., Junek., L., Parodi, B., Pick, M., Sanguinetti, G-P., Tivey, R., Utin, Y. (2005). ITER vacuum vessel sector manufacturing development in Europe, *Fusion Engineering and Design*, 75-79, pp. 607-612.
- Karhu, M., Kujanpää, V. (2008). *TW6-TVA-IHYB, Industrialisation and weld quality issues of high productive laser\arc hybrid for thick section welding of ITER grade SS material*. Research report VTT-R-07448-08, Lappeenranta, Finland, 40 p.
- Karhu, M., Kujanpää, V., Gumenyuk, A., Lammers, M. (2013). Study of Filler Metal Mixing and Its Implication on Weld Homogeneity of Laser-Hybrid and Laser Cold-Wire Welded Thick Austenitic Stainless Steel Joints, In: *Proceedings of 32nd International Congress on Applications of Lasers & Electro-Optics*, Miami, FL USA. October 6-10, pp. 252-261.
- Katayama, S. and Matsunawa, A. (1984). Solidification Microstructure of Laser Welded Stainless Steels, In: *Proceedings of the International Conference on Applications of Lasers and Electro-optics*, ICALEO'84, Boston, USA, pp. 60-67.
- Katayama, S. and Matsunawa, A. (1985). Solidification behaviour and microstructural characteristics of pulsed and continuous laser welded stainless steels, In: *Proceedings of the International Conference on Applications of Lasers and Electro-optics*, ICALEO'85, San Francisco, USA, pp. 19-25.
- Katayama, S. (2013). *Handbook of Laser Welding Technologies*, Ed. Katayama S., Woodhead Publishing Limited. 632 p.
- Katayama, S., Mizutani, M., Kawahito, Y., Ito, S., Sumimori, D. (2015). Fundamental Research of 100 kW Fiber Laser Welding Technology, In: *LiM- Lasers in Manufacturing Conference*, June 22-25, 2015 Munich, Germany. Pp. 1-8.
- Kawahito, Y., Mizutani, M., Katayama, S. (2009). High quality welding of stainless steel with 10 kW high power fibre laser. *Science and Technology of Welding and Joining*, 14:4, pp. 288-294.
- Kim, B.C., Lee, Y.J., Hong, K.H., Sa, J.W., Kim, H.S., Park, C.K., Ahn, H.J., Bak, J.S., Jung, K.J., Park, K.H., Roh, B.R., Kim, T.S., Lee, J.S., Jung, Y.H., Sung, H.J., Choi, S.Y.,

- Kim, H.G., Kwon, I.K., Kwon, T.H. (2013). Fabrication progress of the ITER vacuum vessel sector in Korea, *Fusion Engineering and Design*, 88, pp. 1960-1964.
- Koga, H., Goda, H., Terada, S., Hirota, K., Nakayama, S., Tsubota, S. (2010). First Application of Hybrid Laser-arc Welding to Commercial Ships, *Mitsubishi Heavy Industries Technical Review* Vol. 47 No. 3, pp. 59-64.
- Koizumi, K., Nakahira, M., Itou, Y., Tada, E., Johnson, G., Ioki, K., Elio, F. (1998). Design and development of the ITER vacuum vessel, *Fusion Engineering and Design*, 41, pp. 299–304.
- Kou, S. (2003). In: *Welding Metallurgy*, 2nd ed.; John Wiley & Sons, Inc.: Hoboken, New Jersey, U.S.A., pp. 103–107.
- Kotecki, D.J. and Siewert, D.T.A. (1992). WRC-92 constitution diagram for stainless steel weld metals: a modification of the WRC-1988 diagram. *Welding Journal* 71:5, pp.171s-178s.
- Kristensen, J. K. (2013). Applications of laser welding in the shipbuilding industry, Part IV Applications of laser welding. In *Handbook of Laser Welding Technologies*, Ed. Katayama S., Woodhead Publishing Limited, pp. 596-611.
- Kujanpää, V., Suutala, N., Takalo, T. and Moisio, T. (1979). Correlation between solidification cracking and microstructure in austenitic and austenitic-ferritic stainless steel weld, *Welding Research International*, 9(2):55, pp. 55-76.
- Kujanpää, V. (1984). Studies on Weld Defects in Austenitic Stainless Steels, Doctoral thesis, University of Oulu, Finland.
- Kujanpää, V.P., David, S.A. and White, C.L. (1986). Formation of Hot Cracks in Austenitic Stainless Steel Welds – Solidification Cracking, *Welding Journal, welding research supplement*, August, pp. 203s-212s.
- Kujanpää, V.P., Helin, J.P., Moisio, T.J.I., Bruck, G.J. (1990). Composition and Microstructure of Laser Beam Welds Between Dissimilar Metals, *Journal of Laser Applications*, 2, pp. 24-30.
- Kujanpää, V. (2014). Thick-section laser and hybrid welding of austenitic stainless steels, *Physics Procedia* 56, pp. 630-636.
- Kurz, W. and Trivedi, R. (1995). Modern Solidification Theory Applied to Welding, In: *Trends in Welding Research, Proceedings of the 4th International Conference*, Tennessee, USA, June 5-8, pp. 115-120.
- Lippold, J.C. (1985). Centerline Cracking in Deep Penetration Electron Beam Welds in Type 304L Stainless Steel, *Welding Journal*, 64(5), pp. 127s-136s.

- Lippold, J. C. (2005). In: *Welding Metallurgy and Weldability of Stainless Steels*, John Wiley & Sons, Inc.: Hoboken, New Jersey, U.S.A., 357 p.
- Lippold, J. C. (2015). In: *Welding Metallurgy and Weldability*, John Wiley & Sons, Inc.: Hoboken, New Jersey, U.S.A., 400 p.
- Liu, C., Yanga, J., Shia, Y., Fub, Q., Zhao, Y. (2018). Modelling of residual stresses in a narrow-gap welding of ultra-thick curved steel mockup, *Journal of Materials Processing Tech.* 256, pp.239-246.
- Masumoto, I., Tamaki, K. and Kutsuna, M. (1972). Hot cracking of austenitic steel weld metal, *Yosetsu-Gakki-shi*, (41), pp. 1306-1314, (Brutcher Transl. 8965/1973).
- Matsuda, F., Nakagawa, H., Uehara, T., and Katayama, S. (1979). A New Explanation for Role of Delta-Ferrite Improving Weld Solidification Crack Susceptibility in Austenitic Stainless Steel, *Transactions of JWRI*, Vol. 8, No. 1, pp. 105-112.
- Matsuda, F., Nakagawa, H., Katayama, S. and Arata, Y. (1982). Solidification Crack Susceptibility in Weld Metals of Fully Austenitic Stainless Steels (Report VII), *Transactions of JWRI*, Vol. 11, No. 2, pp. 79-94.
- Ohnishi, T., Kawahito, Y., Mizutani, M., Katayama, S. Butt welding of thick, high strength steel plate with a high power laser and hot wire to improve tolerance to gap variance and control weld metal oxygen content, *Science and Technology of Welding and Joining*, 18, pp. 314-322.
- Pacary, G., Moline, M., and Lippold, J.C. (1990). *A Diagram for Predicting the Weld Solidification Cracking Susceptibility of Pulsed-Laser Welds in Austenitic Stainless Steels*, EWI Research Brief B9008.
- Peng, W., Jiguo, S., Shiqing, Z., Gang, W. (2016). Control of wire transfer behaviors in hot wire laser welding, *International Journal of Advanced Manufacturing Technology*, 83, pp. 2091-2100.
- Ploshikhin, V., Prikhodovsky, A., Makhutin, M., Ilin, A. and Zoch, H.-W. (2005). Integrated Mechanical-Metallurgical Approach to Modelling of Solidification Cracking in Welds, In: *Hot Cracking Phenomena in Welds*, pp. 223-244. Eds. Lippold, J., Boellinghaus, T. and Cross, C., 1st ed., Germany: Springer-Verlag Berlin Heidelberg.
- Rethmeier, M., Gook; S., Lammers, M., Gumenyuk, A. (2009). Laser-Hybrid Welding of Thick Plates up to 32 mm Using a 20 kW Fibre Laser, *Quarterly Journal of the Japan Welding Society*, 27: 2, pp. 74-79.
- Rominger, V., Koitzsch, M., Kuhn, V., Gottwald, T., Stolzenburg, C., Holzer, M., Schad, S-S., Killi, A., Ryba, T. (2015). Latest trends in high power disk laser technology, In:

- LiM- Lasers in Manufacturing Conference*, June 22-25, 2015 Munich, Germany. Pp. 1-6.
- Salminen, A.S. and Kujanpää, V.P. (1995). Effect of heat input on the positional tolerances of fire feeding during laser welding, In: *Proceedings of the laser materials processing conference ICALEO '95*, pp. 534-543.
- Salminen, A.S., Kujanpää, V.P. (2003). Effect of wire feed position on laser welding with filler wire, *Journal of Laser Applications*, 15, pp. 1-9.
- Schaeffler, A.L. (1949). Constitution Diagram for Stainless Steel Weld Metal, *Metal Progress* 56: 680 and 680B.
- Suutala, N. and Moisio, T. (1980). The use of chromium and nickel equivalents in considering solidification phenomena in austenitic stainless steels, In: *Solidification technology in the foundry and cast house*, The Metals Society, 15-17 September 1980, University of Warwick, Coventry, UK, pp. 1-17.
- Suutala, N. (1982a). Effect of manganese and nitrogen on the solidification mode in austenitic stainless steel welds, *Metallurgical Transactions A*, Vol. 13A, pp. 2121-2130.
- Suutala, N. (1982b). Solidification Studies on Austenitic Stainless Steels, Doctoral thesis, University of Oulu, Finland.
- Suutala, N. (1983). Effect of solidification conditions on the solidification mode in austenitic stainless steels, *Metallurgical Transactions A*, Vol. 14A, pp. 191-197.
- Turichin, G., Kuznetsov, M., Tsubulskiy, I., Firsova, A. (2017). Hybrid Laser-Arc Welding of the High-Strength Shipbuilding Steels: Equipment and Technology, *Physics Procedia*, 89, pp. 156-163.
- Üstündag, Ö., Avilov, A., Gumenyuk, A., Rethmeier, M. (2018). Full penetration hybrid laser arc welding of up to 28 mm thick S355 plates using electromagnetic weld pool support, In: *IOP Conf. Series: Journal of Physics: Conf. Series* 1109, 012015, pp. 1-8.
- Üstündag, Ö., Avilov, A., Gumenyuk, A., Rethmeier, M. (2019). Improvement of Filler Wire Dilution Using External Oscillating Magnetic Field at Full Penetration Hybrid Laser-Arc Welding of Thick Materials, *Metals*, 9, 594, pp. 1-10.
- Victor, B., Nagy, B., Ream, S., Farson, D. (2009). High Brightness Hybrid Welding of Steel, In: *Proceedings of 28th International Congress on Applications of Lasers & Electro-Optics*, Orlando, FL USA. November 2-5, pp. 79-88.
- Wahba, M., Mizutani, M., Katayama, S. (2016). Hybrid laser-arc welding with backing and cut-wire, In: *9th International Conference on Photonic Technologies - LANE 2016*. September 19-22, 2016 Fürth, Germany. Pp. 1-6.

- Wester, S., Kristensen, J.K., Petring, D. (2008). Joining of thick section steels using hybrid laser welding, *Ironmaking & Steelmaking*, 35: 7, pp. 496-504.
- Westin, E., Stelling, K., Gumenyuk, A. (2011). Single-pass laser-GMA hybrid welding of 13.5 mm thick duplex stainless steel. *Welding in the World*, 55, pp. 39-49.
- Xiao, W., Li, Z., Zhang, F., Dai, K., Xian, Z., Xue, Y., Chen, B. (2015). Effect of heat input on cryogenic toughness of 316LN austenitic stainless steel NG-MAG welding joints with large thickness. *Materials and Design*, 86, pp. 160-167.
- Yang, W., Xin, J., Fang, C., Dai, W., Wei, J., Wu, J., Song, Y. (2019). Microstructure and mechanical properties of ultra-narrow gap laser weld joint of 100 mm-thick SUS304 steel plates, *Journal of Materials Processing Technology*, 265, pp. 130-137.
- Zhang, J., Niu, J., Xu, Z., Zhang, W. (2011). Transient welding distortions of the thick-wall pipes circumferentially welded by all-position narrow gap TIG welding, *Transactions of JWRI*, Special Issue on WSE2011, pp. 67-70.
- Zhang, M., Chen, G., Zhou, Y., Liao, S. (2014). Optimization of deep penetration laser welding of thick stainless steel with a 10 kW fiber laser, *Materials and Design*, 53, pp. 568-576.
- Zhang, X. (2013). Developments in multi-pass welding technology with filler wire. In: *Handbook of Laser Welding Technologies*, Ed. Katayama S., Woodhead Publishing Limited. pp. 459-477.
- Zhang, X., Mi, G., Chen, L., Jiang, P., Shao, X., Wang, C. (2018). Microstructure and performance of hybrid laser-arc welded 40mm thick 316 L steel plates, *Journal of Materials Processing Technology*, 259, pp. 312-319.

Part II: Publications

Publication I

Karhu, M., and Kujanpää, V.

Solidification cracking studies in multi pass laser hybrid welding of thick section austenitic stainless steel

Reprinted with permission from

Hot Cracking Phenomena in Welds III, Böllinghaus T., Lippold J., Cross C. (eds)

pp. 161-182, 2011

© 2011, Springer, Berlin, Heidelberg

Solidification Cracking Studies in Multi Pass Laser Hybrid Welding of Thick Section Austenitic Stainless Steel

Miikka Karhu and Veli Kujanpää

Introduction

VTT- Technical Research Centre of Finland has carried out several R&D sub-tasks during the international FUSION technology program in which a suitable welding method has been considered for the manufacturing of vacuum vessel for International Thermonuclear Experimental Reactor (ITER). The tasks have been involved hybrid Nd:YAG laser and electron beam welding. Because the walls of vacuum vessel will be made of 60 mm thick stainless steel, above mentioned high energy density beam processes have shown great potential of being high efficient joining method. In work of R&D tasks, the laser welding with filler wire and the hybrid welding were used in welding of thick section austenitic stainless steel for a very narrow gap and using a multi pass technique. The results have shown that by using the narrow groove with one pass per layer procedure the number of passes can be decreased significantly and the efficiency of the welding can be increased. In addition, the total heat input stays smaller than in conventional arc welding processes, which leads to lesser welding distortions.

Despite the successful welding process development it has been realized that metallurgical issues like occurrence of weld solidification cracking could cause troubles if it is not taken care of with certain precautions which means e.g. carefully selected weld chemistry. In the tests of basic AISI 304L and AISI 316LN laser and hybrid laser multi pass welding experiments, clear indication of hot cracking was seen in many test welds [1]. Therefore it may be well judged that used vessel material AISI 316L(N)-IG ITER steel grade could be susceptible to hot cracking, if other conditions favoring hot cracking, e.g. increased section thickness and rigidity of structure to be welded, primary austenitic weld solidification, etc. are present [2–5]. Stem from above mentioned observations, a hot cracking study was conducted. The purpose of the study was to develop a test set-up for studying hot cracking in multi pass laser hybrid welding of thick section austenitic stainless

M. Karhu (✉)

VTT-Technical Research Centre of Finland, FI-53851 Lappeenranta, Finland e-mail: miikka.karhu@vtt.fi

steel and then use this set-up for evaluation of hot cracking susceptibility of welds produced into the special customized heat AISI 316L(N)-IG ITER-grade by using certain reference filler wire material (THERMANIT 19/15). The concept of the test set-up was to use a straight forward approach in designing: It was built a very rigid clamping table together with fastening system and a test piece-design which is very rigid itself and produces self restraint.

Experimental Procedures

Materials

Parent material used in the experiments was a specially customized heat AISI 316L(N)-IG ITER-grade austenitic stainless steel. Concerning chemical composition of the ITER-grade stainless steel, it is specified to be inside certain limits and it is known as a nominal chemical composition, Table 1. Filler wire used in the experiments was an austenitic stainless steel wire THERMANIT 19/15 with a diameter of 1.2 mm. Regarding the test materials used in this experiments both parent and filler material is from the known heat and known chemical composition according to EN 10204-3.1. The exact chemical compositions of the materials are shown in Table 2.

Initial Assessment of Weldability for Parent and Filler Material

Various constitutional diagrams have been developed in order to evaluate a weldability of stainless steels [7–11]. For example, the use of those diagrams could help

Table 1 Nominal chemical composition (wt-%) of AISI 316L(N)-IG stainless steel. [6]

Element	Min	Max
C	0.015	0.030
Mn	1.6	2.0
Si	–	0.50
P	–	0.025
S	0.005	0.01
Cr	17.0	18.0
Ni	12.0	12.5
Mo	2.30	2.70
Ti ^a	–	0.15
Ta	–	0.01
Nb	–	0.01
Cu	–	0.3
B	–	0.0020
Co	–	0.05
N	0.060	0.080

^aNb+Ta+Ti < 0.15 wt%

Table 2 Exact chemical composition (wt-%) of the parent material AISI 316L(N)-IG and filler wire material THERMANIT 19/15 according to EN 10204-3.1

Element	AISI 316L(N)-IG	THERMANIT 19/15
C	0.025	0.015
Mn	1.7	7.32
Si	0.36	0.46
P	0.021	0.013
S	0.0001	0.005
Cr	17.6	20.18
Ni	12.2	15.08
Mo	2.41	2.79
Ti	0.005	–
Ta	0.003	–
Nb	0.005	–
Cu	0.1	0.095
B	0.0004	–
Co	0.03	0.016
N	0.067	0.187

to predict as-welded microstructure and avoid unfavorable parent material or filler material compositions which could lead e.g. to solidification mode or microstructure favoring hot cracking. The diagrams are based on chromium (Cr_{eq}) and nickel (Ni_{eq}) equivalents and their ratio (Cr_{eq}/Ni_{eq}) which can be calculated when a chemical composition of parent material and filler material is available. In the case of conventional arc welding where solidification rate is slow, it is found that if the ratio of chromium and nickel equivalent (Cr_{eq}/Ni_{eq}) in weld metal is below a certain level, e.g. 1.5, the susceptibility for solidification cracking is much higher than in welds where chromium and nickel equivalent ratio is above 1.5. The critical ratio is depending on the solidification rate such that at the higher solidification rates the critical ratio is slightly increased ($Cr_{eq}/Ni_{eq} \sim 1.7$). This is observed to be case e.g. in laser or electron beam welding. The impurities, especially sulphur and phosphorus also play a role in the susceptibility of hot cracking. If the impurity content is very low, below 0.01%, the susceptibility is much decreased [12–18].

The hot cracking susceptibility is also dependent on the level of strains affected by the rigidity of the structure. If the structure is thick and very rigid, stresses induced by welding heat in-put, are less likely become relieved by deformation of the structure. If deformations are hindered, strains could become stronger and more concentrated in the welding zone. In above case the strains causing hot cracking develop much easier [2, 3]. Furthermore, it is commonly recognized that in applications, where fully austenitic stainless steel welds are in certain specific reason required (e.g. anti-magnetic requirements etc.), hot cracking in weld metals could cause remarkable problems.

For the above reasons the ordinary austenitic stainless steel composition is often balanced such that usually ordinary AISI 316L or AISI 316LN composition is on the safe composition range, i.e. the ratio of chromium and nickel equivalents is over 1.5, which should ensure that solidification is primary ferritic resulting in approx. 5–15% delta ferrite in the weld metal at room temperature. This has been observed

to prohibit hot cracking. Another import factor for hot cracking prevention is reduction of impurity content (S+P); for safety reason it is usually limited to 0.03 ... 0.04%.

Initial requirement governed by the ITER-application was a fully austenitic microstructure for the base and weld metal. Therefore it was anticipated that there could be a risk for weld solidification cracking. Consequently, initial assessments of weldability were made using chromium and nickel equivalents. The ratio of chromium and nickel equivalents in used vacuum vessel material ITER grade austenitic stainless steel AISI 316L(N)-IG was calculated according to nominal chemical composition and for five different chromium and nickel equivalent equations, Tables 1 and 3.

Calculations revealed that depending on the variation of the element contents, Cr_{eq}/Ni_{eq} -ratio is in the range of 1.15–1.68. This indicates potential risk of hot cracking, especially when Cr_{eq}/Ni_{eq} -ratio remains lower than 1.5. The resulting regions defined by points of calculations are plotted in xy-coordinate which is featured in Fig. 1. Depending on obtained heat, marked areas in Fig. 1 gives an idea, how much the range of Cr_{eq} – and Ni_{eq} –ratios can vary in AISI 316L(N)-ITER grade within the permissible composition range (according the Table 1).

Furthermore, chromium and nickel equivalents according to exact chemical compositions (Table 2) for both parent material and filler material were calculated. In that case, only Hammar & Svensson diagram was decided to use, because it will best correlate weld solidification conditions [19].

It can be seen from the diagram in Fig. 2, that produced weld metal will follow the segment line starting from point 1.5 and moving along the segment line towards to point 1.2 depending on dilution ratio. Consequently, produced weld metal will have even smaller Cr_{eq}/Ni_{eq} -ratio than 1.5, because of used filler material. For example, if dilution rate of 40% is assumed, weld metal will have a Cr_{eq}/Ni_{eq} -ratio of 1.3, which means possible risk of hot cracking tendency.

Table 3 Chromium and nickel equivalents provided by different authors [7–11]

Author / name of diagram	Chromium equivalent (Cr_{eq})	Nickel equivalent (Ni_{eq})
Schaeffler	$Cr_{eq} = Cr + Mo + 1.5 \cdot Si + 0.5 \cdot Nb$	$Ni_{eq} = Ni + 0.5 \cdot Mn + 30 \cdot C$
DeLong	$Cr_{eq} = Cr + Mo + 1.5 \cdot Si + 0.5 \cdot Nb$	$Ni_{eq} = Ni + 0.5 \cdot Mn + 30 \cdot C + 30 \cdot N$
Hull	$Cr_{eq} = Cr + 1.21 \cdot Mo + 0.48 \cdot Si + 0.14 \cdot Nb + 2.20 \cdot Ti + 0.72 \cdot W + 0.21 \cdot Ta + 2.27 \cdot V + 2.48 \cdot Al$	$Ni_{eq} = Ni + [0.11 \cdot Mn - (0.0086 \cdot Mn^2)] + 24.5 \cdot C + 18.4 \cdot N + 0.44 \cdot Cu + 0.41 \cdot Co$
Hammar & Svensson	$Cr_{eq} = Cr + 1.37 \cdot Mo + 1.5 \cdot Si + 2 \cdot Nb + 3 \cdot Ti$	$Ni_{eq} = Ni + 0.31 \cdot Mn + 22 \cdot C + 14.2 \cdot N + Cu$
WRC-1992 (by Kotecki & Sievert)	$Cr_{eq} = Cr + Mo + 0.7 \cdot Nb$	$Ni_{eq} = Ni + 35 \cdot C + 20 \cdot N + 0.25 \cdot Cu$

Fig. 1 Chromium (Cr_{eq}) and nickel (Ni_{eq}) equivalents of ITER grade austenitic stainless steel AISI 316L(N)-IG was calculated according to nominal compositions and five different equations. Equivalent regions are coordinated as a chart

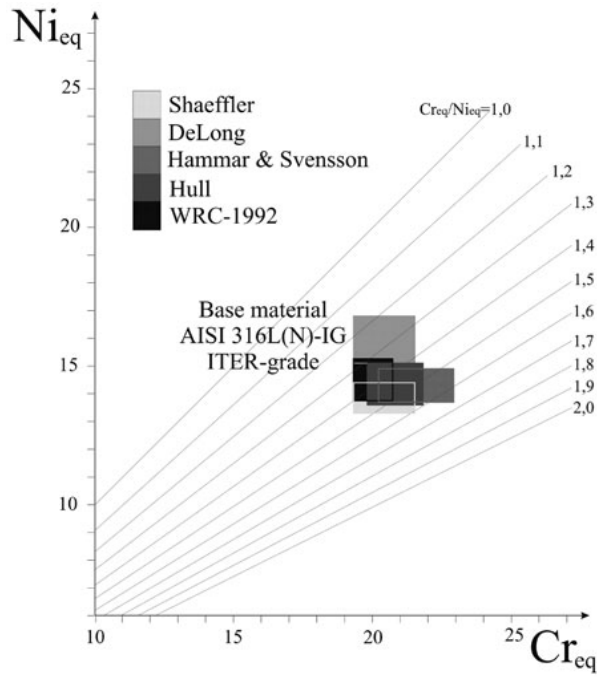
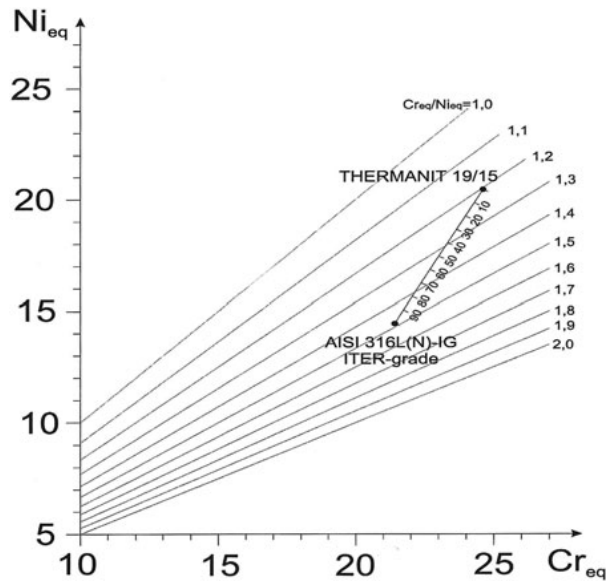


Fig. 2 Cr_{eq} and Ni_{eq} values of parent (AISI 316LN-IG) and filler material (Thermanit 19/15) placed in Hammar & Svensson diagram



Hot Cracking Test Set-Up: Rigid Clamping Table and Test Piece Design

Test set-up was decided to be designed and built in order to evaluate hot cracking susceptibility of ITER-grade heat AISI 316 L(N)-IG austenitic stainless steel when it is being narrow gap multi pass laser hybrid welded under very rigid conditions.

A very rigid clamping system was designed and built in order to emulate rigid welding conditions and strains which can occur in massive components assembly welding. The test system consists of rigid 170 mm thick table and clamping system for that. In clamping system, the total of 6 pieces of \varnothing 30 mm diameter high strength bolts together with 40 mm thick holder blocks was used to minimize angular distortions caused by welding heat. Each bolt was tightened into the moment of 1,500 Nm with using dial torque wrench. That equals approx. a 300 kN compression per bolt.

Test Pieces

The test piece used was planned to be rigid as it self and to simulate the rigidity of assembly welds. The tested material was AISI 316 L(N)-IG ITER Grade austenitic stainless steel with original thickness of 60 mm. Test piece consisted of two 400 mm \times 150 mm plates with thickness of 60 mm. Those 60 mm thick halves were machined in order to possess following features when combined together (Fig. 3): Both ends have close square preparation at the length of 60 mm. The joint thickness, which is intended to be filled using multi pass welds, is 20 mm. The length of the welded joint is 250 mm and the joint has a root gap of 1.2 mm.

As can be seen in section A-A and C-C in Fig. 3, the 20 mm thick joint to be welded is captured near to half way at the whole 60 mm thickness of the test piece. A rectangular cavity for a root of the weld is prepared to be 30 mm \times 10 mm. Below the root cavity is a 20 mm thick close square preparation along the whole length of the test piece (400 mm).

After machining of necessary groove geometries, two halves were put together and sealed with using electron beam welding at the sections where close square preparations were prepared, Fig. 4. The aim of above mentioned procedure was to prohibit transverse shrinkage and angular distortions and in that way to produce strains which are correspondent to those which can occur in massive components assembly welding.

Two kinds of 20 mm thick groove geometries were used in hot cracking tests. The groove geometries are shown in Fig. 5. The basic idea was to use wider (Fig. 5a) and narrower (Fig. 5b) groove configurations, in order to get two different multi pass weld shapes together with different depth to width ratios of produced multi pass welds.

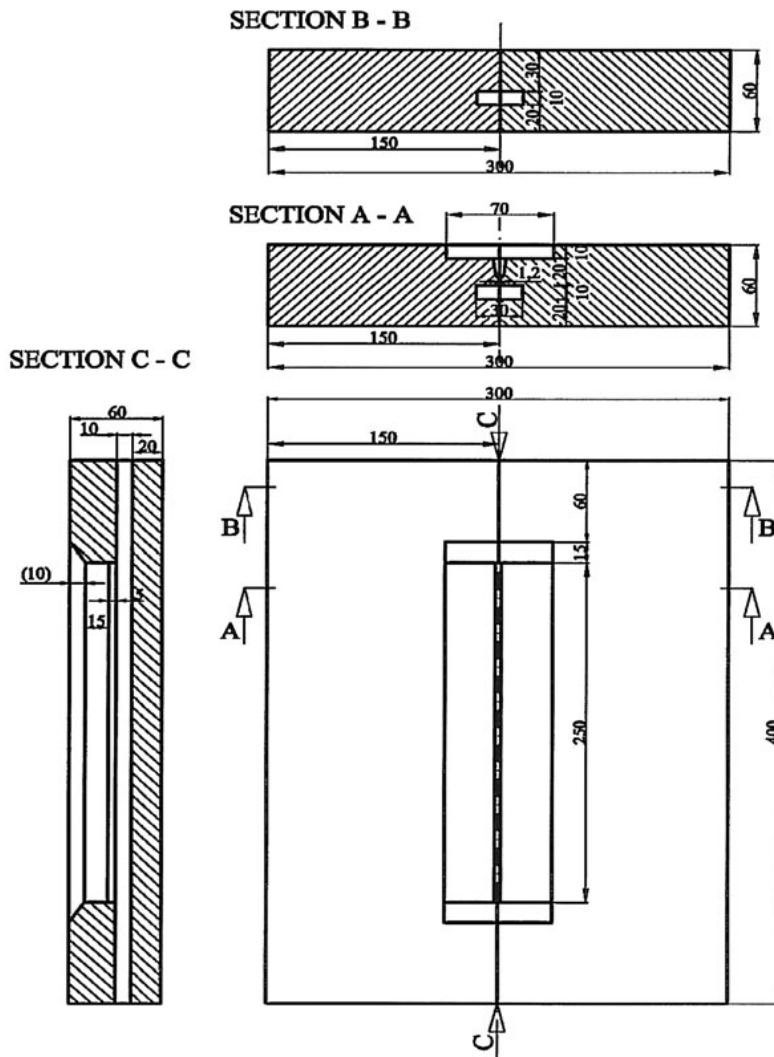


Fig. 3 Test piece used in hot cracking tests

Welding Equipment

Welding experiments were performed by using a combination of Nd:YAG-laser process and MIG-process. The laser used in hybrid process was HAAS-LASER GmbH model HL 3006 D with \varnothing 0.6 mm optical fiber beam delivery system, Fig. 6. The laser has a maximum output power of 3 kW at the surface of a work piece. The full power of 3 kW was used in all experiments. Used lens focusing optic gives a 200 mm focal length, 6.12 degree focusing angle and can provide a spot diameter of 0.6 mm

Fig. 4 Test piece used in hot cracking tests. Two machined halves are put together and sealed using electron beam welding into the one test piece

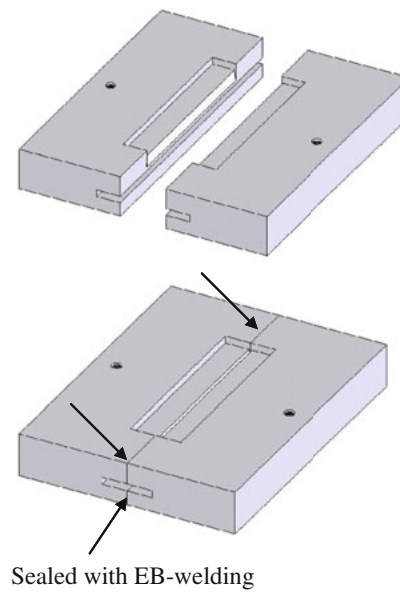
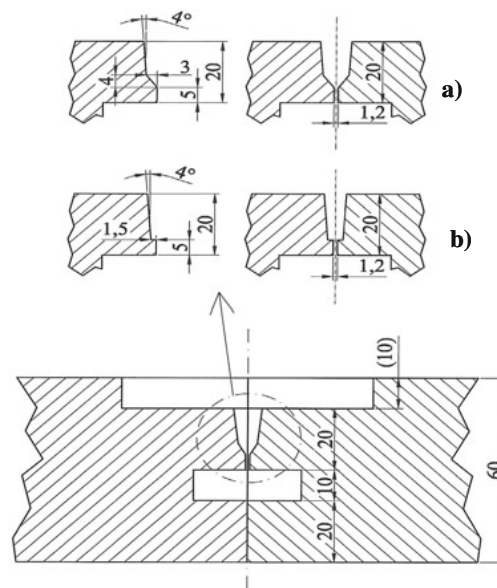


Fig. 5 Two different groove geometries were used in hot cracking tests



in the focal point. The laser system enables a beam parameter product of 25 mm·rad. GMAW machine used in the hybrid welding was KEMPPI Pro 5200 equipped with ProMIG 501 unit, Fig. 7. KUKA KR 15 robot was used in order to execute required welding movements. Self tailored hybrid welding head was mounted in the wrist flange of KUKA-robot, Fig. 7.



Fig. 6 3 kW Nd:YAG-laser used in the experiments



Fig. 7 Welding equipment used in the experiments. *Left:* Kemppi Pro MIG-welding machine, *right:* Hybrid welding head mounted in KUKA KR 15 robot

Hot Cracking Test Program

As described earlier, two different groove configurations were decided to use such a way that three identical test pieces for both groove geometries were prepared. Consequently, we had two test series with three identical hot cracking welding test repetitions in each series. Test pieces with wider groove geometry, Fig. 5a, belonged to the series A and test pieces with narrow groove geometry, Fig. 5b, belonged to

the series B. With using preliminary welding tests proper welding parameters were searched for both groove geometries. Constant welding parameters used in both series are presented in Table 4. As the same parameters in welding of root passes could be used in both series, there were different welding parameters regarding to the welding of filling passes between series A and B, Table 5. That is because filler wire feeding rate, welding speed and focal position needs to be adjusted according to different groove volumes used in test series A and B. Inside the test series, the same parameters were used for welding of each three identical test pieces.

The lay-out of the experimental set-up is shown in Fig. 8.

Before welding experiments, test piece was clamped to the rigid table as described earlier in this study. Welding experiments were executed in such a way that a keyhole mode hybrid welding was first used in welding of root pass (Fig. 9a) and after that a required amount of filling passes (4. . .6 passes) were produced with conduction limited hybrid welding. In conduction limited hybrid method, a power density of an Nd:YAG- laser beam spot was purposely dispersed by using strong defocusing (Fig. 9b). Using the above procedure, the welding process can be brought

Table 4 Constant welding parameters

The constant parameters	
Laser power	3 kW
Focal length	200 mm
Horizontal distance between the laser focal point and filler wire feeding point	2 mm
Diameter of filler wire	1.2 mm
Stick out (electrode extension)	17 mm
Orientation and the angle of arc torch	leading, 55°
Shielding gas (MISON He30= Ar+30%He+0,03NO) and flow rate:	
– Via arc torch's nozzle	20 l/min
– Via extra nozzle	20 l/min

Table 5 Welding parameters of root and filling passes for series A and B

Welding parameters for the root pass		
Filler wire feeding rate	9.5 m/min (28.8 V / 232 A)	
Focal point position	±0 mm (spot size Ø0.6 mm)	
Welding speed	1.3 m/min	
Welding parameters for the filling passes		
	Wider groove geometry, Fig. 6a Series A	Narrow groove geometry, Fig. 6b Series B
Filler wire feeding rate	9.0. . .9.5 m/min (29. . .30 V / 205. . .260 A)	9.0. . .11 m/min (28. . .31 V / 220. . .295 A)
Focal point position	+50 mm (spot size Ø 5.9 mm)	+30. . .+40 mm (spot size Ø 3.8. . .4.9 mm)

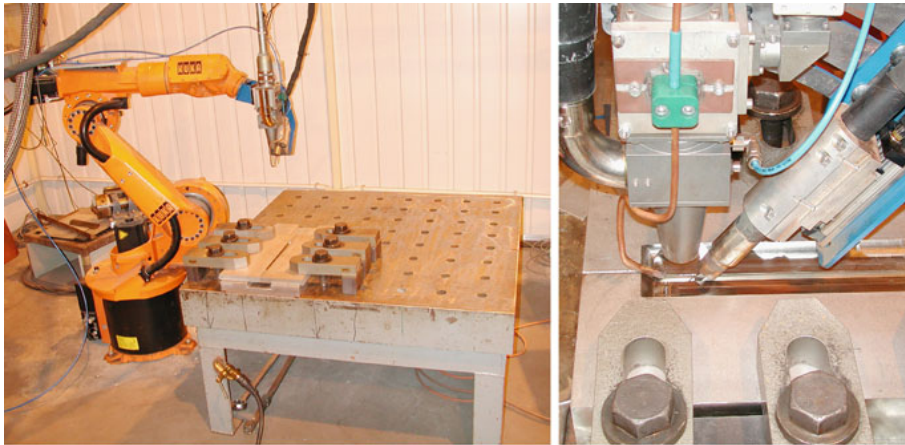


Fig. 8 *Left*: The lay-out of the experimental set-up. *Right*: Close-up from the hybrid welding head configuration

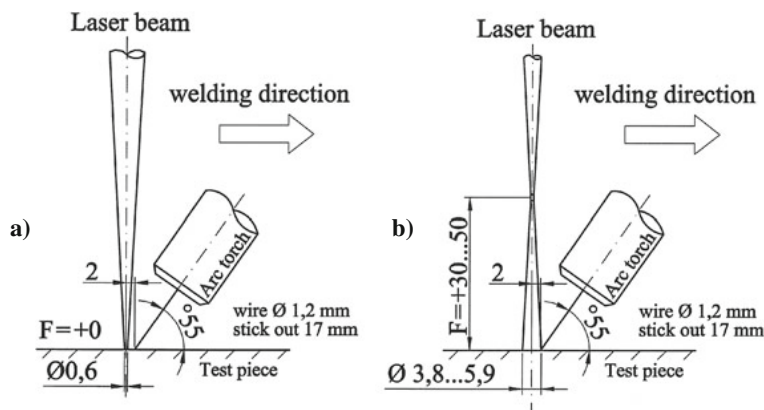


Fig. 9 Set-up used in hybrid welding: (a) key-hole mode in welding of root pass and (b) conduction limited mode in welding of filling passes

inside the conduction limited regime. In addition, a molten filler metal was synergistically added into the laser induced melt pool via a metal inert arc (MIG, Ar + He shielding) welding process. By doing so, a considerable wide melt zones can be produced, which gave a possibility to fill groove gaps which are impossible to fill with using keyhole hybrid welding alone.

After welding, test-pieces were allowed to cool room temperature before clamping was released. Next, test welds were examined by X-ray radiography. After that, test welds were sectioned for macro- and micro graphical preparation. Evaluations of the welds were done by the visual inspection from welded test pieces and from the macro- and micro graphical cross-sections of the welds and from the X-ray radiographs as well.

In order to get reference data from the decreasing groove cross-section and volume, measuring tasks were carefully performed between welding of each pass. Amount of occurred transverse shrinkage was determined measuring the width of welded test piece perpendicular to weld joint using a calibre rule. In addition, the closure of gap opening was separately measured at the surface of the test piece using a calibre rule.

Finally, measurements and macrographs from the test welds together with chemical analysis of base and filler material were combined as the rate of dilution was determined by calculations. In order to get some reference to dilution calculations, electron probe micro analysis (spot size 500 μm and sampling time 30 s) were selectively performed from the weld cross-sections as well.

Results and Discussion

The scope of the study did not include strain measurement during testing. However, results of welding tests showed that the developed test set-up can produce critical conditions to promote hot cracking in produced test welds.

Observations of Hot Cracking Tendency

Multi pass technique was used in hot cracking welding tests. In test welds of series A (wider groove), a total of 5 passes were needed to fill the groove, whereas in test series B (narrow groove), 7 passes were needed. During the welding experiments, great attention was paid to the visual inspection of the surface of the intermediate passes. The surface of each individual pass was visually inspected before the welding of consequent pass started. The observations from the visual inspections clearly showed that hot cracking, which opened to the surface of the weld pass, did occur. Hot cracking observations concerning individual passes in both series are summarized in Tables 6 and 7.

In test series A, hot cracking occurred only in one test piece of all three: in welding of the first filling pass of multi pass weld H3. In test series B, hot cracking occurred in every test piece. In those test pieces, hot cracking was occurred in

Table 6 Hot cracking observations after completion of individual passes: test series A

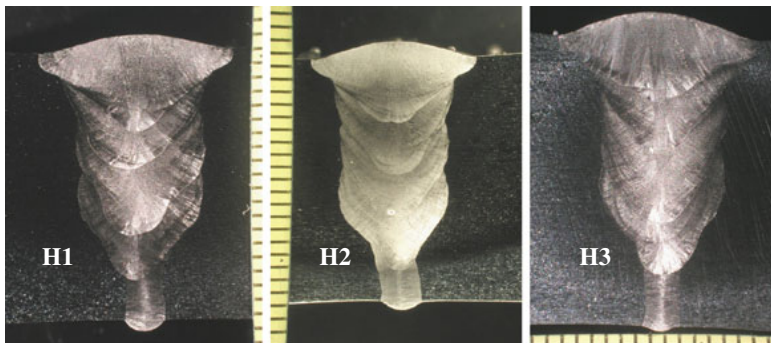
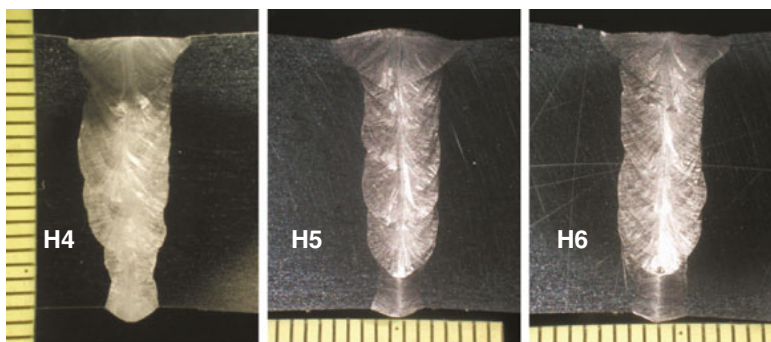
Test series A	Occurrence of hot cracking		
	Weld H1	Weld H2	Weld H3
Root pass	No	No	No
1st filling pass	No	No	Yes
2nd filling pass	No	No	No
3rd filling pass	No	No	No
4th filling pass	No	No	No

Table 7 Hot cracking observations after completion of individual passes: test series B

Test series B	Occurrence of hot cracking		
	Weld H4	Weld H5	Weld H6
Root pass	No	No	No
1st filling pass	No	<i>Yes</i>	<i>Yes</i>
2nd filling pass	<i>Yes</i>	<i>Yes</i>	<i>Yes</i>
3rd filling pass	<i>Yes</i>	<i>Yes</i>	No
4th filling pass	No	No	No
5th filling pass	No	No	No
6th filling pass	No	No	No

the first, second and third filling passes, whereas in root passes no cracking was observed to occur. It was also found that all cracking occurred in welds which were situated 2/3 of plate thickness from the bottom.

It turned out when completed weld cross-sections were observed that cracks found earlier from the surface of the individual passes seemed to be “healed” by

**Fig. 10** Welds from the test series A: Weld H1, Weld H2 and Weld H3**Fig. 11** Welds from the test series B: Weld H4, Weld H5 and Weld H6

re-melting of following overlapping passes. This can be noticed from the macrographs of the weld cross-sections of test series A (weld H1, H2 and H3) and test series B (weld H4, H5 and H6) which are presented in Figs. 10 and 11, respectively.

Effect of Weld Bead Geometry

In both test series A and B, cross-sectional weld bead geometries were measured from the macrographs, especially depth and width of each individual pass (Tables 8 and 9). In addition, depth to width ratios was calculated and those ratio-values were compared to hot cracking tendency.

According to results, narrow groove configuration used in series B tended to cause more hot cracking than wider groove configuration used in series A. However, in root passes hot cracking was not emerged, although they had a large depth to width ratios ($D/W \sim 1.29 \dots 3.04$). In general, depth to width ratio (D/W) of 1 seems to be often a near threshold value concerning the occurrence of hot cracking in filling passes. In multi pass welds H1 and H2, where depth to width ratios of filling passes stayed between 0.5 . . . 0.84, no cracking was observed.

Table 8 Cross-sectional weld bead geometry (depth/width) in test series A

Test series A			
Weld H1	D (mm)	W (mm)	D/W
Root pass	6.4	2.7	2.37
1st filling pass	7.3	8.8	0.83
2nd filling pass	7.6	9.1	0.84
3rd filling pass	6.5	10.5	0.62
4th filling pass	7.0	10.5	0.67
Weld H2	D (mm)	W (mm)	D/W
Root pass	5.8	3.2	1.81
1st filling pass	7.0	8.5	0.82
2nd filling pass	6.3	8.5	0.74
3rd filling pass	6.5	9.5	0.68
4th filling pass	6.5	13.0	0.50
Weld H3	D (mm)	W (mm)	D/W
Root pass	7.0	3.3	3.04
1st filling pass	8.0	8.3	0.96
2nd filling pass	7.5	8.0	0.94
3rd filling pass	6.9	9.5	0.73
4th filling pass	5.8	12.9	0.45

Note: grey color donates occurred hot cracking

Table 9 Cross-sectional weld bead geometry (D = Depth/W = Width) in test series B

Test series B			
Weld H4	D (mm)	W (mm)	D/W
Root pass	5.0	3.6	1.39
1st filling pass	5.4	5.6	0.96
2nd filling pass	4.5	6.3	0.71
3rd filling pass	4.8	6.6	0.73
4th filling pass	4.5	6.3	0.71
5th filling pass	4.6	5.9	0.78
6th filling pass	5.6	8.8	0.64
Weld H5	D (mm)	W (mm)	D/W
Root pass	5.5	3.2	1.72
1st filling pass	6.0	5.1	1.18
2nd filling pass	5.5	5.1	1.08
3rd filling pass	5.8	5.5	1.05
4th filling pass	5.9	5.5	1.07
5th filling pass	5.5	5.9	0.93
6th filling pass	5.5	9.1	0.60
Weld H6	D (mm)	W (mm)	D/W
Root pass	5.7	4.0	1.43
1st filling pass	5.1	5.6	0.91
2nd filling pass	5.8	5.4	1.07
3rd filling pass	5.5	5.1	1.08
4th filling pass	4.3	5.4	0.80
5th filling pass	3.8	5.4	0.70
6th filling pass	4.2	8.3	0.51

Note: grey color denotes occurred hot cracking

Weld Microstructure and Appearance of Hot Cracking

As mentioned earlier, visual evaluation after welding of each filling pass revealed that hot cracks occurred centered at along the weld length and opened to the surface of the weld. In Fig. 12a, it is shown an example from the test series B, where the part of the joint was purposely left without upper filling passes in order to authenticate the presence of hot cracking in that case occurring in the first filling pass. In Fig. 12b, it is shown the top view from the Fig. 12a, which reveals hot cracking opened to the surface of the first filling pass.

From the micro graphs presented in Fig. 13, it can be seen magnifications (450 \times) taken from the same cross-section as shown in Fig. 13a. Micro graphs show the upper and lower part of the hot crack propagated in the fully austenitic microstructure.

It seems that during the multi pass welding of this study, the following filling pass has been overlapped into the previous pass such much that molten metal has “healed” the hot crack underneath. Evaluations from the X-ray radiography and the

Fig. 12 (a) Macro cross-section showing hot cracking propagated into the surface of the first filling pass (magnification $4\times$). (b) The top view from the Fig. 12a showing hot cracking along the weld length (magnification $5,3\times$)

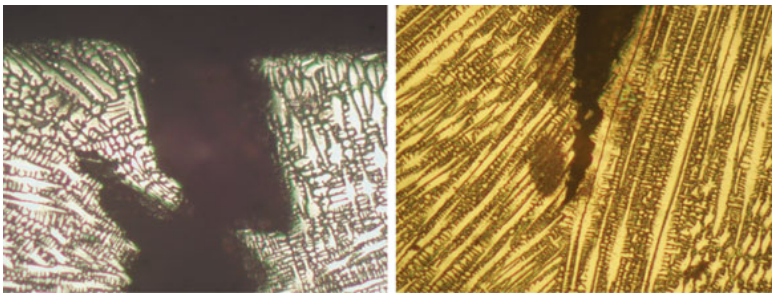
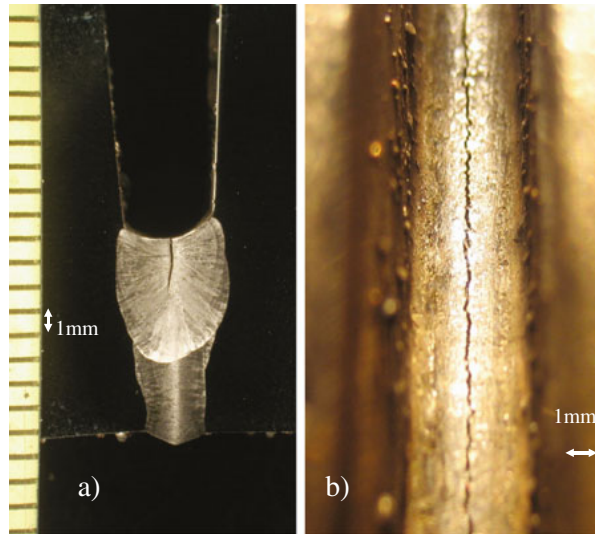


Fig. 13 Micro graphs taken from the same cross-section as shown in Fig. 12a. Micro graphs show the upper (graph on the left) and lower part (graph on the right) of the hot crack in the fully austenitic microstructure. Magnification $450\times$

cross-sectional macro graphs (Figs. 10 and 11) of the welds support “healing” observation. Anyhow, in general this healing- effect will not be always 100% certain, which must have taken into considerations in production welds of real applications.

Weld which is a product of primary austenite solidification mode has very distinctive microstructural morphology when viewed metallo-graphically. Above mentioned are e.g. cited in references 19–21. Based on metallographic examination primary austenite solidification can be defined in all test welds of series A (welds: H1, H2 and H3) and B (welds: H4, H5 and H6). There is couple of micro graph example shown from the both series A and B. In Fig. 14a, b it is shown weld metal structures from the intermediate passes of test weld H3 and H4, respectively. Both weld metals have solidified in primary austenite solidification mode. Fully austenitic microstructure of weld metal is presented in Fig. 14a, b.

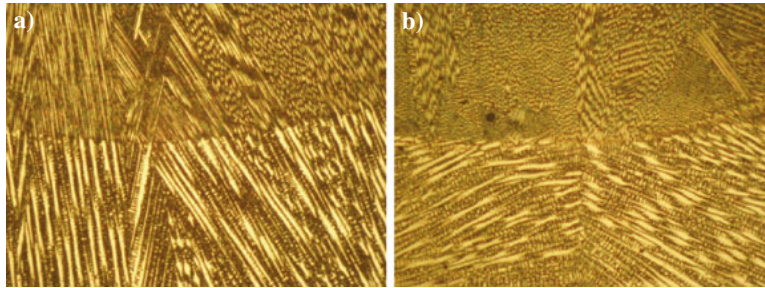


Fig. 14 Micro graphs showing fully austenitic microstructure of weld metal in (a) test weld H3 and (b) H4. Both weld metals have solidified in primary austenite solidification mode. Magnification 230 \times

Assessment of Rate of Dilution

From the both test series one test weld was selected for the assessment of rate of dilution: Multi pass weld H1 from the test series A and multi pass weld H5 from the test series B. In order to assess the rate of dilution, following procedure was used: Cross-sectional macrographs of weld H1 and H5 are digitally exported to CAD-software and further converted into CAD-image. The borderlines of groove geometries with known reduction adjustments which are due to transverse shrinkage were super positioned with the weld cross-section into the same image. By using CAD-software's image processing capabilities, individual proportions of each weld pass, melted base- and filler material in terms of cross-sectional area were determined. Finally, rate of dilution in each pass was calculated with using proportions of determined cross-sectional area together with the chemical element's proportions taken from the specifications which show the exact chemical compositions of the base and filler material (Table 2). Since dilution rates were known, chromium and nickel equivalent values were additionally calculated using equations presented in Table 3. Summary of both the rate of dilution and chromium and nickel equivalent calculations (Hammar & Svensson) for the multi pass welds H5 and H1 are presented in Tables 10 and 11.

Dilution in root pass of weld H1 and H5 was determined by calculations to be 63% and 60%, respectively. What comes to filling passes, dilution rates concerning base material are in weld H1 between 6 and 31% (average value 16%) and in weld H5 between 8 and 17.5% (average value 13.25%). Results reveal that each filling pass was some extent diluted by previous passes which naturally contain proportion of elements from the base material. Larger dilutions in root pass results from the narrow square preparation (width ~1 mm) in root face, as groove volume remains very low and much of filler material is not needed.

In order to get some reference to dilution calculations, electron probe micro analysis (EPMA) were performed from the weld cross-sections of welds H1 and H5. EPMA measurements give information about desired element content in weight-%. Electron probe micro analyses were carried out with using a spot size of 500 μm

Table 10 The results of dilution- and Cr/Ni-equivalent calculations concerning multi pass weld H5

Multi pass weld: H5 Pass no.	Proportions of dilution (%)			Hammar & Svensson equivalents		
	Base mat.	Filler mat.	Previous pass	Cr-eq	Ni-eq	Cr/Ni-eq
Root pass ^a	60	40	–	22.48	16.77	1.34
1st filling pass ^b	16.5	44.5	39 ^a	23.30	17.99	1.30
2nd filling pass ^c	13.5	51	35.5 ^b	23.78	18.75	1.27
3rd filling pass ^d	8	41	51 ^c	23.97	19.08	1.26
4th filling pass ^e	11	44	37 ^d + 8 ^c	23.99	19.13	1.25
5th filling pass ^f	17.5	54.3	28.2 ^e	23.92	18.99	1.26
6th filling pass	13	47.9	39.1 ^f	23.97	19.06	1.26

For example: 4th filling pass = base material 11% + Filler material 44% + 3rd filling pass 37% + 2nd filling pass 8% = 100%

Table 11 The results of dilution- and Cr/Ni-equivalent calculations concerning multi pass weld H1

Multi pass weld: H1 Pass no.	Proportions of dilution (%)			Hammar & Svensson equivalents		
	Base mat.	Filler mat.	Previous pass	Cr-eq	Ni-eq	Cr/Ni-eq
Root pass ^a	63	37	–	22.41	16.58	1.35
1st filling pass ^b	31	49	20 ^a	23.27	17.77	1.31
2nd filling pass ^c	12	46	41 ^b + 1 ^a	23.68	18.58	1.28
3rd filling pass ^d	15	47	38 ^c	23.83	18.81	1.27
4th filling pass	6	47	45 ^d + 2 ^c	24.07	19.29	1.25

and sampling time of 30 s. Each pass in both H1 and H5 test weld was analyzed and further two measurements were made for the base material as well. The points of locations of analyses are shown in Figs. 15 and 16.

When justifying the confidence of EPMA measurements, following comparison was made: The chemical analysis data of the base material AISI 316L(N)-IG

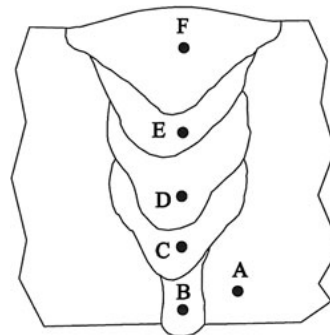
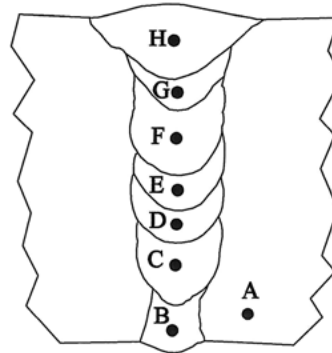
**Fig. 15** The points (A...F) showing locations where electron probe micro analyses (EPMA) were taken in multi pass weld H1

Fig. 16 The points (A . . . H) showing locations where electron probe micro analyses (EPMA) were taken in multi pass weld H5



according to EN 10204-3.1 (Table 2) was considered as a reference data and that data was compared to data collected from the base material with separate electron probe micro analyses (EPMA). EPMA data differed from the given reference data (EN 10204-3.1) on the range of approx. 2.5–11% depending on the reviewed element. That could be considered as a reasonable matching accuracy between those two independent measurements.

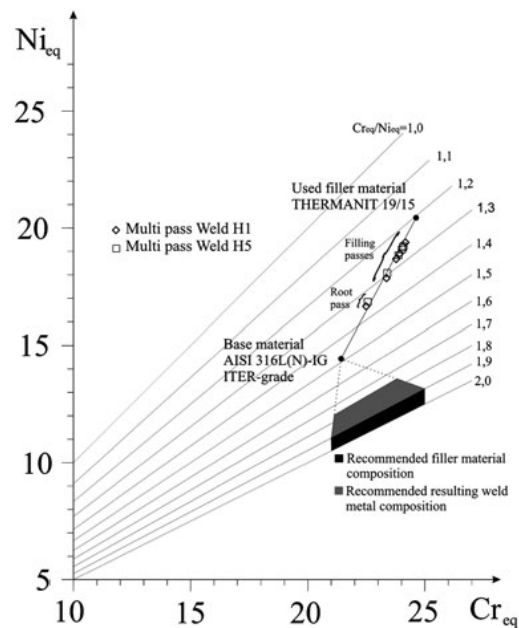
On the other hand, also the results of electron probe micro analysis seemed to be quite consistent when compared to ones which were achieved by using dilution calculations. This confirmed that used procedure for the assessment of rate of dilution can be successfully used. The results including cracking observations and dilution calculations are in good agreement with the initial data, as it is known that both parent material and filler wire used, are fully austenitic. The fact that in test weld H1 and H2 filling passes did not cracked although chromium/nickel-equivalent ratios were at the same level as H4-H6 could have been related to weld cross-sectional geometry. Filling passes in weld H1 and H2 are much wider than the filling passes which were cracked in welds H4-H6 (Tables 8 and 9). When considering test weld H3, it had cracking in the first filling pass, which had the highest depth to width ratio (0.96) of all H3 filling passes, Table 8. Narrower filling passes with large depth to width ratio tended to be more susceptible to hot cracking than the wider ones.

Effect of Weld Metal Composition

In order to speculate what kind of filler material selection could help to prevent weld solidification cracking in the studied case, Cr/Ni-equivalent diagram can be used as a suggestive tool, Fig. 17. In the Fig. 17, the data from the results of dilution- and Cr/Ni-equivalent calculations concerning multi pass weld H1 and H5 are converted to Hammar & Svensson diagram.

As it can be seen from the Fig. 17, in the case of filling passes dilution corresponds to Cr_{eq}/Ni_{eq} -ratio values of 1.25 . . . 1.31 in weld metal, whereas in root pass

Fig. 17 Cr/Ni-values for filling passes and root pass of multi pass weld H1 and H5 are marked in Hammar & Svensson diagram. Grey and darkened area shows boundaries for recommended filler material and weld metal composition, respectively



dilution was higher leading to value of 1.35. That is way below compared to risk value of 1.5. In that respect, hot cracks in test welds approved that risk according to Cr_{eq}/Ni_{eq} -calculations is for real.

It should be noticed that the used parent material had quite low impurity content. According to the certificate (see Table 2) phosphorous (P) + sulphurous (S) content was $0.021 + 0.0001 = 0.0211$ wt-% whereas the nominal composition spec (see Table 1) allows the total of P + S content of 0.035 wt-% as a maximum. As the results showed that cracking could occur at quite low impurity content ($P+S=0,0211$ wt%), therefore it could be danger that hot cracking susceptibility strongly enhances if the used ITER-grade heat will hold the maximum amount of impurity content allowed by the nominal composition spec, Table 1.

Selection of Filler Metal to Decrease Cracking Risk

One possibility to overcome cracking risk is a correct filler material choice. In the case of this study, that is to use more ferritic filler wire material, which will have e.g. a value of Cr_{eq}/Ni_{eq} -ratio about 1.9...2.0 (see Fig. 17). Using this kind of filler wire and assuming dilution shown in Tables 10 and 11, Cr_{eq}/Ni_{eq} -ratio about 1.75–1.90 and primary ferrite solidification could be achieved in weld metal. However, the welded application itself does not necessarily allow 5–15% room temperature delta ferrite content in weld metal, because of certain requirements or restrictions.

In the case of this study initial requirement was that microstructure of weld metal in joints must be fully austenitic, containing as less as possible delta ferrite at room temperature. It was not fully clear by end-user's side, is ferrite content allowed in assembly welds of ITER-applications and furthermore if ferrite is allowed, what is the maximum allowed content in percent? Thus, it is important to clearly specify the maximum allowed weld ferrite content. If primary ferrite solidification could be achieved in produced weld, weld hot cracking susceptibility would be remarkably reduced compared to situation where a weld is solidified as primary austenitic mode.

Conclusions

In this study the main objective was to find a method for studying hot cracking susceptibility when a thick section austenitic stainless steel is welded using laser hybrid welding process (3 kW Nd:YAG-laser + GMAW) and multi pass technique. The tested parent material was a specially customized heat: AISI 316L(N)-IG ITER-grade austenitic stainless steel. During this study the test system was first developed and tested. It consisted of a very rigid clamping system and specially designed 60 mm thick test piece which was planned to be rigid as itself.

Although the test set-up did not include strain measurement during testing, results of welding tests showed that the developed test set-up can produce critical conditions to promote hot cracking in produced AISI 316L(N)-IG ITER grade test welds in multi pass laser-arc hybrid welding. Results showed that in this case the used combination of the parent/filler material was led to primary austenitic solidification and fully austenitic weld metal microstructure. It was advisable to carry on welding tests with using filler wire composition which may give primary ferrite solidification on weld metal and thus leading to diminishing hot cracking susceptibility. Results also confirmed that hot cracking susceptibility of welded base and filler material combination can be suggestively pre-estimated by applying known weld metal composition and chromium (Cr_{eq}) and nickel (Ni_{eq}) equivalents.

Within the test series, weld passes did not always have same cracking susceptibility although they possessed the same range of Cr/Ni-equivalent values. This can be associated to cross-sectional geometry of individual weld pass. Narrower filling passes with large depth to width ratio tended to be more susceptible to hot cracking than the wider ones. Above could be found in test series B, where weld passes were more susceptible to hot cracking than the passes in series A.

As the scope of this study did not include strain measurement during testing, it has been considered to execute further studies with set-up which include strain measuring at the near weld zone during the welding.

Acknowledgements The authors wish to thank VTT- the Technical Research Centre of Finland, the National Technology Agency of Finland and the European Fusion Development Agreement for funding the project within the experiments of this paper was executed. We like to thank also Mr. Mikko Pesari for his assistance in welding experiments and illustration work for figures.

References

1. Karhu M, Jokinen T and Kujanpää V (2006) Conduction Limited Laser-Arc Hybrid Welding of Austenitic Stainless Steel with Different Joint Geometries, VTT Research report No. TUO25-056299, Espoo, Finland, 25p.
2. Folkhard E (1988) *Welding Metallurgy of Stainless Steels*. Springer, 279p.
3. Papeleux P, Flipot AJ and Lafontaine I (1973) *Welding Austenitic Steel Clads for Fast Reactor Fuel Pins*, International Atomic Energy Agency, Document AIEA/SM-173/VII-47, pp. 1–17.
4. Borland JC and Younger RN (1960, January) Some Aspects of Cracking in Welded Cr-Ni Steels. *British Welding Journal*:22–59.
5. Sorokin LI (2004) Evaluation of crack formation resistance in welding and heat treatment of creep resisting nickel alloys. *Welding International* 18(5):379–385.
6. Barabash V Material Specification for the supply of 316L(N)-IG austenitic stainless steel plates, G 74 SP 12 03-07-09 W 0.1, Rev.2- 08.07.2003.
7. Schaeffler AL (1949) Constitution Diagram for Stainless Steel Weld Metal. *Met. Progr.* 56: 680 and 680B.
8. DeLong WT, Ostrom GA and Szumachowski ER (1956) Measurement and Calculation of Ferrite in Stainless Steel Weld Metal. *Welding Journal* 35:521s–528s.
9. Hull FC (1973) Delta Ferrite and Martensite Formation in Stainless Steels. *Welding Journal* 52:193s–203s.
10. Hammar Ö and Svensson U (1979) *Solidification and casting of metals*. The Metals Society, London, pp. 401–410.
11. Kotecki DJ and Siewert DTA (1992) WRC-92 constitution diagram for stainless steel weld metals: a modification of the WRC-1988 diagram. *Welding Journal* 71(5):171s–178s.
12. Kujanpää V, Suutala N, Takalo T and Moisio T (1979) Correlation between solidification cracking and microstructure in austenitic and austenitic-ferritic stainless steel weld. *Welding Research International* 9(2):55–76.
13. Lippold JC (1985) Centerline Cracking in Deep Penetration Electron Beam Welds in Type 304L Stainless Steel. *Welding Journal* 64(5):127s–136s.
14. David SA, Vitek JM and Hebble TL (1987) Effect of Rapid Solidification on Stainless Steel Weld Metal Microstructures and Its Implications on the Schaeffler Diagram. *Welding Journal* 66(10):289s–300s.
15. Lippold JC (1994) Solidification behaviour and cracking susceptibility of pulsed-laser welds in austenitic stainless steels. *Welding Journal* 73(6):129s–139s.
16. Lippold JC (1995) *Microstructure Evolution in Austenitic Stainless Steel Laser Welds*, Proceedings of the Second International Conference on Beam Processing of Advanced Materials, Cleveland, Ohio, USA, pp. 167–178.
17. Lienert TJ (1998) A Combined PSM/Weldability Diagram for Laser Welded Austenitic Stainless Steel, Trends in Welding Research, Proceedings of the 5th International Conference, Pine Mountain, Georgia, USA, pp. 724–728.
18. Lienert TJ and Lippold JC (2003) Improved weldability diagram for pulsed laser welded austenitic stainless steels. *Science and Technology of Welding and Joining* 8(1):1–9.
19. Suutala N (1982) *Solidification Studies on Austenitic Stainless Steels*, Doctoral thesis, University of Oulu, Finland.
20. Elmer JW, Allen SM and Eagar TW (1989, October) Microstructural Development during Solidification of Stainless Steel Alloys. *Metallurgical Transactions A* 20A:2117–2131.
21. Lippold JC and Kotecki DJ (2005) *Welding Metallurgy and Weldability of Stainless Steels*. Wiley, 357p.

Publication II

Karhu, M., and Kujanpää, V.

Defocusing techniques for multi-pass laser welding of austenitic stainless steel

Reprinted with permission from

Physics Procedia

Vol. 78, pp. 53-64, 2015

© 2015, Elsevier



Available online at www.sciencedirect.com

ScienceDirect

Physics Procedia 78 (2015) 53 – 64

Physics

Procedia

15th Nordic Laser Materials Processing Conference, Nolamp 15, 25-27 August 2015,
Lappeenranta, Finland

Defocusing techniques for multi-pass laser welding of austenitic stainless steel

Miikka Karhu^{a*}, Veli Kujanpää^b

^aFormerly with VTT Technical Research Centre of Finland Ltd, currently with Lappeenranta University of Technology, Skinnarilankatu 34, Lappeenranta, FI-53850, Finland

^bTechnical Research Centre of Finland Ltd, Skinnarilankatu 34, Lappeenranta, FI-53850, Finland

Abstract

This study introduces an experimental work carried out in multi-pass laser welding with cold filler wire and laser-arc hybrid welding of thick section austenitic stainless steel. As it has been demonstrated earlier, hybrid and cold wire welding with a keyhole-mode can offer very efficient way to produce multi-pass welds in narrow gap thick section joints. However, when multi-pass welding is applied to one pass per layer method without e.g. scanning or defocusing, the used groove width needs to be very narrow in order to ensure the proper melting of groove side walls and thus to avoid lack of fusion/cold-run defects. As a consequence of the narrow groove, particularly in thick section joints, the accessibility of an arc torch or a wire nozzle into the very bottom of a groove in root pass welding can be considerably restricted. In an alternative approach described in this paper, a power density of a laser beam spot was purposely dispersed by using a defocusing technique. In groove filling experiments, a power density of defocused laser beam was kept in the range, which led the welding process towards to conduction limited regime and thus enabled to achieve broader weld cross-sections. The object was to study the feasibility of defocusing as a way to fill and bridge wider groove geometries than what can be welded with focused keyhole-mode welding with filler addition. The paper covers the results of multi-pass welding of up to 60 mm thick joints with single side preparations.

© 2015 The Authors. Published by Elsevier B.V. This is an open access article under the CC BY-NC-ND license (<http://creativecommons.org/licenses/by-nc-nd/4.0/>).

Peer-review under responsibility of the Lappeenranta University of Technology (LUT)

Keywords: laser welding; defocusing; multi-pass; austenitic stainless steel

* Corresponding author. Tel.: +358-50-447-7916
E-mail address: miikka.karhu@lut.fi

1. Introduction

Laser welding is generally considered as a high energy density welding process, in which an ability to use a keyhole welding is exploited. In order to bring e.g. a steel alloy locally in the vapour phase for keyhole welding, the power density of laser beam at the surface of the work piece must be risen to the magnitude of 10^6 W/cm² or greater. This keyhole laser welding mode is also normally applied in hybrid or cold wire welding process, which results to a narrow, pinhead looking weld bead, where typical keyhole weld features like high depth/width ratio can be detected. It has been demonstrated in the previous studies of e.g. Arata et al. (1986), Jokinen et al. (2003), Rethmeier et al. (2009), Phaoniam et al. (2013) and Zhang (2013), that hybrid or cold/hot wire welding with keyhole mode can offer a very efficient way to produce multi-pass welds in very narrow gap thick section joints. In the alternative approach described in this paper, the used groove configurations (especially width of the groove gaps) were resembled like those used in conventional narrow gap arc welding processes (e.g. NG-TIG). One driving force for testing wider groove geometries was targeting to improve especially the accessibility and clearance of an arc torch or a wire nozzle in the case of root pass and lower passes welding of thick joints (~ 60mm). When the successful groove filling in above mentioned groove configurations is aimed, a keyhole mode welding alone cannot be used in filling runs, because gap widths are too wide to be bridged. Under the circumstances, a laser part (in terms of power density of the beam at the work piece) as well as filler wire feeding rate and welding speed has to be tuned in hybrid or cold wire process such that much wider weld beads can be produced. Therefore, it was decided to disperse a power density of a laser beam spot purposely by using defocusing and in that way bring the welding process towards or inside the conduction limited regime.

Nomenclature

NG-TIG	narrow gap – tungsten inert gas
P_L	laser power
F	focal point position
v_w	welding speed
v_f	filler wire feeding speed
MIG	metal inert gas
LF	lack of fusion

2. Experimental

2.1. Materials and test specimens

Base materials used in the experiments were austenitic stainless steel alloys with the different plate thickness between 10mm and 60mm as follows: AlloyX, PL=10mm, AISI 316L-A, PL=20mm, AISI316L-B, PL=60mm. Test specimens for the welding tests were rectangular pieces of 150 mm in width and 300 mm in length. Required groove geometries were made using machining and joints are prepared with tack welds in both ends and at the middle in order to achieve demanded joint configuration. Filler materials used were diam. Ø 1.0 mm ESAB OK Autrod 316LSi and diam. Ø 0.8 mm ESAB OK Autrod 308LSi stainless steel filler wires. The exact chemical compositions of the base and filler materials are given in Table 1.

Table 1. Chemical compositions of the used base and filler materials.

Element weight-%	C	Si	Mn	P	S	Cr	Ni	Mo	N	Cu	Ti+Ta
Alloy X	0.026	0.30	1.49	0.030	0.001	22.0	5.8	3.09	-	0.16	< 0.01
AISI 316L-A	0.024	0.37	1.70	0.020	0.0002	17.6	12.3	2.43	0.07	0.01	< 0.01
AISI 316L-B	0.025	0.36	1.70	0.021	0.0001	17.6	12.2	2.41	0.07	0.01	< 0.01
Autrod 316LSi	0.020	0.80	1.80	0.018	0.011	18.4	12.2	2.50	0.06	0.09	-
Autrod 308LSi	0.020	0.90	1.00	0.020	0.010	19.7	10.7	0.04	-	0.03	-

2.2. Welding equipment

Welding experiments were performed by using a combination of Nd:YAG laser and GMAW/cold wire-process. The laser used in trials was HAAS-LASER GmbH model HL 3006 D with \varnothing 0.6 mm optical fiber beam delivery system. The laser has a maximum output power of 3 kW at the surface of a work piece. The full power of 3 kW was used in all experiments. Used lens focusing optic gives a 200 mm focal length, 6.12 degree focusing angle and can provide a spot diameter of 0.6 mm in the focal point. The laser system enables a beam parameter product of 25 mm²mrad. GMAW machine used in the hybrid and cold wire purpose was KEMPPi Pro 5200 equipped with PromIG 501 unit. KUKA KR 15 robot was used in order to execute required welding movements. Self-tailored hybrid welding head was mounted in the wrist flange of KUKA-robot, Figure 1.

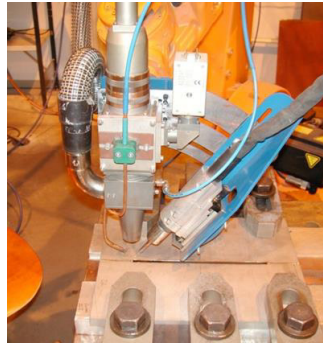


Fig. 1. Welding set-up showing general arrangement used in the welding experiment.

2.3. Experimental procedure

In order to get basic knowledge how different set of defocusing values affect the cross-section of the produced weld bead, welding experiments were started with preliminary bead-on-plate defocusing tests. This gave a suggestive guideline which was then applied in the further welding experiments, where gap filling of different groove widths was studied.

Groove gap filling experiments were executed in such a way that austenitic stainless steel test pieces with different plate thickness (10-60 mm) and groove gap openings were welded in the flat position and with utilizing laser-arc hybrid welding and also partly laser welding with cold filler wire. Evaluations of test welds were made using visual inspection and a light microscopy as well. Selected test welds were cut transversally into the specimens for metallographic preparation. During the preparation, the specimens were ground, polished and electrolytically etched (10% aqueous oxalic acid, 30V/2A/40s) in order to reveal macro- and microscopic weld cross-sectional appearances.

3. Results and discussion

3.1. Bead-on-plate defocusing tests

Bead-on-plate experiments give informative guideline how the use of different beam defocusing values affect the mode of heat transfer (keyhole vs. conduction limited) into work piece and the shape of emerging weld cross-section. This knowledge is applied to further gap filling experiments in the later chapter.

The series of bead-on-plate melt runs were carried out using a 3 kW Nd:YAG laser power, a 200 mm focal optic and different focal position adjustments. Only the use of positive ($F=0\dots+60$) defocusing values which were set above the surface of the test piece were considered because the 200 mm focal length was used and it was decided that it will be better not to bring welding optic too close to the surface of the test piece and weld pool which would be the case if negative defocusing values would be used. In this particular case, above procedure enables multi-pass filling also near to root portion of up to 60 mm thick joint and get a welding optic further off from occasional spatters coming from the weld pool zone.

Figure 2 shows the macro cross-sections from the bead-on-plate defocusing trials where series of melt runs were autogenously laser welded in 10 mm thick AlloyX austenitic stainless steel plates using 3 kW laser power at the welding speed of 0.4 m/min, argon shielding gas and seven different ($F=0\dots+60$) focal position adjustments.

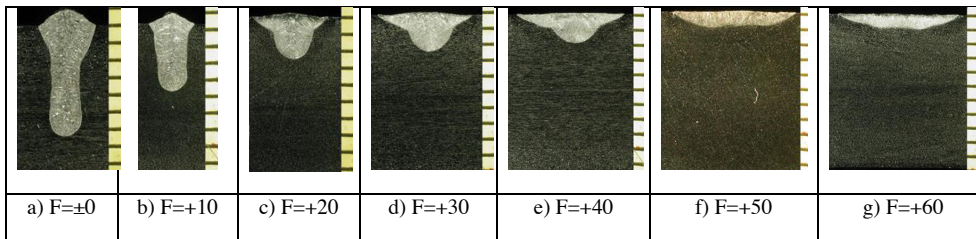


Fig. 2. Cross sections of bead on plate melt runs in austenitic stainless steel, autogenously welded with Nd:YAG laser and different focal positions. Laser power: 3 kW and welding speed: 0.4 m/min.

For a plain comparison purposes, the size of beam spot in diameter was assessed by using data geometry of beam measurement. Moreover, theoretical power densities for different focal position adjustments were estimated with simplified manner where e.g. reflections, scattering and attenuation etc. was omitted. The recap of above-mentioned contemplation is presented in Table 2.

Table 2. Diameters of laser beam spot and theoretical power densities at different focal positions using a 200 mm focal length optic and a 3 kW laser power.

Melt run	Focal position [mm]	Diameter of beam spot (note 1) [mm]	Power density (note 2) [W/cm^2]
a)	± 0	$\varnothing 0.6$	$\sim 1.06 \times 10^6$
b)	+ 10	$\sim \varnothing 1.7$	$\sim 1.32 \times 10^5$
c)	+ 20	$\sim \varnothing 2.7$	$\sim 5.24 \times 10^4$
d)	+ 30	$\sim \varnothing 3.8$	$\sim 2.65 \times 10^4$
e)	+ 40	$\sim \varnothing 4.9$	$\sim 1.59 \times 10^4$
f)	+ 50	$\sim \varnothing 5.9$	$\sim 1.10 \times 10^4$
g)	+ 60	$\sim \varnothing 7.0$	$\sim 0.78 \times 10^4$

Note 1: In case of a) $\varnothing 0.6$ mm spot diameter is the measured value of a focus monitor. Diameter values from b) to g) are calculated, approx. values.

Note 2: Calculated with simplified manner, using a theoretical laser power value of 3 kW (reflections, scattering and attenuation is omitted).

As the shapes of the weld cross-sections in Figure 2 and the scale of power densities with different focal adjustment given in Table 2 are being evaluated, it can be noticed that in the cases of a) and b) power density of laser beam at the work piece has been high enough to produce a keyhole-mode. That is corresponding with the theoretical power density values of $1.06 \times 10^6 \text{ W/cm}^2$ and $1.32 \times 10^5 \text{ W/cm}^2$, which are listed in Table 2. Onwards the cross-section c), where focal positions of +20 mm and greater are used, the welding process is starting to turn from keyhole-mode into the conduction limited mode, while power density is decreasing at the level, where vaporization of material is not sufficient enough to sustain or even produce keyhole vapour channel. Above mentioned can be detected from the cross-sectional features starting from the melt run c) and continuing towards the melt run g), as the penetration becomes shallower and depth/width ratio decreases. As for examples, the depth/width (d/w) ratio of weld cross-section produced using F=0 focusing in case a) is determined to be $d/w \sim 4$, whereas in the case c) and f) which were strongly defocused (F=+20...+50), d/w is ~ 1 and ~ 0.1 , respectively. This tendency of cross sectional weld features is in well accordance with the assessment of theoretical power densities which are calculated to be at the magnitude of 10^6 W/cm^2 in the case a) and 10^4 W/cm^2 in the cases from c) to g), Table 2. In Figure 2e) and onwards, the features of weld cross-sections are pronounced looked like produced by conduction limited mode as a protruding peak which can be barely noticed at the center of weld bottom in the case e) are faded away in the case f) and g).

In order to demonstrate the effect of welding synergy when a defocused laser beam welding and a gas metal arc process is combined into a laser-arc hybrid process, set of bead-on-plate trials were executed. Figure 3 presents an example of cross-sections of a separate melt runs from plain (3a) Metal Inert Gas (MIG) and (3b) defocused laser welding and also when preceding separate process are combined into a (3c) laser-arc hybrid process.

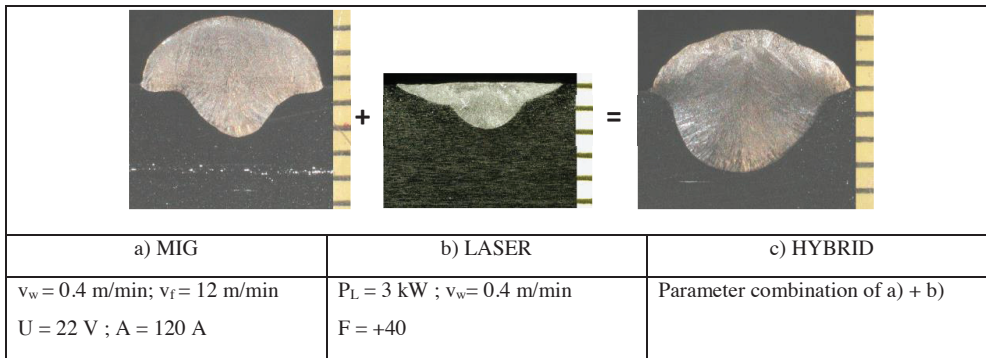


Fig. 3. Macro cross-sections of bead-on-plate welds produced by a) MIG process alone, b) defocused autogenously laser process and c) combined laser-arc hybrid process of a) + b).

In used hybrid process, an arc torch is applied in leading position. As arc is melting the surface of the work piece in advance, that could in some extent assist defocused laser beam in terms of advanced beam absorption at the work piece and vice versa laser beam can provide a hot spot for enhanced arc ignition. The influence of above mentioned synergy effects on the shape of the hybrid weld bead can be seen when cross-sections a), b) and c) in Figure 3 are evaluated: Even though a laser beam is strongly defocused, the penetration in the hybrid weld is a bit deeper (MIG and laser = 2 mm vs. hybrid = 3.4 mm) and the shape of penetration is more evenly distributed on lateral regions of the weld bead than in MIG or laser weld bead.

3.2. Gap filling experiments with 10 mm thick test pieces

The idea of gap filling experiments with 10 mm test pieces was to demonstrate the parameters needed and the ability to fill thicker plates (20 and 60 mm). Therefore the sizes of the tested gap width were chosen to emulate corresponding gap widths which will occur in the case of 60 mm thick joint configuration.

Experiments started with welding of 10 mm thick test pieces using a keyhole-mode hybrid welding in root pass and conduction limited hybrid welding in filling pass. The used set-up of laser-arc/filler wire interactions is presented in Figure 4. Base material used in these tests was AlloyX and filler metal was Autrod 308LSi wire in 0.8 mm diameter. In this series of conduction limited hybrid welding experiments the main interest was laid on the feasibility to bridge and fill grooves with gap widths up to near 11 mm. The used groove geometries consisted of open joint preparations with a 1 mm root gap, a 5 mm root face and different upper square gap opening widths between 6.8 and 10.8 mm, Figure 5.

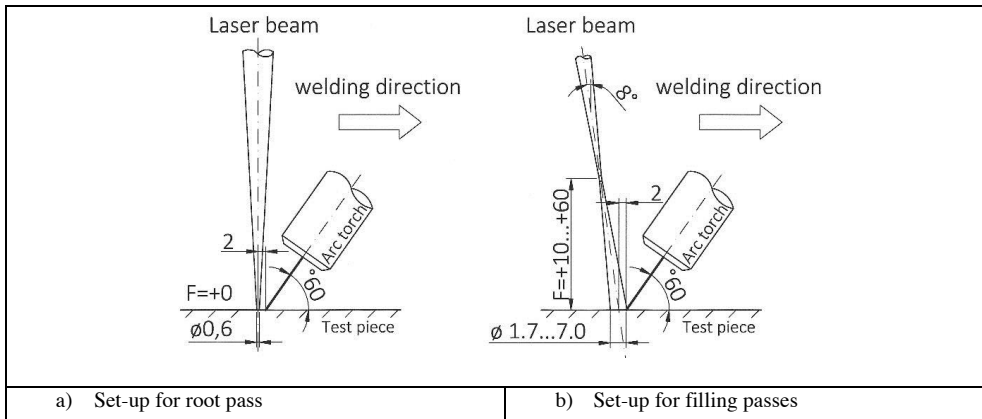


Fig. 4. Set-up used in welding tests: a) Key-hole mode in welding of root pass and b) Conduction limited mode in welding of filling passes. F number (e.g. 0, +10...+60) indicates focal point position.

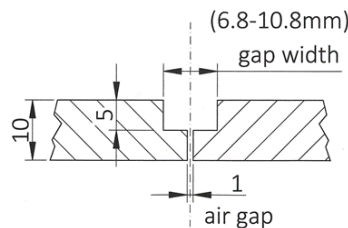


Fig. 5. The groove geometry used in the experiments with 10 mm thick test pieces. Varied gap widths were between 6.8mm and 10.8 mm.

Once operating inside conduction limited welding regime, the beam spot size should be adjusted with defocusing such that the beam spot is a bit smaller than the gap of the groove. By doing so, the access of the beam path down to the groove bottom is ensured. On the other hand, to avoid a lack of fusion between the weld bead and the fusion faces, the beam spot should not be too small-sized compared to the gap width to be welded, because melting effect towards fusion faces could be then remained too low or even non-existent if the heat of the beam will not properly reach the side walls of the groove, although an arc melting effect is also present and contributes in hybrid welding.

The first test weld B2 (Figure 6a) was welded in nearly 7 mm wide gap. In this case a defocusing value of +40 mm, which gave a beam spot diameter of ~4.9 mm was applied. The macro cross-section (Figure 6a) shows that the welding heat has reached the side walls of the groove and also the volume of filler wire feeding respect to the groove volume has been sufficient as the filling pass exhibits a bit concave surface. In test weld B4, where a gap width to be bridged was increased to 9 mm, the diameter of beam spot was enlarged by increasing the defocusing value to the value of +50 mm, which corresponds roughly a beam spot diameter of ~5.9 mm. Welding speed used earlier in the

test weld B2, was reduced from 0.5 m/min to 0.3 m/min and the filler wire feeding was tuned a bit higher to accommodate the grown groove volume in the case of weld B4. Judging from the macro cross-section of test weld B4 in Figure 6b, the elevated defocusing value of +50 mm combined with the proper amount of wire feeding and welding speed is successfully applied to the groove. As contemplating the test weld B5, it was welded into the groove which had 10.8 mm gap width. Welding speed was kept in 0.3 m/min but filler wire feeding was tuned a bit higher to accommodate grown groove volume in the case of weld B5. In order to get the fusion faces of wider groove melted, the spot size of the beam was enlarged from ~5.9 mm to ~7 mm by enhancing defocusing from value F=+50 mm to F=+60 mm. It can be seen from the macro cross-section of Figure 6c that the welding heat has reached the side walls of the groove and even gap width of 10.8 mm can be successfully bridged and filled using defocusing technique.

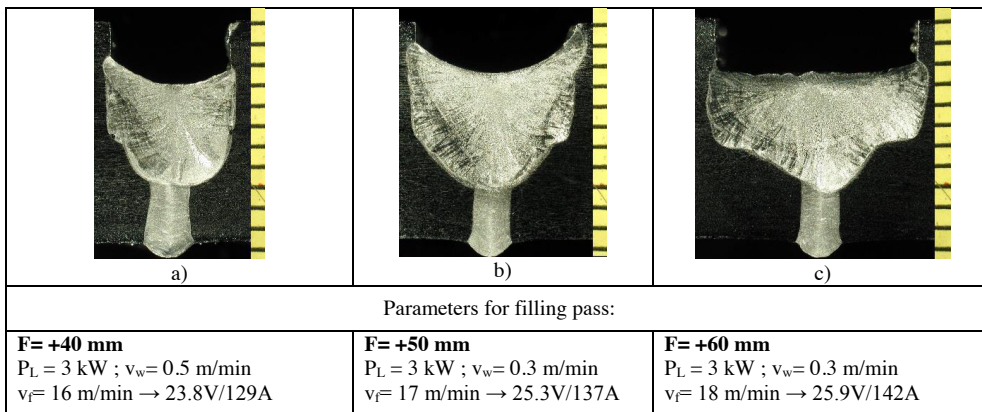


Fig. 6. Macro cross-sections from the defocusing trials applied to laser-arc hybrid welding of different groove gaps.

3.3. Gap filling experiments with 20 mm thick test pieces using multi-pass cold wire and hybrid process

In the case of laser welding with filler wire, wire is introduced as a solid form into the laser induced weld pool. As the wire is entering into the interaction zone of the laser impingement point, a part of laser power is reflected away from the wire and a certain part is absorbed into the wire causing wire heating and melting. In addition to above, a part of power of laser beam is also consumed to the heating and melting of the base material. As compared laser welding with filler wire (cold wire) to laser-arc hybrid welding, melting of filler wire is taken place in a bit different way: Before entering into the laser induced weld pool zone, filler wire is already melted by the arc source and it is introduced into the weld pool in molten spray of droplet form. That is why the melting efficiency in laser-arc hybrid welding is far better than in laser welding with filler wire.

Some bead-on-plate welding trials on AISI 316L-A plate were carried out in order to get suggestive data what kind of the effect different defocusing settings of laser beam has on the melting capacity of filler wire and the emerging width of weld bead. In the trials the filler wire was guided through the same GMA-torch which will be used in hybrid trials, only a grounding cable shoe was disconnected from the fastening table to enable the use cold wire welding. In the above case of laser welding with filler wire, the trials demonstrated the limits for the maximum filler wire feeding for five focal position variants. It came evident that as the level of focal position was enhanced, the power density of laser beam was decreased and the corresponding maximum wire feeding rate was decreased as well. If maximum wire feeding rates were exceeded, melting behaviour started to fluctuate causing spatters and uneven weld surface because the melting capability of laser beam was not enough as the limit was reached. The used focal point position variants and corresponding maximum wire feeding rates and widths of the produced weld beads are presented in Table 3.

Next, it was prepared a couple of 20 mm thick test specimens which had groove geometries with different gap width in order to test limits for groove filling capability in case of defocused multi pass wire welding. The groove geometries and corresponding weld cross-sections can be seen in Figure 7.

Table 3. The results of filler wire melting capability trials concerning laser welding with filler wire.

Focal position [mm]	Max. filler wire feeding rate [m/min]	Width of melted weld bead [mm]
+ 10	5.5	2.6
+ 20	3.5	3.3
+ 30	3.0	5.3
+ 40	2.5	6.3
+ 50	2.0	7.2

Laser power: $P_L = 3$ kW; Focal length: $FL = 200$ mm; Welding speed: $v_w = 0.3$ m/min; Filler wire: Autrod 316LSi, $\varnothing 1.0$ mm

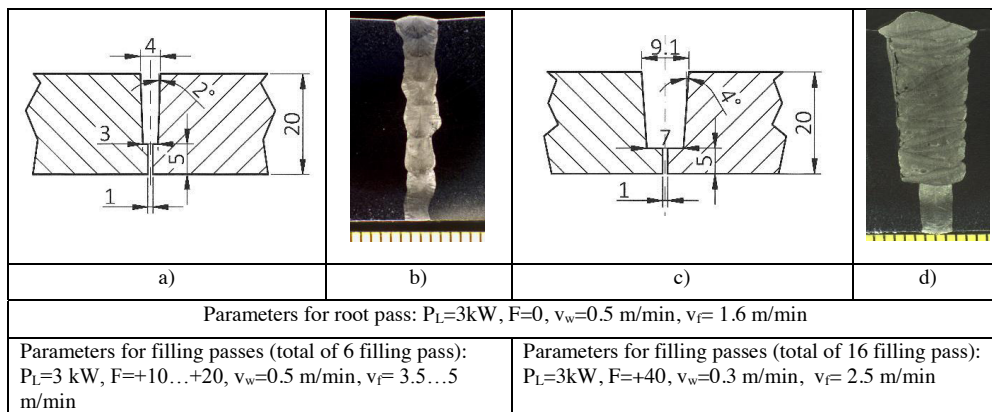


Fig. 7. Groove geometries used in cold filler wire multi pass tests and corresponding weld macro cross-sections.

As can be judged from the weld macro cross-section of the Figure 7b, the groove geometry with 3...4 mm wide gap depicted in Figure 7a was successfully filled when the total of 7 filling passes were needed. Because the welding of 60 mm joint thickness range was considered as a final target, this 20 mm part depicted in Figure 7a/b was anticipated to deploy for welding of the first 1/3 bottom portion of 60 mm thickness if it will turn out that a hybrid welding torch cannot be fitted and deployed near the bottom of the groove portion. Above stems from the fact that in cold wire welding up to ~40 mm wire stick-out/electrode extension can be used whereas in hybrid welding wire stick-out needs to be less than 20 mm to ascertain fluent arc behaviour. When concerning the welding results of wider groove configuration shown in Figure 7c, it came obvious already during the welding that the used groove geometry was far too wide in this case for laser welding with cold filler wire. As it can be seen in Figure 7d, a severe lack of fusion defects can be noticed all the way on the left side of the fusion face. Lack of fusion is caused from insufficient melting of fusion face of the groove. Because of the wide groove, laser beam spot is forced to be widened in order to try to get also groove faces melted. A larger beam spot with the focal point position value of $F=+40$ leads to a decreased power density which in side deteriorates the melting capacity when applied in laser welding with cold filler wire. As a consequence, groove filling was left poor because low filler wire feeding rate (~2.5 m/min) could be used. A total of 17 passes had to be made in order to fill whole 20 mm thickness.

In defocusing trials with hybrid process, the defocusing value of $F=+50$ mm was tried at first. The cross-section of multi-pass weld in Figure 8b showed that filling of 9...11 mm wide groove geometry (Fig. 8a) was successfully carried out with root pass and five filling passes. The following trial was made using ~3 mm wider groove (Fig. 8c) compared to the former one: The first three filling passes were made using the defocusing value of $F=+50$ mm and then continued with $F=+60$ mm for the last three filling passes. In this case the groove geometry was too wide to be completely melted, Fig. 8d. Using the current laser-arc hybrid set-up, the limit of bridgeable groove width lies around the value of 11 mm. A total of 7 passes (root pass + 6 filling pass) were made in order to fill the whole 20 mm thickness. When the results of defocusing trials are compared between the laser cold wire and laser-arc hybrid process, it can be judged that when using hybrid welding where filler metal are pre-melted via an arc torch, a much wider groove than in laser welding with cold filler wire can be used.

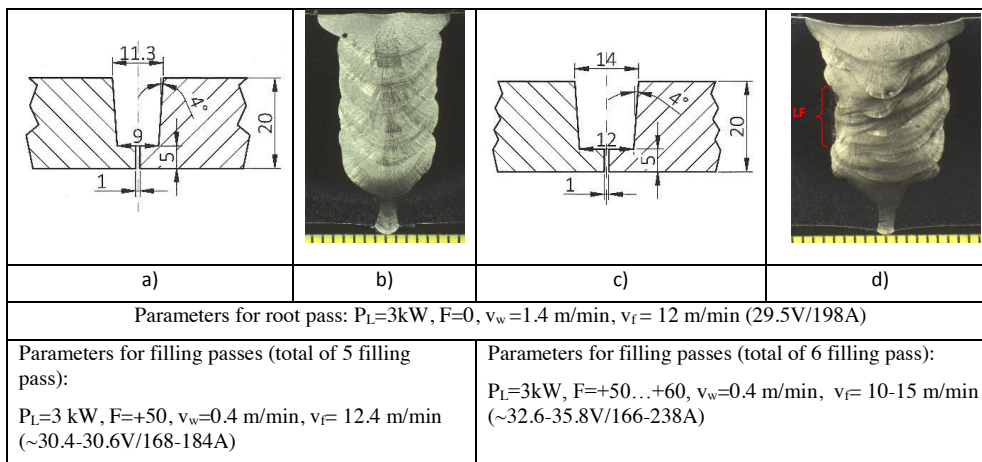


Fig. 8. Groove geometries used in laser-arc hybrid multi-pass tests and corresponding weld macro cross-sections.

3.4. Gap filling experiments with 60 mm thick test pieces using multi-pass cold wire and hybrid process

The final welding trials of the defocusing experiments were dedicated to filling tests of 60 mm thick groove geometries. The first approach was to use a procedure which deploys laser welding with filler wire for the first ~1/3 thickness of 60 mm and then continues with using laser-arc hybrid welding to fill the remaining ~2/3 of joint thickness. Welding parameters were adopted from the preliminary welding trials described earlier. As narrow gap joint thickness grows up to 60 mm, the used bevel angle has to be maintained as small as possible to avoid excessive width of groove opening at the surface side of test piece. At first, it was decided to use the groove geometry with both inner bevel angle of 2 degrees and upper bevel angle of 4 degrees, Figure 10a. When a narrow gap welding procedure is used, the challenge which will come up is how to introduce the filler wire into the very bottom of the groove. In practice, this means that a wire feeding nozzle or an arc torch has to be extremely narrow in order to fit near the bottom of the narrow groove. Especially, when the arc-source is used, electrode extension length has to be kept less than 20 mm (Figure 9b) in order to maintain smooth molten metal transition and robust welding process. That is why at the first trial, it was decided to use cold wire laser welding without an arc-source in welding of the first 25 mm of the groove thickness. In the cold wire method the length of the wire extension from the tip of the wire nozzle was set to 40 mm (Figure 9a). When contemplating the cross-sectional macrograph of multi-pass welds B22 and B23 (Figure 10b and 10c), it can be noticed that filling passes have successfully filled the groove and overlapped enough each other. In the weld B22, ten cold wire filling passes were first produced using the defocusing value of $F=+20$, 3.5 m/min wire feeding (316LSi wire) and 0.5 m/min welding speed. For the upper groove filling of weld B22, nine laser-arc hybrid welded passes were needed. The used defocusing values were $F=+30\dots+50$, whereas wire feeding was 13...19.5

m/min and welding speed 0.6 m/min. A total of 20 passes including the root pass were needed to fill 60 mm thickness. In the weld B23, a total of eight cold wire filling passes were first produced using the defocusing value of $F=+20\dots+30$, 3...3.5 m/min wire feeding and 0.35 m/min welding speed. After cold wire passes, six laser-arc hybrid passes were made for the rest upper groove region. Eventually, a total of 15 passes including the root pass were needed to fill whole 60 mm thickness of the multi-pass weld B23.

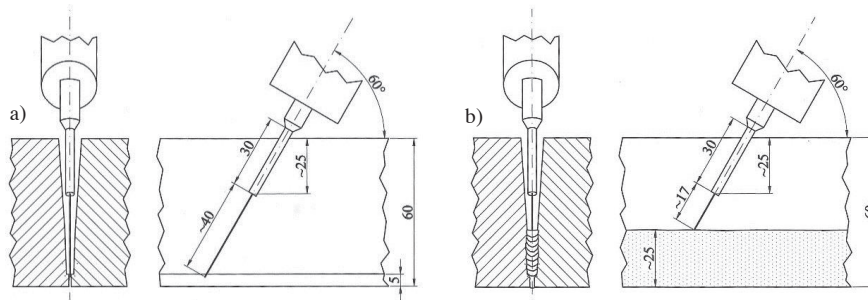


Fig. 9. a) Configuration for laser welding with cold filler wire in filling of lower 25mm portion. b) Configuration for laser-arc hybrid welding of upper 35 mm portion.

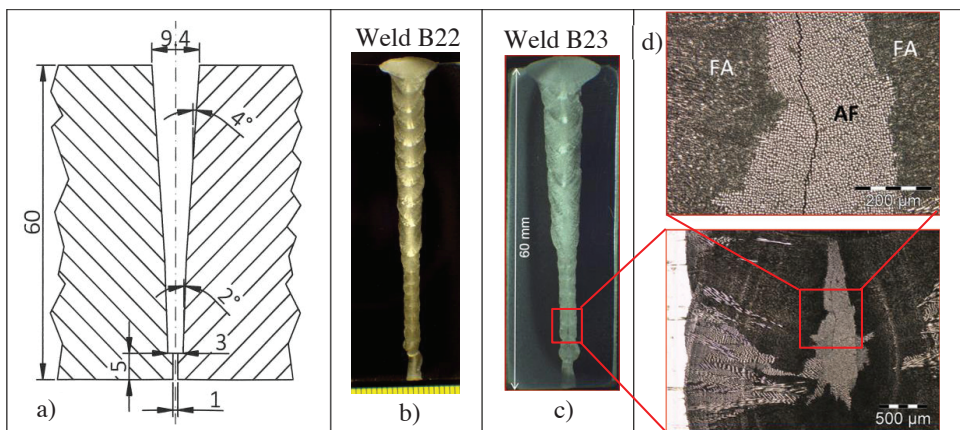


Fig. 10. a) Groove geometry used in gap filling multi-pass tests: both cold wire and laser-arc hybrid method was used as described in Fig. 9. b/c) The corresponding weld macro cross-sections of multi-pass weld B22 and B23. d) Micrographs from the weld B23 exhibiting solidification cracking propagating in primary austenitic solidified region.

During welding, it was noticed that solidification cracking occurred in three laser-arc hybrid filling passes in multi-pass weld B22. Those cracks were located in the passes which were approximately in the middle of the whole groove thickness of 60 mm. Cracking was clearly detected visually as the cracks were propagated to the surface of the pass and located longitudinally at the weld centre line. In Figure 11, it can be seen a picture taken from the hot crack before the next filling pass was continued. On the other hand, when cross-sectional macrograph of completed multi-pass

weld B22 is observed, hot cracks seem to be healed by re-melting of a consequent overlapping filling pass. When microstructures were studied in the test weld B23, it was found also a solidification crack emerging in cold wire welded pass: It can be seen that the major portion of the weld microstructure has been solidified in primary ferritic mode and the crack path is propagated in the primary austenitic solidified island located at the weld centre line, Figure 10d. The same sort of cracking observations in fast solidified EB-welds has been also reported by Lippold (1985).



Fig. 11. Top view from above of narrow gap groove. A hot crack propagated to the surface of the laser arc-hybrid filling pass during the welding of multi-pass weld B22.

As a laser-arc hybrid welding was proved to be a more efficient method in terms of groove filling than a plain laser welding with cold wire, it was decided to make couple of trials in which a whole 60 mm deep groove from the root up to the capping run was tried to fill using laser-arc hybrid welding. In order to reach the bottom of the groove, a special 90 mm long and thin contact nozzle for above trials was prepared. Figure 12a shows the groove geometry used for the first hybrid welding trials of 60 mm thick test piece D1. The following range of variable parameters for filling passes was used: Focal point position $F=+50\dots+60$ mm, welding speed 0.4 m/min, filler wire feeding rate 12...23.5 m/min ($U=25\dots31.2V/I=166\dots230V$). In weld D1 total of 15 passes were needed. That is 5 passes less than in the case of test weld B22. When examining the cross-sectional macrograph of weld D1 in Figure 12b, it can be noticed that lack of fusion defects occur on the both side of groove fusion face. In this case groove geometry was too wide to be completely melted. To get groove fusion faces properly melted, it is decided to modify a little bit the existing groove geometry. In this new groove configuration (Figure 12c), the width of the groove at the very bottom of the groove was decreased to the value of 4 mm, enabling a bit narrower groove cross-section at the lower area than used in the earlier groove version. This new improved configuration chosen to be deployed in test piece E2 is practically the narrowest possible, which just allows access for the used contact electrode nozzle to the near bottom of the groove. Welding parameters were a little bit adjusted from the test weld D1 such a way that welding speed for the filling passes was a bit decreased and filler wire feeding rate was adjusted accordingly. In addition, at the each pass the diameter of laser beam spot size was tried to adjust according to the concurrent width of the groove by using defocusing of laser beam. The following range of variable parameters was used: Focal point position $F=+35\dots+65$ mm, welding speed 0.25...0.35 m/min, filler wire feeding rate 9...15 m/min ($U=27\dots32V / I=177\dots240V$). The macrograph of produced multi-pass test weld E2 can be seen in Figure 12d. In multi-pass weld E2, total of 10 passes were needed to fill the whole joint thickness of 60 mm. When examining the cross-sectional macrograph of multi-pass weld E2, it can be noticed that fusion between the filling passes and the groove edges are complete. This confirms the significance of correctly adjusted defocusing and a diameter of laser beam spot size respect to the width of the groove. In the case where bevelled Y-shape groove is used, the size of the laser beam spot diameter has to be gradually increased in each filling pass. In order to secure the side wall fusion, the diameter of laser beam spot size needs to be adjusted by defocusing near the same as the width of the current groove.

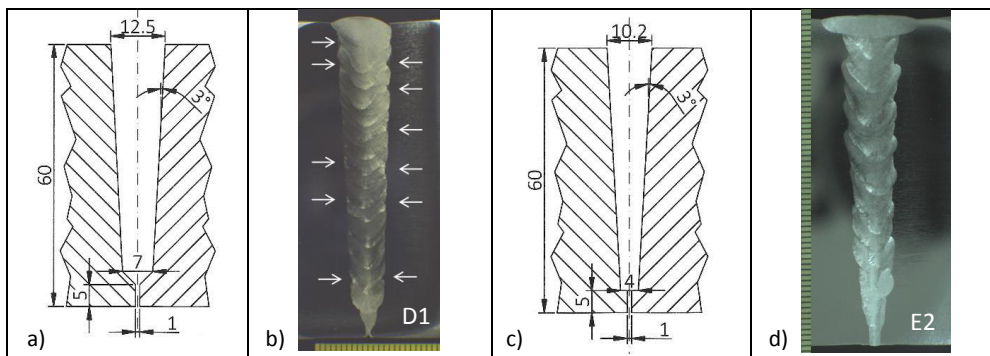


Fig. 12. a/c) Groove geometries used in the gap filling of entire laser-arc hybrid multi-pass tests, b/d) the corresponding weld macro cross-sections of multi-pass weld D1 and E2. The white arrows are pointing the lack of fusion defects in weld D1. A total of 15 and 10 laser-arc hybrid passes were needed in D1 and E2, respectively.

4. Conclusions

Series of conduction limited welding tests for austenitic stainless steel joints were carried out using a combination of 3 kW Nd:YAG laser and MIG/cold wire welding process. In this conduction limited process variation, a size and power density of a laser beam spot was purposely dispersed by using a defocusing technique. The experiments demonstrated that by using the described defocusing technique and conduction limited hybrid method in welding of filling passes even a gap width of near 11 mm can be bridged and filled. In order to avoid lack of fusion defects between the filling passes and groove sides, the size of the laser beam spot should be properly set to respect with the groove width to be welded. A narrow gap configuration set special requirements to contact/wire feeding nozzle because of limited space. Especially, the bottom portion of a deep groove is challenging to reach in the case of an arc. In that sense, a laser welding with cold filler wire without an arc in root pass and couple of consequent filling passes will enable easier operation in narrow groove because wire stick-out could be risen up to 40 mm. Contrary to laser-arc hybrid welding wire stick-out should not exceed 20 mm. Results showed that the groove filling efficiency is much better when using laser-arc hybrid welding than in laser welding with cold filler wire. Extra heat source of GMAW enables wire melting before it enters to the laser induced melt pool. When using laser welding with cold filler wire for the first 20-25 mm weld thickness and then laser-arc hybrid welding for the rest upper 35-40 mm thickness, a total of 15 to 20 passes was needed to complete the 60 mm thick multi-pass weld. As laser-arc hybrid multi-pass welding was used alone, it was managed to fill 60 mm thick joint with 10 passes. In metallurgical point of view the combination of base and filler material used in the welding experiments was found to be susceptible to weld solidification cracking.

References

- Arata, Y., Maruo, H., Miyamoto, I. and Nishio, R., High Power CO₂ Laser Welding of Thick Plate – Multipass Welding with Filler Wire, Transactions of JWRI, Vol.15 No.2, 1986, pp. 199-206.
- Jokinen, T., Karhu, M. and Kujanpää, V., Welding of Thick Austenitic Stainless Steel Using Nd:Yttrium-Aluminum-Garnet Laser with Filler Wire and Hybrid Process, Journal of Laser Applications, Vol.15 (2003) No:4, pp. 220-224.
- Lippold, J.C., Centerline Cracking in Deep Penetration Electron Beam Welds in Type 304L Stainless Steel, Welding Journal, 64(5), 1985, pp. 127S-136S.
- Phaoniam, R. et al., Development of a highly efficient hot-wire laser hybrid process for narrow-gap welding—welding phenomena and their adequate conditions. Welding in the World 57, 2013, pp. 607–613.
- Rethmeier, M. et al., Laser-Hybrid Welding of Thick Plates up to 32 mm Using a 20 kW Fibre Laser, Q. J. Jpn. Weld. Soc. 27(2), 2009, pp. 74-79.
- Zhang, X., Developments in multi-pass laser welding technology with filler wire, Handbook of Laser Welding Technologies, Woodhead Publishing Limited, 2013, edited by Katayama, S., part III, chapter 17, pp. 459-477.

Publication III

Sohail, M., Karhu, M., Na, S-J., Han, S-W. and Kujanpää, V.
**Effect of leading and trailing torch configuration on mixing and fluid behavior of
laser-gas metal arc hybrid welding**

Reprinted with permission from
Journal of Laser Applications
Vol. 29, pp. 042009-1-14, 2017
© 2017, Laser Institute of America



Effect of leading and trailing torch configuration on mixing and fluid behavior of laser-gas metal arc hybrid welding

Sohail Muhammad

Department of Mechanical Engineering, KAIST, Daejeon 34141, South Korea and Department of Materials Engineering, NEDUET, Karachi 75270, Pakistan

Karhu Miikka

Department of Mechanical Engineering, Lappeenranta University of Technology, P.O. Box 20, FI-53851 Lappeenranta, Finland

Na Suck-Joo^{a)}

Department of Mechanical Engineering, KAIST, Daejeon 34141, South Korea and VTT Technical Research Centre of Finland, P.O. Box 20, FI-53851 Lappeenranta, Finland

Han Sang-Woo

Department of Mechanical Engineering, KAIST, Daejeon 34141, South Korea

Kujanpaa Veli

VTT Technical Research Centre of Finland, P.O. Box 20, FI-53851 Lappeenranta, Finland

(Received 21 April 2017; accepted for publication 4 October 2017; published 31 October 2017)

The paper introduces the results of mixing and fluid flow studies for full penetration laser-gas metal arc (GMA) hybrid welding with GMA leading and trailing torch configuration. The material used was austenitic stainless steel with the thickness of 10 mm. The joint configuration was butt joint without gap. It was found that the molten pool at the root side is a longer time in the molten state than the pool at the weld surface. Compared to autogeneous laser welding, the addition of GMA makes the upper bead wider. This effect is more prominent in the case of GMA trailing compared to the case of GMA leading. The simulation results also show a similar trend of bead shape change in the case of GMA leading and trailing configuration compared to the experimental ones. Mixing behavior of filler and base metal is also evaluated and compared by both experimental studies and simulations. In GMA leading configuration, the mixing is more pronounced in the upper part of the weld cross section, while in GMA trailing, the mixing is more efficient in the whole cross section compared to GMA leading case. Simulation results support this difference in mixing behavior. Laser is the main source that provides full penetration and forms a molten pool on upper and root surface. The direction of wire feeding affects the mixing behavior. In GMA leading configuration the wire droplets impinge in front of the laser beam and in the front edge of the molten pool, whereas in GMA trailing configuration, the wire droplets impinge behind the laser beam where the molten pool is fully developed. This causes the difference in mixing. © 2017 Laser Institute of America. <https://doi.org/10.2351/1.5008304>

Key words: laser-GMA hybrid welding, element mixing, GMA leading, GMA trailing, volume of fluid method, full penetration, keyhole, fiber laser

I. INTRODUCTION

Hybrid laser-gas metal arc (GMA) welding combines the processes of both GMA and laser welding enabling fast welding speed and deep penetration. The advancement in fiber laser technology has made it possible to weld thick sections with a single pass. The processes of laser welding and GMA welding alone are quite complex multiphysics phenomena, which make it more complex when they are combined together. Laser welding in partial and full penetration shows different characteristics. Addition of GMA in leading or trailing configuration can also affect the flow behavior, which, in turn, would affect the mixing of GMA wire in the melt pool. Zhang *et al.*^{1,2} studied the metal transfer mechanism for

hybrid welding and they found that plasma has considerable influence on electrode melting, droplet formation, detachment, impingement onto the work piece, and weld morphology. They also studied the effect of laser leading and trailing configuration on plasma and metal transfer in hybrid welding for CO₂ lasers. They found that laser leading configuration (i.e., GMA trailing) yields a more stable arc due to increase in arc conductivity augmented by the laser beam. Zhao *et al.*³ studied the flow and mixing characteristics of laser leading and trailing configuration for CO₂ laser by experimental means in full penetration welding with gaps of 0, 0.5, and 1.0 mm. They conclude that the inward flow, i.e., the fluid flow toward the inside of the keyhole, is important in uniform mixing. In laser leading case, i.e., GMA trailing mixing is stronger than in laser trailing, i.e., GMA leading. Wei *et al.*⁴ used double GMA sources on both sides of laser, to study the arc characteristic and metal transfer in double GMA hybrid

^{a)}Author to whom correspondence should be addressed; electronic mail: sjoona@kaist.ac.kr. Telephone: +82-42-350-3216.

welding. They found that one gas metal arc is active at a time at lower current and the arcs change to synchronous arcing at higher currents. Karhu *et al.*⁵ studied the filler wire mixing in laser-GMA and laser-cold wire welding in both laser leading and laser trailing configurations, using fiber laser. They found that laser-arc hybrid welding is better in terms of mixing as compared to laser-cold wire welding, and the near top surface mixing is higher when compared to lower regions near the weld root.

Experimental studies are costly and give very little insight into flow behavior, and therefore, simulation studies are needed. Modeling of the process involves complex multi-physics phenomena, which include multiple reflection inside keyhole, arc heat source, recoil pressure, Marangoni flow, bubble pressure model, etc. Some studies were carried out for laser welding, GMA, and hybrid welding with partial penetration.⁶⁻¹² Partial penetration welding poses a danger for porosity in the bottom of the melt pool. This, usually, is not the case when using full penetration. Numerous studies are available, which have taken into consideration the full penetration welding by using fiber laser. Avilov *et al.*¹³ performed the full penetration welding of AlMg₃ 30mm thick plate. They proposed the use of inductive support to prevent the gravity dropout of liquid metal. Bachmann *et al.*¹⁴ performed the numerical and experimental investigation of inductive weld pool support for AISI 304 steel. They found the optimal parameters for magnetic field needed to support the gravity dropout. Zhang *et al.*¹⁵ performed the optimization of full penetration laser welding of 12 mm stainless steel plate. They found that along with welding parameters the defocusing of laser beam plays an important role in the optimization process. In addition, assist gas application used in root surface side could improve the process stability and bead geometry. Zhang *et al.*⁹ extended the application of laser welding model developed by Cho *et al.*⁷ to full penetration welding and they found that the flow in full penetration welding is periodic in nature and lower surface of molten pool at the root side may be longer and more unstable than the upper surface.

In the present work these models are extended to study and compare the flow and mixing behavior in full penetration laser-GMA hybrid welding using the GMA leading and

TABLE I. Hybrid welding parameters.

Description	Values
Laser power	10 kW
Focal point position	4 mm below surface
Welding speed	1.3 m/min
GMAW average voltage	25 V
GMAW average current	95 A
Wire feeding speed	5 m/min
Wire stick out	15 mm
Wire diameter	1 mm solid wire
Torch angle	65°
Horizontal interaction distance between laser spot and wire tip	3 mm
Shielding gas	Ar + 2% CO ₂ + 30% He + 0.03% NO
Shielding gas flow rate	24 l/min

TABLE II. Composition of base metal (AISI 316L).

Element	C	Mn	Si	P	S	Cr	Ni
wt. %	0.024	1.7	0.37	0.02	0.0002	17.6	12.3
Mo	Ti	Ta	Nb	Cu	B	Co	N
2.43	0.005	0.003	0.005	0.1	0.0003	0.03	0.07

trailing configuration. The results achieved from modeling are compared with the experimental results. The main purpose of the work was to gain understanding from the melt flow behavior of laser-GMA hybrid welding with the help of simulation. Especially, the effect of GMA torch orientation and its implication on emerging melt flow and weld metal mixing was in interest.

II. EXPERIMENTAL PROCEDURE

Experiments were performed on austenitic stainless steel AISI-316L by using a combination of pulsed GMA and 10kW fiber laser welding. The welding parameters used are shown in Table I. The composition of filler wire and base metal had some difference in terms of Cr and Ni concentration, for providing a sufficient contrast of alloying elements in the fusion zone. Tables II and III list the composition of alloying elements in the base and filler metal. Cr and Ni concentrations were 17.6% and 12.3% in the base metal, while in the filler wire, the concentrations were 22.9% and 8.7%, respectively. A 10 mm thick plate was welded using closed butt joint as shown in Fig. 1. The properties of the fiber laser used in the current experiment and simulation are summarized in Table IV.

III. MATHEMATICAL MODELS

A. Full penetration laser welding

The governing equations used for modeling full penetration laser welding were similar to the ones used in the partial penetration welding described in Ref. 6. The difference, however, was in the application of vapor plume heating, vapor shear stress, and vapor recondensation flux. In the case of full penetration autogenous laser welding, the model used by Zhang *et al.*⁹ was implemented. The shear stress induced by vapor in partial penetration welding was zero at the bottom of the keyhole and increased linearly toward the keyhole exit, as shown in Fig. 2(a). On the other hand, in full penetration welding, there are two exits; one at the top surface and another at the root surface. Therefore, the shear stress induced by vapor was assumed to be zero at the middle of the keyhole and increase linearly toward both exits, Fig. 2(b). Contrary to the partial penetration welding case, Fig. 2(c), metal vapor induced heat source was applied on both sides of the keyhole extending to the middle of the work piece, Fig. 2(d). In the

TABLE III. Composition of filler wire (wt. %).

C	Si	Mn	P	S	Cr	Ni	Mo	Nb+Ta	Cu	N
0.010	0.36	1.6	0.017	0.0	22.9	8.7	3.20	0.0	0.08	0.147

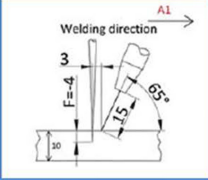

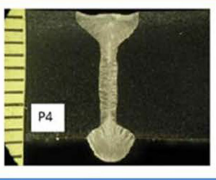


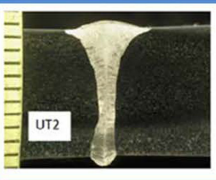
Configuration	Laser and GMA arrangement	Groove Shape	Bead Shape
A1 + B1 GMA leading without gap			
A2 + B1 GMA trailing without gap			

FIG. 1. Summary of experiments.

case of full penetration laser welding with the addition of a GMA source, the models developed for vapor recondensation flux were also implemented, Fig. 3. In the case of full penetration welding, a radiation heat source was applied on the top and bottom surface, Fig. 3(a). In addition, the vapor recondensation flux was applied increasing linearly from the middle of the plate toward the top and root openings of the keyhole, Fig. 3(b).

B. Governing equations for laser-GMA hybrid welding

Mainly three-dimensional transient simulations were carried out for laser-GMA welding. Here, the mass conservation equation, the momentum conservation equation, referred to here as the Navier–Stokes equation, the energy conservation equation, and the volume of fluid (VOF) equation were used as governing equations to execute the molten metal flow analysis. An additional equation for alloying element conservation was used to investigate the mixing of Cr. The molten metal was treated as a Newtonian flow, considering the fluid to be an incompressible laminar flow. Based on these assumptions, the aforementioned governing equations were solved.

TABLE IV. Properties of fiber laser used.

Parameters	Values
Wavelength (μm)	1070
Polarization	Circular/Random
Beam quality (M^2)	25.1
Beam quality, Beam Parameter Product (mm mrad)	8.467
Focal length (mm)	300
Beam diameter on optics (mm)	16.777
Focusing number	18
Focal radius (μm)	303
Rayleigh length (mm)	10.844

C. Mass conservation equation

$$\nabla \cdot \mathbf{V} = \frac{\dot{m}_s}{\rho} \tag{1}$$

Here, \mathbf{V} is the velocity vector and \dot{m}_s is a mass source term by molten drops.

D. Navier–Stokes equation

$$\frac{\partial \mathbf{V}}{\partial t} + \mathbf{V} \cdot \nabla \mathbf{V} = -\frac{1}{\rho} \nabla P + \nu \nabla^2 \mathbf{V} - K \mathbf{V} + \frac{\dot{m}_s}{\rho} (\mathbf{V}_s - \mathbf{V}) + \mathbf{G}, \tag{2}$$

where $K = C(F_s^2)/((1 - F_s)^3 + B^*)$.

Here, ρ is the fluid density, P is the pressure, ν is the dynamic viscosity, K is the drag coefficient for a porous media model in the mushy zone, \mathbf{V}_s is the velocity vector for the mass source, \mathbf{G} is the body acceleration due to body force, C is a constant representing mushy zone morphology, F_s is the solid fraction, and B^* is the positive zero used to avoid division by zero. The third term of the right hand side of Eq. (2) is the source term for the frictional dissipation in the mushy zone. Here, the Carman–Kozeny equation derived from the Darcy model is used to model the flow in the mushy zone based on the assumption that this region can be treated as a porous media.¹⁶ The fourth term is the additional term for considering the mass source by molten drops.

E. Energy conservation equation

$$\frac{\partial h}{\partial t} + \mathbf{V} \cdot \nabla h = \frac{1}{\rho} \nabla \cdot (k \nabla T) + \dot{h}_s \tag{3}$$

where $h = C_p T + f(T)L_f$.

Here, h is the enthalpy, k is the thermal conductivity, T is the temperature, and \dot{h}_s is an enthalpy source term due to mass

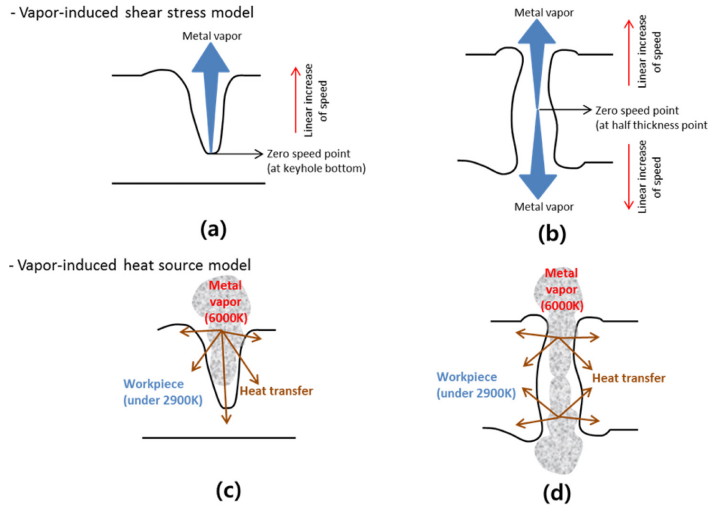


FIG. 2. Shear stress and vapor heat source models for full and partial penetration welding.

source. The enthalpy-based continuum model was used to consider the solid-liquid phase transition where C_p is the specific heat, L_f is the latent heat of fusion and $f(T)$ is the temperature dependent function as

$$f(T) = \begin{cases} 0 & (T \leq T_s) \\ \frac{T - T_s}{T_l - T_s} & (T_s \leq T \leq T_l) \\ 1 & (T_l \leq T) \end{cases}$$

Here, T_s and T_l are solidus and liquidus temperature.

F. VOF equation

$$\frac{\partial F}{\partial t} + \nabla \cdot (VF) = \dot{F}_s \tag{4}$$

Here, F is a volume-of-fluid and \dot{F}_s is the change of the volume fraction of fluid associated with the mass source \dot{m}_s in the continuity equation.

G. Additional conservation equation (alloying element distributions)

$$\frac{\partial \phi}{\partial t} + \nabla \cdot (V\phi) = \dot{\phi}_s \tag{5}$$

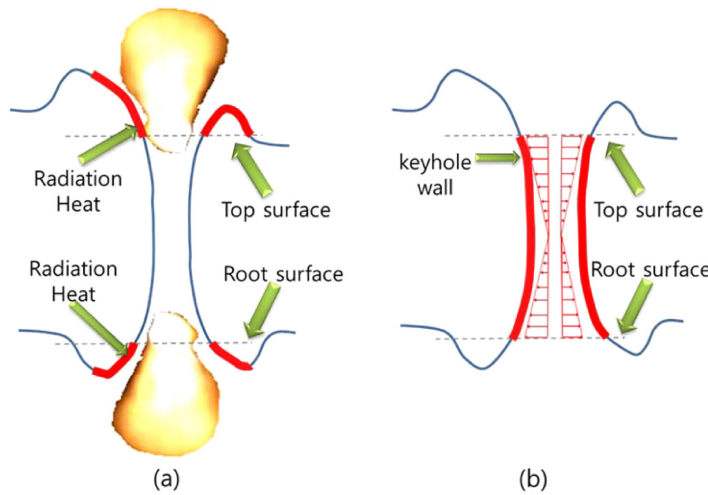


FIG. 3. Vapor plume and recondensation heat source in full penetration welding.

Here, $\dot{\theta}_s$ is the scalar source term added by an alloying element in the molten drops, while the diffusive effects of the alloying element are not considered. By Eq. (5), a scalar quantity indicates the weight percentage of alloying element in a cell that cannot only be conserved but is also affected by the molten pool flow.

H. Arc welding models

The heat source of the electric arc can be modeled as a surface heat flux with a Gaussian function of below equation

$$q_A(x, y) = \eta_A \frac{VI}{2\pi r_A^2} \exp\left(-\frac{x^2 + y^2}{2r_A^2}\right). \quad (6)$$

Here, η_A is the arc efficiency, r_A is the arc root radius, and V and I are the electric voltage and current of the arc, respectively. The arc efficiency was assumed to be 0.56 for the arc plasma. The heat input efficiency of the droplet was 0.24 in this simulation; therefore, the total efficiency of GMA welding is 0.8.¹⁷ The heat input from droplets were determined using procedure highlighted by Cho *et al.*¹⁸ The pressure boundary condition of the arc plasma can be modeled by the Gaussian-like function of Eq. (7)¹⁹

$$P_A(x, y) = \frac{\mu_0 I^2}{4\pi r_A^2} \exp\left(-\frac{x^2 + y^2}{2r_A^2}\right). \quad (7)$$

Here, μ_0 denotes the magnetic permeability of free space.

Besides the gravitational force, the electromagnetic force that was generated by the electric current density and self-induced magnetic field was considered in Eq. (2) as body force. The analytical solutions for the vertical and radial components of the current density and the angular component of the magnetic field were expressed as follows:^{20,21}

$$J_z = \frac{I}{2\pi} \int_0^\infty \lambda J_0(\lambda r) \exp\left(-\frac{\lambda^2 r_A^2}{4d}\right) \frac{\sinh[\lambda(c-z)]}{\sinh(\lambda c)} d\lambda, \quad (8)$$

$$J_r = \frac{I}{2\pi} \int_0^\infty \lambda J_1(\lambda r) \exp\left(-\frac{\lambda^2 r_A^2}{4d}\right) \frac{\cosh[\lambda(c-z)]}{\sinh(\lambda c)} d\lambda, \quad (9)$$

$$B_\theta = \frac{\mu_m I}{2\pi} \int_0^\infty J_1(\lambda r) \exp\left(-\frac{\lambda^2 r_A^2}{4d}\right) \frac{\sinh[\lambda(c-z)]}{\sinh(\lambda c)} d\lambda. \quad (10)$$

Here, J_0 is the first kind of Bessel function of zero order, c is the thickness of the work piece, z is the vertical distance from the origin, J_1 is the first kind of Bessel function of the first order, d is the distribution parameter, taken as 0.5, and μ_m is the magnetic permeability of the material.

The plasma drag force, shown in Eq. (11), is exerted on the surface due to impingement of the arc plasma jet flow and it causes an outward flow from the center. To model the plasma drag force, the following analytical solution of the wall shear stress produced by the normal impingement of the jet on the flat surface was used.²²

$$\frac{\tau}{\rho_p \mu_0^2} \text{Re}_0^{1/2} \left(\frac{H}{D}\right)^2 = g_2 \left(\frac{r}{H}\right). \quad (11)$$

Here, τ is the shear stress, ρ_p is the plasma density, u_o is the initial plasma velocity, Re_0 is the Reynolds number, H is the electrode contact nozzle distance from work piece, D is the electrode contact nozzle diameter, r is the radius from the center, and g_2 is the universal function. In the calculation, it is assumed that H and D are the same as the arc length and electrode diameter, respectively. Finally, the buoyancy force, which is a body force, can be modeled by the Boussinesq approximation and is expressed as follows:

$$F_b = \rho g \beta (T - T_0). \quad (12)$$

Here, g is gravity, β is the thermal expansion rate, and T_0 is the reference temperature. This buoyancy force is also induced in laser welding, but it is not discussed here in detail. The GMAW leading and trailing hybrid processes were treated in the same way with only the difference of position.

I. Vaporization model

The application of the laser increases the temperature of the liquid metal up to boiling point, which leads to the vaporization of the metal. The evaporation flux can be calculated using the modified Langmuir equation shown in the below equation²³

$$J_v = \frac{(1 - \beta_R) P_{\text{sat}}(T)}{\sqrt{2\pi MRT}}, \quad (13)$$

where β_R is a recondensation coefficient, $P(\text{sat})$ is vapor induced pressure, M is atomic mass, R is universal gas constant, and T is surface temperature. Recondensation is considered in two steps. In the first step, 18% recondensation is considered in the Langmuir equation based on the reported value for a perfect vacuum.²⁴ The vaporization effectively removes mass and energy from the point of irradiance. If only 18% recondensation is considered, the mass loss due to vaporization is very high as compared to the reported mass loss using a fiber laser.²⁵ Hirano *et al.*²⁶ reported, by means of experimental investigation, a total of 90% recondensation. In partial penetration welding, 72% recondensation was considered for the vapor traveling toward the keyhole exit in such a way that the laser exerts a recondensation flux. This varies linearly from the bottom of the keyhole toward the keyhole exit. In full penetration welding, the recondensation flux is considered to vary from the middle of the work piece toward the keyhole exits at both the top and bottom surfaces.

In the case of full penetration welding, it is also assumed that the vapor plumes present at both the top and bottom surfaces apply energy due to radiation from vapor plumes. The temperature of the vapor plumes is considered to be 6000 K,²⁷ because the work piece material is stainless steel.

IV. MATERIAL PROPERTIES AND BOUNDARY CONDITIONS

Austenitic stainless steel (AISI 316L) plate with a thickness of 10 mm was used in this study. The physical properties

TABLE V. Material properties used in simulation, AISI-316.

Physical properties	Values
Density of liquid metal ρ (kg m^{-3}) 1450 °C	6881
Density of solid metal ρ (kg m^{-3}) 25 °C	7950
Thermal conductivity of liquid k_L ($\text{Wm}^{-1} \text{K}^{-1}$)	28.5
Thermal conductivity of solid k_S ($\text{Wm}^{-1} \text{K}^{-1}$)	19.4
Viscosity μ ($\text{kg m}^{-1} \text{s}^{-1}$) (pure iron)	0.0059
Surface tension γ (N m^{-1}) (1973 K for SS-316)	1.150
Surface tension gradient $d\gamma/dT$ ($\text{N m}^{-1} \text{K}^{-1}$)	-4.3×10^{-4}
Contact angle (deg)	90
Specific heat of solid C_S ($\text{J kg}^{-1} \text{K}^{-1}$)	470
Specific heat of liquid C_L ($\text{J kg}^{-1} \text{K}^{-1}$)	830
Latent heat of fusion h_{SL} (J kg^{-1})	2.70×10^5
Latent heat of vaporization h_V (J kg^{-1})	7.45×10^6
Coefficient of thermal expansion β	1.65×10^{-5}
Liquidus temperature T_L (K)	1723
Solidus temperature T_S (K)	1658
Boiling temperature T_V (K)	3090
Convection heat transfer coefficient h ($\text{kg s}^{-3} \text{K}^{-1}$)	1×10^{-8}
Emissivity ϵ	0.4

of the material and coefficients used in the simulation are shown in Table V. Figure 4 shows the coordinate system and computational domain used in the study. The analytic domain was set as 109.2 mm in length, 26 mm in width, and 20 mm in height including the void regions at both the top and bottom sides for free surface tracking.

The energy on both the top and bottom free surfaces is balanced between the laser heat flux, the heat dissipation by convection and radiation, and the heat loss due to surface evaporation. The energy balance is expressed as follows:

$$\begin{aligned}
 k \frac{\partial T}{\partial \vec{n}} &= q_L + q_A - q_{\text{conv.}} - q_{\text{rad}} - 0.82 * q_{\text{evp}} + q_{\text{recond}} \\
 &= q_L + q_A - h(T - T_0) - \epsilon_r \sigma (T^4 - T_0^4) \\
 &\quad - (q_{\text{evp}} - q_{\text{recond}}), \\
 q_{\text{recond}} &= 0.72 * q_{\text{evp}}, \quad (14)
 \end{aligned}$$

where q_{evp} is the evaporation loss in the previous time step, which is applied as recondensation flux, \vec{n} is the vector normal to the local free surface, h is the convective heat transfer coefficient and T_0 is the ambient temperature. This ambient temperature can be room temperature when considered away from keyhole or metallic vapor plume temperature when

the region is near the keyhole. ϵ_r is the surface radiation emissivity, and σ is the Stefan–Boltzmann constant. The energy balance on the bottom free surface is expressed in a manner similar to Eq. (13), with the only difference being that the laser and arc source are absent at the bottom surface.

For the pressure boundary condition, the following equation was used on the free surface:

$$P = P_R + P_A + \frac{\gamma}{R_c}, \quad (15)$$

where P_R is the recoil pressure on the keyhole wall, P_A is the arc pressure, γ denotes the surface tension coefficient, and R_c denotes the radius of the surface curvature.

V. RESULTS AND DISCUSSION

A. GMA leading hybrid welding

The weld cross-sectional shapes obtained by experiments and simulations are shown in Fig. 5. The results are in fair agreement, and especially, the widening of the weld cross section close to the root was successfully captured in the simulation. Compared to the experimental results, the simulated weld cross section shows lack of weld metal at the weld surface. In addition, wedge-shaped upper portion and root reinforcement are lacking in the simulated weld. The possible reason for the difference was that shielding gas was not considered in the simulations. The use of shielding gas may help to maintain more molten metal on the top surface, which can prevent the formation of undercut.

Figure 6 shows the temperature contours and flow pattern of GMA leading configuration. Figure 6(a) shows the fully developed temperature contours at 1.9 s. It shows two distinct flow recirculations, one on the upper surface and a second on the lower or root surface of the melt pool. A similar type of melt pool was shown for full penetration laser welding by Zhang *et al.*,⁹ and this indicates that the laser was the main source governing the flow pattern in full penetration hybrid welding with GMA leading configuration. It can be seen from the simulation that the molten pool on the top surface was shorter than the molten pool on the root surface. The same pattern persisted as welding proceeds, Fig. 6(b). The freezing of the molten pool first started at the top surface, and the root surface was the last to solidify, as shown in Fig. 6(c). In partial penetration laser welding, the molten pool was only observed at top surface of weld pool because this was the

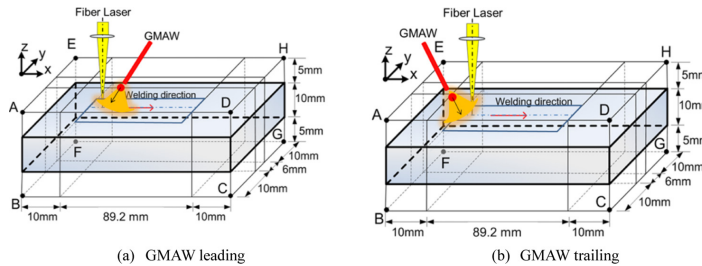


FIG. 4. Simulation domain with (a) GMAW leading and (b) GMAW trailing configurations.

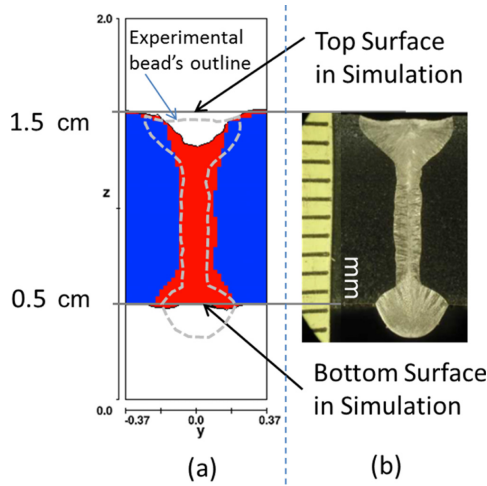


FIG. 5. GMAW leading, comparison of simulated (a) and experimental (b) weld cross sections. In (a) units are in centimeters.

only opening for molten metal at the bottom of the keyhole to gush out. However, in the full penetration welding, the molten metal inside the keyhole had the option to gush out both from the top surface and the root surface. The flow of molten pool toward the bottom side was more probable because the molten pool was attracted toward the bottom by the forces of gravity, while this gravity force opposes the flow of molten pool toward the top surface. Another reason for higher amount of melt pool at root surface is that most amount of fiber laser was absorbed by the bottom part of the keyhole as shown by Sohail *et al.*,¹² which will generate higher recoil pressure at the bottom half of the keyhole. In GMA only full

penetration welding, the molten pool length at the bottom was much smaller, but in laser full penetration welding, it was shown experimentally by Zhang *et al.*⁹ that the molten pool at the root surface was longer as compared to the molten pool at the top surface.

In the longitudinal section, Fig. 7(a), and transversal cross section, Fig. 7(b), fluctuations of chromium concentration can be seen in the weld. The results show enhanced chromium content close to surface of the weld, i.e., the mixing of Cr in weight per cent is inhomogeneous and has a higher concentration in the upper part of the melt pool. This type of mixing characteristic was also found in the study of Cho *et al.*⁶ in partial penetration hybrid welding with GMA leading configuration.

Figures 8(a)–8(d) show the mixing profiles of the experimental weld, obtained through an energy dispersive spectroscopy (EDS)-line scan using Cr as a trace element. Mixing was designated to be 0%, if the concentration of Cr was in the level of the base metal (17.6 wt. % Cr) and 100% if the concentration of Cr was in the level of filler wire (22.9 wt. % Cr). Other values were obtained by linear interpolation based on below equation

$$\text{Mixing} = \frac{(\text{wt. \% Cr} - 17.6)}{(22.9 - 17.6)} * 100. \quad (16)$$

The general trend shows higher mixing in the upper part of the weld, as illustrated in the experimental results Figs. 8(a) and 8(b). A trend of lesser mixing was found in the lower part, as shown in Figs. 8(c) and 8(d). This is also correspondingly good with the earlier results of Karhu *et al.*⁵ It is to be noted that these concentrations were captured at particular transversal cross section and may show different values when scanned at different locations. In order to allow a comparison with the line scans obtained by EDS of experimental weld cross sections, four line scans were extracted from simulated weld cross sections. The lines were drawn at z-locations of 1.37, 1.11, 0.87, and 0.63 cm. Figures 8(e)–8(h) show the corresponding simulated mixing profiles on the same locations of Figs. 8(a)–8(d), respectively.

The mixing profiles, Figs. 8(e) and 8(f), show that the scans at higher locations evidence more mixing as compared to scans at the lower part of the weld, Figs. 8(g) and 8(h). The overall trend of higher mixing in the upper part of the weld cross section was the same in both the experimental and simulated scans but the values were not exactly the same as compared to mixing profiles obtained experimentally. This can be explained by the fact that the mixing profiles can vary from location to location as shown in the simulated mixing profiles, Fig. 7(a), but generally, the trend of having higher Cr concentration would remain the same. Mixing profiles obtained by simulation showed a fair agreement with the experimental values, although the values were a little different from those obtained by the experimental means.

In order to study the melt pool in detail, simulated particles were introduced having properties similar to that of tungsten (W). Five sets of equally spaced particles were placed in five columns and five rows as shown in Fig. 9. The simulated trace of particles helps in understanding the

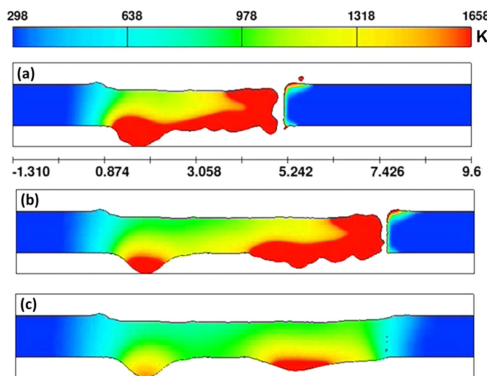


FIG. 6. Simulated longitudinal cuts of laser hybrid welding with GMAW leading. Welding direction from left to right. Flow patterns and temperature contours of the simulated weld in the same location at different times. (a) 1.9 s after switch-on the laser beam, (b) 3 s (at the time of switch-off the laser beam), and (c) 4.3 s (1.3 s after switch-off the laser beam). The colors describe temperature in Kelvins as shown in ruler at the top.

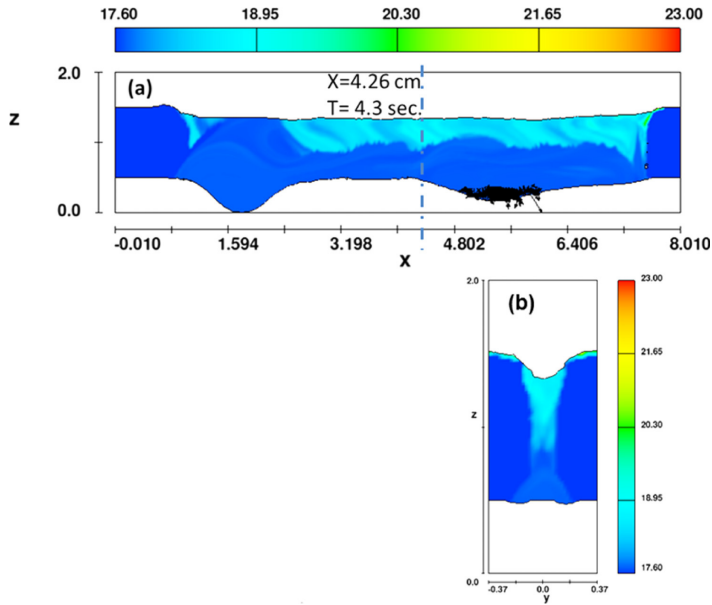


FIG. 7. Chromium content profiles of laser hybrid welding with GMAW leading (a) longitudinal section of fusion zone and (b) chromium content profile of cross section at location $X = 4.26$ cm at 4.3 s. Horizontal and vertical axes are dimensions in centimeters. The colors mark chromium content in wt. %.

mixing behavior of the melt pool. Figure 10 shows the trace of uppermost particle layer, numbered from 21 to 25. Particle 21, which first comes into contact with the laser beam, is mostly circulating in the upper portion and quickly gets

trapped by the upcoming freezing front. This is due to the fact that at the start of welding the length of the molten pool is short in both upper and lower parts. Particles 22, 23, and 24 were able to reach the bottom of the melt pool. Once the

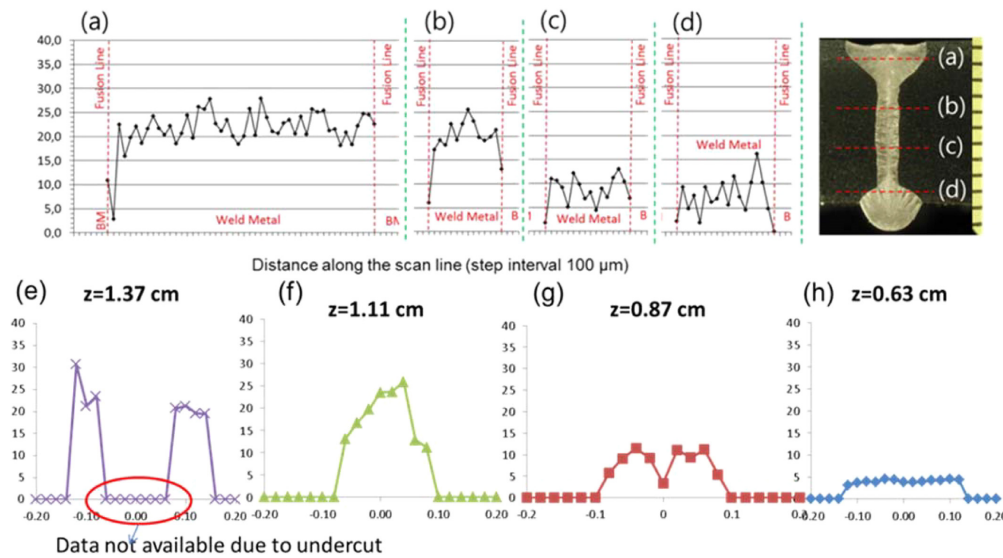


FIG. 8. Experimental (a)–(d) and simulation (e)–(h) of mixing profiles. Vertical axis shows mixing values as per cent according to Eq. (16). In (e)–(h) the place of location (z -value) is referring to Fig. 5(a).

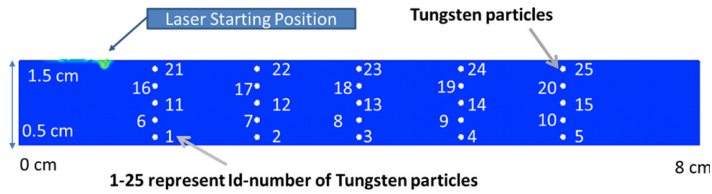


FIG. 9. Locations of 25 tungsten particles introduced.

particles 22, 23, and 24 reach the bottom of melt pool they are unable to return back to the upper part of the molten pool. Therefore, they keep on traveling in the bottom surface molten pool. Figure 11 shows the track of the lowest layer particles 1–5. This shows that none of the particles is able to reach the upper part of the molten pool. The two sets of particle traces indicate that the major flow of particles introduced in the upper layer is toward the bottom surface. The particles near the bottom surface keep on circulating in the lower half of the molten pool. This induces a longer molten pool at the bottom surface and less concentration of Cr in the bottom half of the weld.

B. GMA trailing hybrid welding

GMA trailing simulations were also carried out and a comparison of experimental and simulated weld cross sections is presented in Fig. 12. The shape of cross sections are quite different. The experimental weld shows wide, wedge-like surface, while the root is wider in the simulated cross section. The sagging of melt appeared as an undercut in the simulated bead. However, this undercut was not found in the experimental results. The difference might be the result of neglecting the shielding gas in the simulations. The shielding gas could induce shear stress and react with the molten metal. This probably kept the molten metal in place on the top surface.

Figure 13 shows that the temperature contours and flow pattern of the GMA trailing configuration were quite different from the case of GMA leading simulations. In GMA

leading case, Fig. 6(a), the solidification front proceeds as a peninsula to the melt, sectioning the melt in the upper and lower parts. On the contrary, this behavior is not seen in the GMA trailing case, Fig. 13(a). The above mentioned solidification peninsula may obstruct the circulation of the melt flow between the weld surface and root, which in turn may reduce the mixing of weld metal.

The temperature contours of GMA trailing configuration in Fig. 13 show that the GMA droplet is directly impinging on the molten pool and the keyhole formed by the laser beam. On the other hand, in GMA leading configuration, shown in Fig. 6(a), GMA droplet is impinging on the solid surface of the work piece and causing a preheating of the work piece. This means that in the case of GMA leading configuration, some part of the GMA welding heat was consumed in preheating the work piece while in GMA trailing, most of the GMA heat source energy is supplied to the already molten weld pool. The results were consistent until the end of welding.

The complex phenomenon explained above seems to have also altered the mixing of Cr. This can be seen in Fig. 14, where the mixing was comparatively uniform in the GMA-trailing hybrid welding as compared to the GMA-leading hybrid welding. The incoming metal directly mixed with the molten pool that was created by laser beam and the complex flow structure allowed the Cr to mix in both the upper and lower melt pool.

Figures 15(a)–15(d) show the mixing profile in per cent converged from the results of the EDS-line scans in the GMA-trailing hybrid welding. The corresponding locations on the weld cross section are shown in Fig. 15(e). The mixing

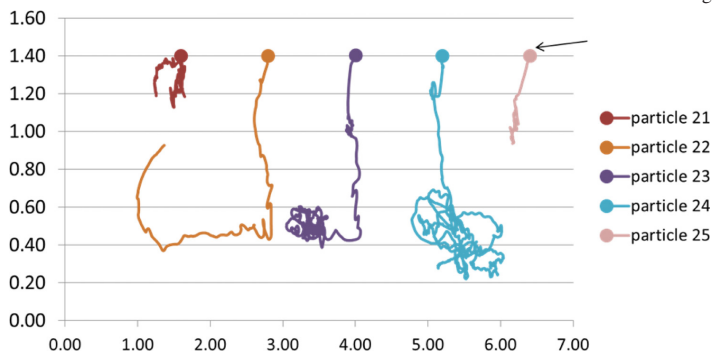


FIG. 10. Traces of particles starting from the uppermost layer. x-axis is travel distance in cm. y-axis is thickness of plate in cm. The lower surface of the plate is at 0.5 cm and upper surface at 1.5 cm.

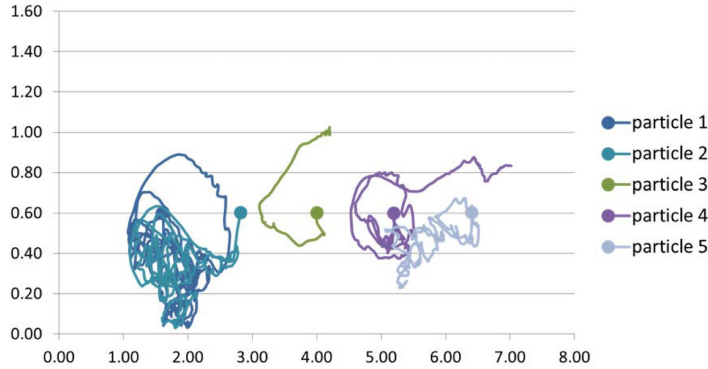


FIG. 11. Traces of particle starting from the lowest layer. *x*-axis is travel distance in cm. *y*-axis is thickness of plate in cm. The lower surface of the plate is at 0.5 cm and upper surface at 1.5 cm.

is higher in the upper scans, Figs. 15(a) and 15(b), but the variation was much higher than the corresponding line scans for the GMA-leading hybrid welding, shown in Figs. 8(a) and 8(b). In the GMA trailing configuration, considerable points show mixing below 15% which were not found in the GMA leading configuration. The mixing profile at the bottom shows a very slight decrease in mixing but some points show a very high amount of mixing, up to 30% in Fig. 15(c) and 21% in Fig. 15(d). This indicates that a more enhanced mixing, in general, was achieved as compared to mixing in the GMA-leading cases in Figs. 8(c) and 8(d).

Figures 15(a)–15(d) show the mixing profiles of the experimental weld obtained through an EDS-line scan using Cr as a trace element in locations shown in the weld cross section in Fig. 15(e). Mixing was designated according to Eq. (16) in the same way as explained earlier in the discussion of GMAW leading case.

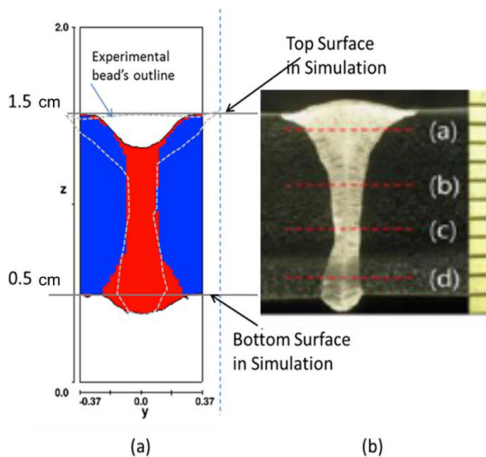


FIG. 12. GMAW trailing, comparison of simulated and experimental weld cross sections.

The line scans of calculated mixing profiles obtained by simulations are shown in Figs. 15(f)–15(j). They correspond to the locations of experimental lines in Figs. 15(a)–15(d), respectively. The line scan of Fig. 15(f) shows zero mixing because the cells were empty on those locations and the data was not available.

The other locations Figs. 15(g)–15(i) show a uniform mixing profile. The difference of the mixing profile levels between close to surface and close to root is quite small. This behavior of uniform mixing was absent in the case of simulated line scans of GMA leading configuration shown in Figs. 8(f)–8(g).

In order to study the flow behavior, tungsten particles were also introduced in the case of GMA trailing configuration as they were introduced in the GMA leading configuration, Fig. 9. It can be seen that three of five particles were

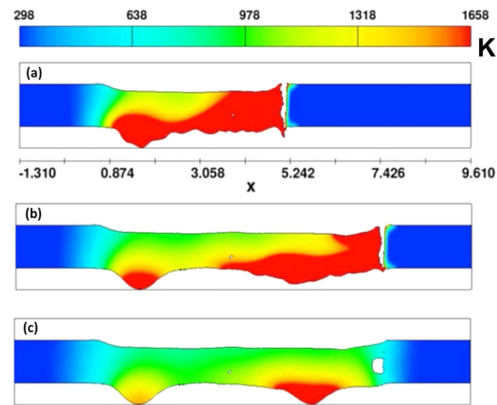


FIG. 13. Simulated longitudinal cuts of laser hybrid welding with GMA trailing. Welding direction from left to right. Flow patterns and temperature contours of the simulated weld in the same location at different times. (a) 1.9 s after switch-on the laser beam, (b) 3 s (at the time of switch-off the laser beam) and (c) 4.3 s (1.3 s after switch-off the laser beam). The colors describe temperature in Kelvins as shown in ruler at the top.

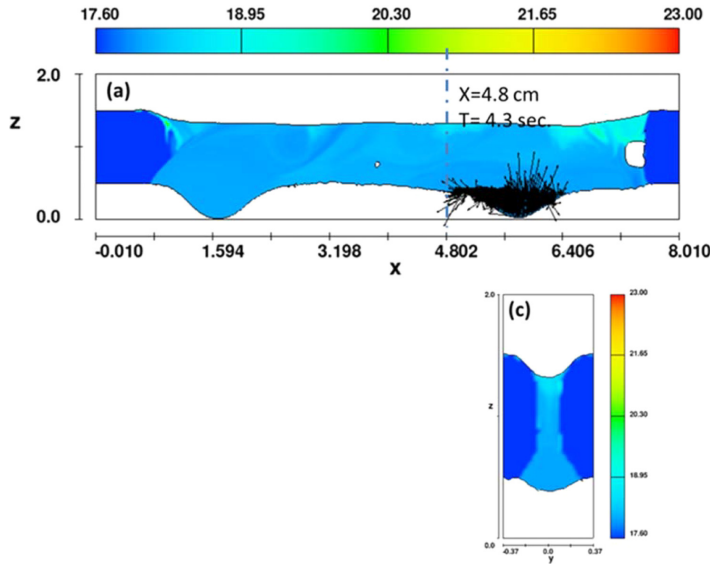
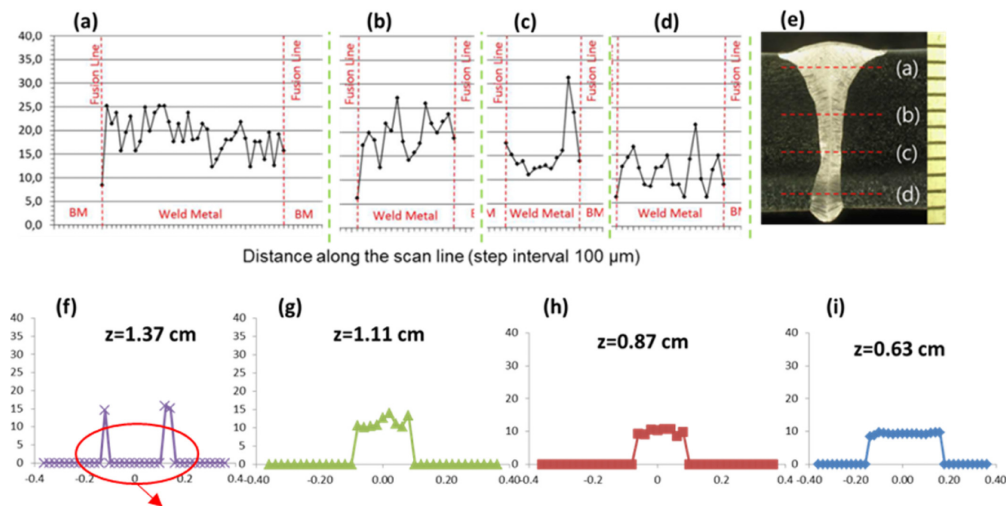


FIG. 14. Chromium content profiles of laser hybrid welding with GMAW trailing (a) longitudinal section of fusion zone and (b) chromium content profile of cross section in location $X = 4.8$ cm at 4.3 s. Horizontal and vertical axes are dimensions in centimeters.

able to recirculate throughout the thickness of the work piece, Fig. 16. The particles 21, 23, and 24, were able to reach the bottom part of the melt pool and return to the upper part of the melt pool, where they were initially placed. This type of flow recirculation was absent in the case of GMA

leading configuration shown in Fig. 10. Particle 1 shown in Fig. 17 was able to reach the upper part of the melt pool, although it was initially introduced in bottom part of the melt pool. In the GMA leading configuration, not a single particle was able to reach the upper melt pool when the



Data not available due to undercut

FIG. 15. Experimental (a)–(d) and simulation (f)–(i) of mixing profiles of laser hybrid welding with GMAW trailing. Vertical axis is mixing as per cent according to Eq. (16). In (f)–(i) the place of location (z -value) is referring to Fig. 12(a).

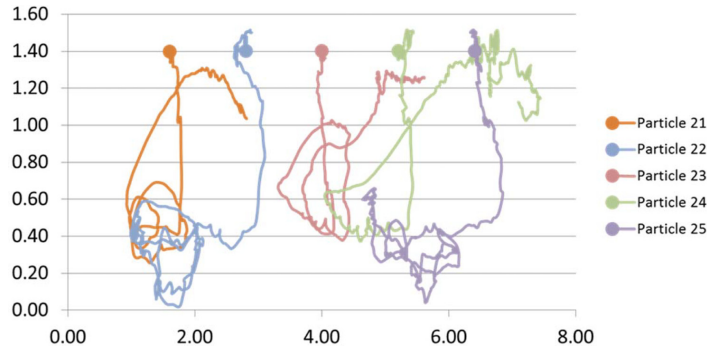


FIG. 16. Traces of particles starting from the uppermost layer. x -axis is travel distance in cm. y -axis is thickness of plate in cm. The lower surface of the plate is at 0.5 cm and upper surface at 1.5 cm (see Fig. 9).

particles were introduced on the same locations, Fig. 11. This indicates that in the GMA trailing configuration, the flow recirculation is more pronounced, and therefore, mixing is more efficient. This emphasises the recirculation of melt at the root part, which will definitely increase the mixing the bottom part of the weld. The absence of such recirculation in the GMA leading configuration was the main reason for having low mixing of melt at the bottom of the weld.

C. Comparison of velocity field in GMAW leading and trailing

Figure 18 presents a comparison of velocity field in the GMA leading and GMA trailing configurations. It was found that higher velocities were observed near the interface surface of the keyhole and melt pool. In both GMA leading and trailing cases, the velocity magnitudes were higher when the keyhole was closed. It is suggested that during the GMA trailing configuration there was a higher tendency of incoming droplet to force the keyhole to close, while the incoming laser applies the force in the opposite direction; therefore, more mixing might be due to these opposite forces. Higher velocities were also observed near the external surface of molten pool at root side, which might be due to the fact that the bottom surface is nearer to the closed keyhole; therefore, it would be easier for the high velocity molten pool to reach the bottom surface in contrast with the top surface.

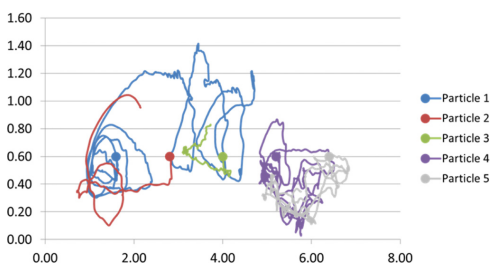


FIG. 17. Traces of particle starting from the lowest layer. x -axis is travel distance in cm. y -axis is thickness of plate in cm. The lower surface of the plate is at 0.5 cm and upper surface at 1.5 cm (see Fig. 9).

D. Comparison of temperature field in GMAW leading and trailing

A comparison of the temperature field of GMA trailing and leading is presented in Fig. 19. In both cases, a longer molten pool was observed at the root surface, Figs. 19(a), 19(b), 19(c), and 19(f) present the temperatures from room temperature to solidus temperature to indicate the total molten pool. Temperatures above solidus to boiling temperature is presented in Figs. 19(c), 19(d), 19(g), and 19(h), which indicated that higher temperatures were observed near the molten pool in touch with the keyhole walls. In both the initial stages of welding and after somewhat developed stage, the molten pool at the root surface is indicating higher temperature. This trend has some similarity with the trend of velocity magnitude presented in Fig. 18.

VI. CONCLUSION

Laser-GMA hybrid welding in full penetration configuration of 10 mm thickness austenitic stainless steel was studied by simulation and compared to experimental results. The effect of leading and trailing torch configuration on mixing and fluid behavior of weld metal was studied.

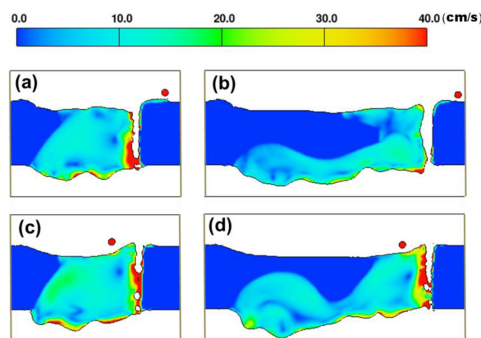


FIG. 18. Velocity fields of (a) GMA leading at 0.7 s, (b) GMA leading at 1.4 s, (c) GMA trailing at 0.7 s and (d) GMA trailing at 1.4 s.

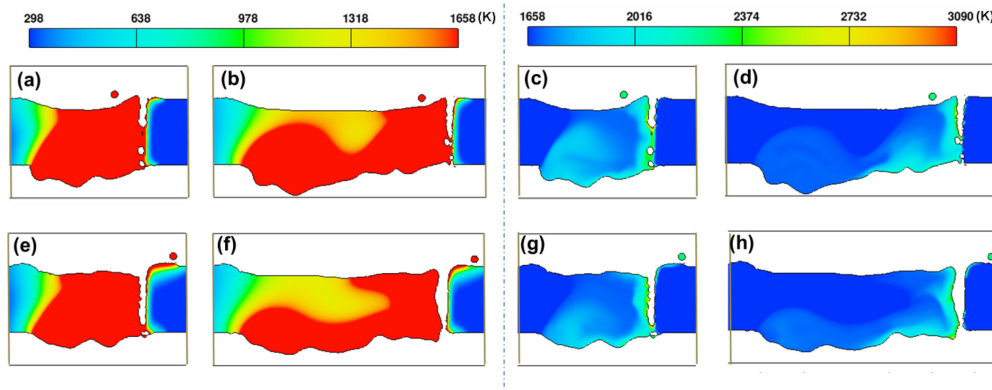


FIG. 19. Temperature field of GMA trailing, (a) below 1658 K at 0.7 s, (b) 1.4 s, (c) above 1658 K, 0.7 s, (d) 1.4 s, GMA leading, (e) below 1658 K at 0.7 s, (f) 1.4 s, (g) above 1658 K, 0.7 s, and (h) 1.4 s.

According to the simulation results, two recirculating flows were found, one on the top surface and another on the root surface. The molten pool is longer in the bottom surface as compared to the upper surface. The temperature contours and flow pattern of the GMA trailing configuration were quite different from the case of the GMA leading simulations. In the GMA leading case, the solidification front proceeds as a peninsula in the melt. It sections the upper and lower parts of the melt pool. On the contrary, this behavior was not seen in the GMA trailing case. The above mentioned solidification peninsula may obstruct the circulation of the melt flow between the weld surface and root, which in turn may reduce the mixing of weld metal.

Five sets of tungsten particles were introduced in simulation to study the flow behavior, which revealed that in the GMA leading configuration, once the particles reach the bottom recirculation they were unable to reach the upper recirculation. In the GMA trailing configuration, the particles, which were initially introduced in the surface part of the weld, were able to reach the bottom recirculation and then return back toward the upper recirculation. This phenomenon helps in the mixing of the melt in GMA trailing.

In the GMA trailing configuration, the flow recirculation is more pronounced, and therefore, mixing is more efficient than in the GMA leading case. This emphasizes the recirculation of melt at the root part, which will definitely increase the mixing in the root part of the weld. The absence of such recirculation in the GMA leading configuration was the main reason for having low mixing at the bottom part of the weld.

ACKNOWLEDGMENTS

The authors gratefully acknowledge the support of the Brain Korea 21, NRF of Korea, and the Finnish Distinguished Professor Programme of TEKES, Finland, to carry out this research.

- ¹W. Zhang, X. Hua, W. Liao, F. Li, and M. Wang, "Study of metal transfer in Co₂ Laser+Gmaw-P hybrid welding using argon-helium mixtures," *Opt. Laser Technol.* **56**, 158–166 (2014).
- ²W. Zhang, X. Hua, W. Liao, F. Li, and M. Wang, "The effect of the welding direction on the plasma and metal transfer behavior of Co₂ Laser+Gmaw-P hybrid welding processes," *Opt. Lasers Eng.* **58**, 102–108 (2014).
- ³L. Zhao, T. Sugino, G. Arakane, and S. Tsukamoto, "Influence of welding parameters on distribution of wire feeding elements in Co₂ laser Gma hybrid welding," *Sci. Technol. Weld. Joining* **14**, 457–467 (2009).
- ⁴H. L. Wei, H. Li, L. J. Yang, Y. Gao, and X. P. Ding, "Arc characteristics and metal transfer process of hybrid laser double Gma welding," *Int. J. Adv. Manuf. Technol.* **77**, 1019–1028 (2014).
- ⁵M. Karhu, V. Kujanpää, A. Gumenyuk, and M. Lammers, "Study of filler metal mixing and its implication on weld homogeneity of laser-hybrid and laser cold-wire welded thick austenitic stainless steel joints," in *32nd International Congress on Applications of Lasers and Electro-Optics, ICALOE2013* (2013), pp. 252–261.
- ⁶W.-I. Cho, S.-J. Na, M.-H. Cho, and J.-S. Lee, "Numerical study of alloying element distribution in Co₂ laser-Gma hybrid welding," *Comput. Mater. Sci.* **49**, 792–800 (2010).
- ⁷W.-I. Cho, S.-J. Na, C. Thomy, and F. Vollertsen, "Numerical simulation of molten pool dynamics in high power disk laser welding," *J. Mater. Process. Technol.* **212**, 262–275 (2012).
- ⁸D. W. Cho, S. J. Na, M. H. Cho, and J. S. Lee, "A study on V-groove Gmaw for various welding positions," *J. Mater. Process. Technol.* **213**, 1640–1652 (2013).
- ⁹L. J. Zhang, J. X. Zhang, A. Gumenyuk, M. Rethmeier, and S. J. Na, "Numerical simulation of full penetration laser welding of thick steel plate with high power high brightness laser," *J. Mater. Process. Technol.* **214**, 1710–1720 (2014).
- ¹⁰D.-W. Cho, W.-I. Cho, and S.-J. Na, "Modeling and simulation of arc: Laser and hybrid welding process," *J. Manuf. Processes* **16**, 26–55 (2014).
- ¹¹M. Sohail, S.-W. Han, S.-J. Na, A. Gumenyuk, and M. Rethmeier, "Characteristics of weld pool behavior in laser welding with various power inputs," *Weld. World* **58**, 269–277 (2014).
- ¹²M. Sohail, S.-W. Han, S.-J. Na, A. Gumenyuk, and M. Rethmeier, "Numerical investigation of energy input characteristics for high-power fiber laser welding at different positions," *Int. J. Adv. Manuf. Technol.* **80**, 931–946 (2015).
- ¹³V. V. Avilov, A. Gumenyuk, M. Lammers, and M. Rethmeier, "Pa position full penetration high power laser beam welding of up to 30 Mm thick Almg₃ plates using electromagnetic weld pool support," *Sci. Technol. Weld. Joining* **17**, 128–133 (2012).
- ¹⁴M. Bachmann, V. Avilov, A. Gumenyuk, and M. Rethmeier, "Experimental and numerical investigation of an electromagnetic weld pool support system for high power laser beam welding of austenitic stainless steel," *J. Mater. Process. Technol.* **214**, 578–591 (2014).

- ¹⁵M. Zhang, G. Chen, Y. Zhou, and S. Liao, "Optimization of deep penetration laser welding of thick stainless steel with a 10 kW fiber laser," *Mater. Des.* **53**, 568–576 (2014).
- ¹⁶V. R. Voller and C. Prakash, "A fixed grid numerical modelling methodology for convection-diffusion mushy region phase-change problems," *Int. J. Heat Mass Transfer* **30**, 1709–1719 (1987).
- ¹⁷J. N. DuPont and A. R. Marder, "Thermal efficiency of arc welding processes," *Weld. J.* **74**, 406s–416s (1995).
- ¹⁸D.-W. Cho, S.-J. Na, M.-H. Cho, and J.-S. Lee, "Simulations of weld pool dynamics in V-groove gta and gma welding," *Weld. World* **57**, 223–233 (2013).
- ¹⁹Z. Cao, Z. Yang, and X. L. Chen, "Three-dimensional simulation of transient gma weld pool with free surface," *Weld. J.* **85**, 169s–176s (2004).
- ²⁰K. Sindo and D. K. Sun, "Fluid flow and weld penetration in stationary arc welds," *Metall. Trans.* **16A**, 203–213 (1985).
- ²¹A. Kumar and T. DebRoy, "Calculation of three-dimensional electromagnetic force field during arc welding," *J. Appl. Phys.* **94**, 1267–1277 (2003).
- ²²D. J. Phares, G. T. Smedley, and R. C. Flagan, "The wall shear stress produced by the normal impingement of a jet on a flat surface," *J. Fluid Mech.* **418**, 351–375 (2000).
- ²³J. P. Bellot, M. Ritchie, H. Duval, A. Mitchell, and D. Ablitzer, "Evaporation of Fe and Cr from induction-stirred austenitic stainless steel. Influence of the inert gas pressure," *ISIJ Int.* **41**, 696–705 (2001).
- ²⁴M. Allmen and A. Blatte, *Laser-Beam Interactions with Materials*, 2nd ed. (Springer, Berlin, Germany, 1995).
- ²⁵Y. Kawahito, N. Matsumoto, Y. Abe, and S. Katayama, "Laser absorption characteristics in high-power fibre laser welding of stainless steel," *Weld. Int.* **27**, 129–135 (2013).
- ²⁶K. Hirano, R. Fabbro, and M. Muller, "Experimental determination of temperature threshold for melt surface deformation during laser interaction on iron at atmospheric pressure," *J. Phys. D: Appl. Phys.* **44**, 435402 (2011).
- ²⁷Y. Kawahito, K. Kinoshita, N. Matsumoto, M. Mizutani, and S. Katayama, "Effect of weakly ionised plasma on penetration of stainless steel weld produced with ultrahigh power density fibre laser," *Sci. Technol. Weld. Joining* **13**, 749–753 (2008).

Publication IV

Karhu, M., Kujanpää, V., Eskelinen, H. and Salminen, A.

**Filler metal mixing behaviour of 10 mm thick stainless steel butt-joint welds
produced with laser-arc hybrid and laser cold-wire processes**

Reprinted with permission from

Applied Sciences

Vol. 9, Article number 1685, 2019

© 2019, MDPI

Article

Filler Metal Mixing Behaviour of 10 mm Thick Stainless Steel Butt-Joint Welds Produced with Laser-Arc Hybrid and Laser Cold-Wire Processes

Miikka Karhu ^{1,*}, Veli Kujanpää ¹, Harri Eskelinen ¹ and Antti Salminen ²

¹ Laboratory of Welding Technology, LUT University, Yliopistonkatu 34, 53850 Lappeenranta, Finland; veli.kujanpaa@lut.fi (V.K.); harri.eskelinen@lut.fi (H.E.)

² Laboratory of Laser Materials Processing, LUT University, Yliopistonkatu 34, 53850 Lappeenranta, Finland; antti.salminen@lut.fi

* Correspondence: miikka.karhu@lut.fi; Tel.: +358-50-4354-587

Received: 21 March 2019; Accepted: 19 April 2019; Published: 24 April 2019



Abstract: In thick section laser welding, filler metal addition is usually required to improve joint fit-up tolerances or to control the chemical composition of the weld metal. With deep and narrow welds produced using an over-alloyed filler metal, it may be challenging to ensure that the filler metal and its elements are homogeneously mixed and evenly distributed throughout the fusion zone. Inhomogeneous filler metal mixing can cause unfavourable changes to weld metal chemistry and microstructure. Filler metal mixing behaviour in laser-arc hybrid and laser cold-wire welding is studied in this work. Welding tests were conducted on 10 mm thick butt-welded joints of AISI 316L austenitic stainless steel. An overmatching type 2205 duplex stainless steel filler wire was used to obtain a composition contrast between the base metal and filler metal. Energy dispersive spectroscopy (EDS) with chromium as the trace element was used for element mapping and stepwise characterization of the weld cross-section samples. Optical metallography was used to observe possible inhomogeneous filler metal mixing behaviour like local acute changes in macro- and microstructural features. The results showed a clear difference in filler metal mixing between the weld surface part (upper half) of the weld and the weld root part (lower half) in 10 mm thick welded cross-sections for closed root gap of I-groove welds or when the gap was only 0.4 mm. In narrow I-groove preparations, inhomogeneous mixing phenomena were more pronounced in laser cold-wire welds than in laser-arc hybrid welds. In both welding processes, a combination of trailing wire feeding and the use of a wider groove enabled filler metal to be introduced deeper into the bottom of the groove and improved mixing in the root portion of the welds.

Keywords: filler metal mixing; laser-arc hybrid welding; laser cold-wire welding; thick sections; austenitic stainless steel

1. Introduction

The utilization of modern high-power laser systems in laser-arc hybrid welding and laser welding with filler wire processes can provide new tools and techniques for efficiency improvement in heavy-section welding. For example, efficiency enhancement via reduced manufacturing time can be achieved if thicker sections can be welded using deep single-pass welding. Single-pass welding tends to result in less weld distortion and thus less time-consuming post-weld finishing is required [1–5]. When considering welding of thick section joints an autogenous laser beam welding is not always practically feasible and that is why filler metal addition to the welding process is needed. Filler metal can be introduced to the laser process for example, via an arc (laser-arc hybrid) as a molten form or using a cold-wire [6–9] or pre-heated wire feeding [10,11]. Also pre-set filler metal foil inserts [12,13]

inside the joint has been used. The need for the use of filler addition can be associated with the joint fit-up tolerance requirements of the welded parts or for example, metallurgical and mechanical properties required for the produced weldments. Although offering clear benefits, the use of filler material in thick section laser or laser-arc hybrid welding applications faces a number of challenges. Results from previous investigations have indicated that in thick section joints with closed or narrow square butt configurations, the filler metal proportion in the weld metal is mainly limited to the surface part of the weld cross-section and filler metal mixing in the root area of the weld metal is minor or negligible [14–17]. Depending on the application and the combination of base metal and filler metal used, inhomogeneous filler metal mixing can have an adverse effect on weld metal microstructural homogeneity and weld metal phases. In turn, the non-optimal microstructure can cause, for example, loss of corrosion resistance, reduction in ductility properties or enhanced susceptibility to weld solidification cracking [13,18–21].

The aim of this study is to investigate filler metal mixing behaviour in 10 mm thick joints of austenitic stainless steel in single-pass laser-arc hybrid and laser cold-wire welding processes. The objective was to examine the effect of groove geometry and filler wire feeding orientation on filler metal mixing in terms of the intensity and homogeneity of mixing throughout the weld cross-section from the weld surface to the root. The experimental work aimed to gain practical knowledge and provide answers to the following research questions: Can filler metal mixing at the root portion of the weld be enhanced by widening the root gap of an I-groove weld or by using a suitable V-groove? Can any difference be found between the results of using leading or trailing wire feeding, that is, when the filler wire is introduced to the melt pool in front of or behind the laser beam with respect to the welding direction? Is there any noticeable difference in filler metal mixing behaviour between laser-arc hybrid and laser cold-wire welding?

2. Materials and Methods

The base material used in the experiments was an austenitic stainless steel grade, AISI 316L, with plate thickness of 10 mm. The test specimens for the welding tests were rectangular pieces 150 mm in width and 300 mm in length. Preparation of the fusion faces of the joints was done by machining. Both I- and V-grooves were prepared for the experiments. The test specimens were tack-welded at both ends and in the centre to achieve the required butt joint configurations. In welds with I-grooves, both closed (root gap = 0 mm) and open square (root gap = 0.4 mm and 0.8 mm) configurations were used, Figure 1a,b. In tests with a V-groove, the configuration was 10-degree groove angle, closed gap and without root face, Figure 1c. The nominal cross-sectional groove area for the 0.4 mm and 0.8 mm open square configurations and the V-groove configuration is 4 mm², 8 mm² and 8.6 mm², respectively. The filler material used was a type 2205 duplex stainless steel filler wire (Ø 1.0 mm) that has an over-matched chemical composition compared to the base material. The exact chemical composition of the base and filler material is given in Table 1.

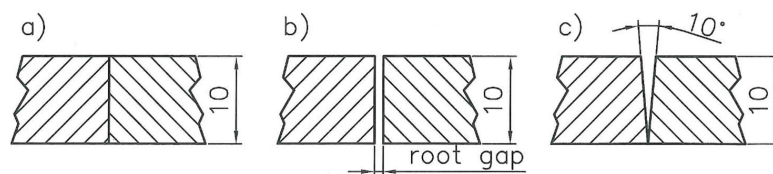


Figure 1. Butt-joint configurations used in the experiments: (a) Closed square (root gap = 0 mm); (b) open square (root gap = 0.4 mm and 0.8 mm); and (c) V-groove with 10-degree groove angle, closed gap and without root face.

Table 1. Chemical composition of the base (AISI 316L) and filler (2205 duplex) material.

Element Weight-%	C	Si	Mn	P	S	Cr	Ni	Mo	N	Cu	Ti + Ta
AISI 316L	0.024	0.37	1.70	0.020	0.0002	17.6	12.3	2.43	0.07	0.01	<0.01
2205	0.010	0.36	1.60	0.017	0.0001	22.9	8.7	3.20	0.147	0.08	-

The welding equipment used in the laser-arc hybrid and laser cold-wire welding experiments was an IPG 10 kW YLS-10000 (IPG Inc., New York, NY, USA) fibre laser and a Kemppi Pro 5200 (Kemppi Oy, Lahti, Finland) gas metal arc welding (GMAW) machine. In the laser cold-wire tests, the filler wire was guided through the same GMAW torch as used in the laser-arc hybrid experiments. A grounding cable shoe was disconnected from the fastening table to enable the use of cold-wire welding. Beam delivery from the laser source to the welding station and welding head was with a process fibre of 200 μm core diameter. The welding head was a laser welding head-unit from Kugler GmbH with copper metal optics and an adjustable GMAW torch unit. The optical system of the Kugler laser welding head consisted of 120 mm collimation and 300 mm focusing lenses. The optical set-up can provide a focal spot diameter of 500 μm . The laser system enables a beam parameter product of 7.1 mm \times mrad and a Rayleigh length of 13.86 mm. A custom-built gantry-based X/Y/Z- linear movement station was used to execute the required welding movements. Figure 2 shows the welding head set-up attached to the linear movement station.

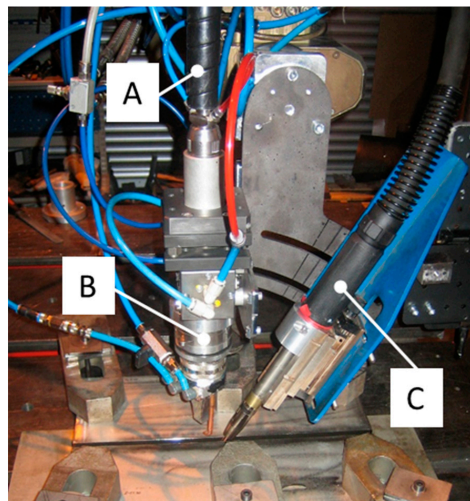


Figure 2. Welding head set-up used in the laser-arc hybrid and laser cold-wire experiments. (A) process fibre with connector; (B) laser welding head-unit; (C) adjustable gas metal arc welding (GMAW) torch unit.

Experiments consisted of sets of single-pass test welds made on 10 mm thick butt-joints in flat position using laser-gas metal arc (GMA) hybrid welding and laser cold-wire welding. The shielding gas used is commercially available mixture for welding of stainless steels. It contained a mixture of Ar + 2% CO₂ + 30% He and was supplied via an arc torch with the flow rate of 24 L/min. Pulsed current GMAW was deployed in the laser-arc hybrid experiments. Table 2 presents the welding parameters used.

Table 2. Welding parameters in the laser-arc hybrid and laser cold-wire welding experiments.

Description	Laser-Arc Hybrid Process	Laser Cold-Wire Process
Laser power, P_L	10 kW	10 kW
Welding speed, V_w	For groove types B2 and B3 = 1.3 m/min; for groove type B4 = 1.6 m/min	For groove types B1, B2 and B3 = 1.1 m/min; for groove type B4 = 1.3 m/min
Filler wire feeding rate, V_f	For groove type B2 = 5 m/min; for groove type B3 = 11.5 m/min; for groove type B4 = 15 m/min	For groove types B1 and B2 = 6 m/min; for groove type B3 = 9.5 m/min; for groove type B4 = 15 m/min
Average current and voltage	5 m/min => 96A/24V; 11.5 m/min => 215A/31V; 15 m/min => 228A/31V	-
Torch/wire feeding angle, α	65 degree	58 degree
Wire stick out, L_w	15 mm	17 mm
Horizontal distance between laser spot and arc or wire tip, D_{LA} or D_{LW}	3.5 mm	0 mm
Focal point position, F	For groove types B2 and B4 => F = -4 mm (equals laser spot diameter \varnothing 0.8 mm); for groove type B3 => F = +20 mm (equals laser spot diameter \varnothing 1.2 mm)	For groove types B1, B2 and B4 => F = -4 (equals laser spot diameter \varnothing 0.8 mm); for groove type B3 => F = +20 mm (equals laser spot diameter \varnothing 1.2 mm)

The objective of the experiments was to gain information about filler metal mixing behaviour in laser-arc hybrid and laser cold-wire welding of thick sections by comparing the effects of wire feeding orientation and groove cross-section. The welding tests included the following parameter combinations (A and B):

(A) Wire feeding orientation with respect to the laser beam and welding direction

- A1 = leading wire feeding
- A2 = trailing wire feeding

(B) Groove type / width of root gap

- B1 = I-groove, closed gap = 0 mm
- B2 = I-groove, open gap = 0.4 mm
- B3 = I-groove, open gap = 0.8 mm
- B4 = V-groove with 10 degree groove angle, closed gap = 0 mm

Welding speed and filler wire feeding rate were determined based on the four different groove cross-sections used. Filler wire feeding rates have to match the volume of the used groove type. Welding speed values were set to balance full joint penetration and good root side formation.

Table 3 summarizes the welding parameter combinations used in the laser-arc hybrid and laser cold-wire welding tests. Figure 3 presents schematic descriptions of the configuration set-up of the laser beam and filler wire arrangement and alignment in the laser-arc hybrid and laser cold-wire welding experiments. The horizontal distance between the laser beam spot and arc (D_{LA}) or wire tip (D_{LW}) was 3.5 mm for the laser-arc hybrid process and zero for the laser cold-wire welding, respectively. The above-mentioned distances were chosen according to previous experiences gained from the corresponding experiments: In laser-arc hybrid welding, use of a short D_{LA} (2–4mm) was observed to ensure robust process behaviour and produce lesser welding spatters. In order to secure fluent wire melting in laser welding with cold-wire process, however, wire is advisable to feed direct into the laser beam spot that is produced on the work piece surface. Test welds with 0.8 mm wide root gap (groove type B3) showed that the laser spot diameter had to get wider in order to ensure proper melting of the fusion faces of the groove. Consequently, a defocused laser beam (F = +20 / beam spot diameter $\sim \varnothing$ 1.2 mm) was used in the welding experiments with parameter combinations A1 + B3 and A2 + B3

(Table 3). Figure 3b,d show the defocusing configurations with focal point position set to 20 mm above the test piece surface for the laser-arc hybrid and laser cold-wire welding experiments, respectively.

Table 3. Welding parameter combinations in laser-arc hybrid and laser cold wire welding tests and weld identification designation. Abbreviations (A1, A2 and B1–B4) are explained in page 3.

Studied Parameter Combinations	Laser-Arc Hybrid Weld Identification	Laser Cold-Wire Weld Identification
A1 + B1	-	LCW1
A2 + B1	-	LCW2
A1 + B2	LAH1	LCW3
A2 + B2	LAH2	LCW3
A1 + B3	LAH3	LCW5
A2 + B3	LAH4	LCW6
A1 + B4	LAH5	LCW7
A2 + B4	LAH6	LCW8

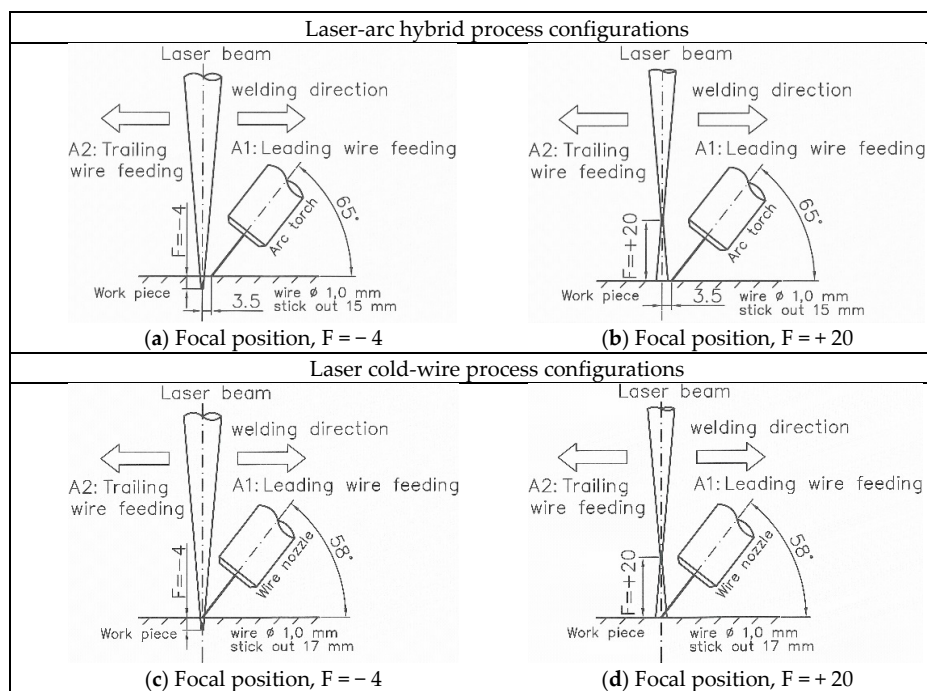


Figure 3. Set-up of laser beam and filler wire feeding arrangements used in laser-arc hybrid welding (upper row; a,b) and laser cold-wire welding (lower row; c,d). A1 = leading wire feeding. A2 = trailing wire feeding.

The welds produced were cut transversally into specimens for metallographic examination. The cutting locations were in the middle area of the 300 mm long welds in order to ensure that the analysed weld cross-section is from a location where the welding process has already stabilized. During the metallographic preparation, the specimens were ground, polished and electrolytically etched (10% aqueous oxalic acid, 30V/2A/40s) to reveal the macroscopic weld cross-section appearance and weld microstructures. A light microscope was used for metallographic observation of the cross-sectional weld specimens. In addition, EDS analysis of selected weld cross-sections was done using a Hitachi SU3500 scanning electron microscope and a Thermo Scientific Ultradry DSS EDS-detector. Chromium

(Cr) was selected as a trace element and its distribution and quantity within the test weld cross-sections were identified using a transverse stepwise characterization and mapping technique. Weld metal Cr-values acquired from the EDS stepwise characterization were compared to known Cr-values of the base metal (17.6 weight-%) and filler metal (22.9 weight-%) to determine the filler metal mixing of each selected test weld (see Equation (1)). For example, if the detected chromium content of a measured point in the weld metal were 17.6 or 22.9 weight-%, the filler metal mixing would be 0 or 100%, respectively. The above relationship is shown in Figure 4, which illustrates how specific chromium weight-% content in the weld metal corresponds to filler metal mixing percent value.

$$\text{Filler metal mixing \%} = \frac{(\text{weld metal Cr content}) - (\text{base metal Cr content})}{(\text{filler metal Cr content}) - (\text{base metal Cr content})} \times 100 \quad (1)$$

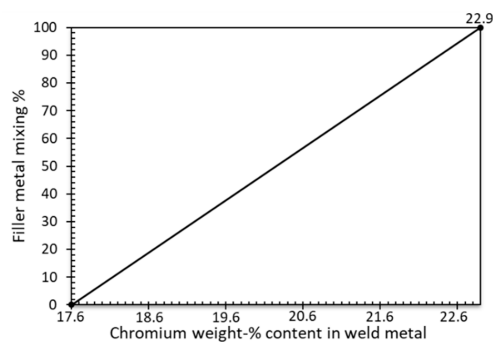


Figure 4. Relationship between chromium content in the weld metal and corresponding filler metal mixing-%. On the horizontal axis, 17.6 represents chromium weight-% content equal to the base metal and 22.9 is the chromium weight-% content of the filler metal.

In the EDS stepwise characterization, an acceleration voltage of 20 kV and sampling time of 90 s were used. As the aim was to study weld metal mixing and homogeneity at a macroscopic scale, the measurement “spot” size and step interval within the measurement line were chosen accordingly. Thus, measurement spot size of 40 μm \times 60 μm and step interval of 100 μm (distance between individual spots) were used to ensure that an individual measurement spot gave data over several dendrites/dendrite spacing at every step. EDS measurements included four horizontal line segments from each studied weld cross-section sample running transversally across the weld fusion zone. In the vertical direction, the first measurement line segment (ML1) was placed 1 mm below the weld surface while the last measurement line segment (ML4) was near the root portion located 1 mm above the back surface of the test specimen. The other lines (ML2 and ML3) were evenly distributed vertically between lines ML1 and ML4 at intervals approx. 2.7 mm away from each other. Figure 5 presents an example showing the locations of the EDS-measurement lines in the studied weld cross-sections. Line segments had 15–65 measurement points depending on the width of the weld at the measurement location in question. In EDS mapping, the characterizations were done with an acceleration voltage of 20 kV and using a resolution of 256 \times 192 pixels. Mapping data was collected until an average 5000 counts per pixel was acquired.

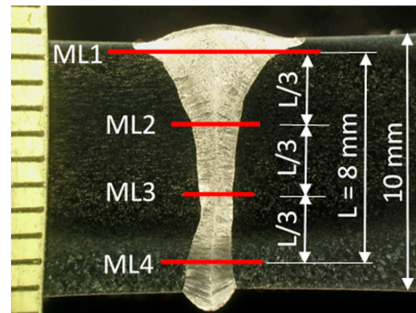


Figure 5. Example showing transversal EDS-measurement line locations (in red) ML1, ML2, ML3 and ML4 in the studied weld cross-sections.

In weldability analysis, dilution is conventionally determined mathematically from the cross-sectional areas of the original joint geometry, melted base metal and weld metal. Dilution ratio is the ratio of the amount of melted base metal to the total amount of fused weld metal [22].

To get a quantitative basis for comparison of the weld cross-sections and to analyse how different groove configurations and wire feeding direction affect the base/filler metal-ratio, the following assessment procedure was used: The weld macrograph cross-sections were converted into CAD-images and the groove geometry superimposed over the original weld cross section. The vertical symmetry axis of the groove was aligned with the centreline of the studied weld cross-section. The cross-sectional areas of the melted base metal, filler metal and weld metal were then defined using area inquiry tools of CAD-software (Autodesk, San Rafael, CA, USA). An example of the above principle is shown schematically in Figure 6. The figure shows dilution calculation and boundary lines of the defined regions of cross-sectional areas converted from the macrograph of test weld LAH1. Dilution calculation gives a dilution ratio of 79%, which means that the weld metal of test sample LAH1 is estimated to contain 79% base metal and 21% filler metal. Normal practice usually assumes that the proportions of base and filler metal are completely mixed and evenly distributed throughout weld cross-section. In welding of rather thin plate thicknesses in which joint penetration of a single pass weld is around 5 mm or less, this assumption would normally be reasonable but for thick section welding, it may not lead to an appropriate outcome, as will be seen in this work.

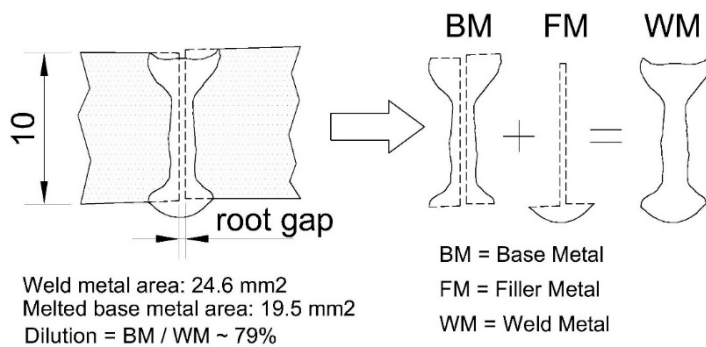


Figure 6. Example showing the cross-sectional area defined from the macrograph of test weld LAH1.

3. Results and Discussion

Figures 7 and 8 present weld cross-sections from laser-arc hybrid welding experiments and laser cold-wire experiments, respectively. Table 4 summarizes cross-sectional areas and calculated base/filler metal portions for the laser arc-hybrid and laser cold-wire test welds.

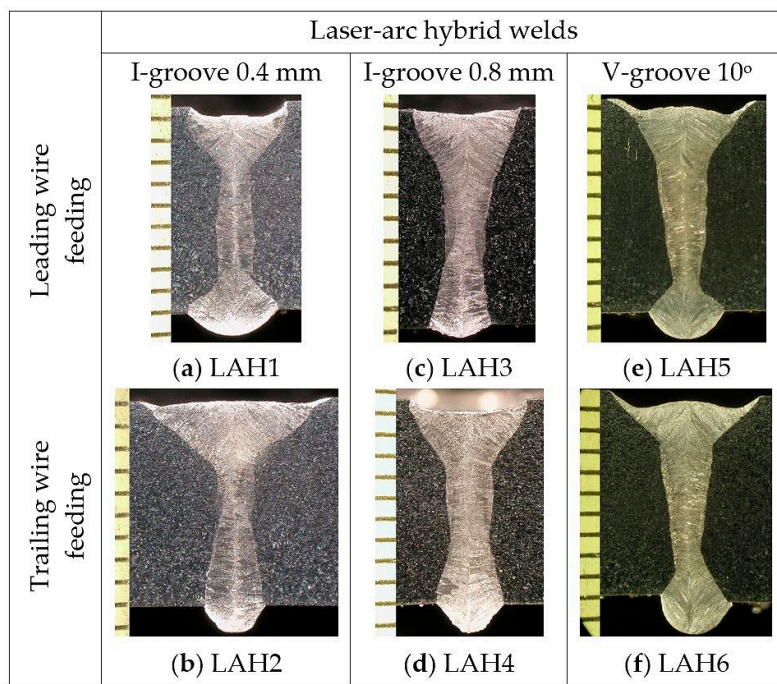


Figure 7. Weld cross-sections (a–f) from laser-arc hybrid welding tests.

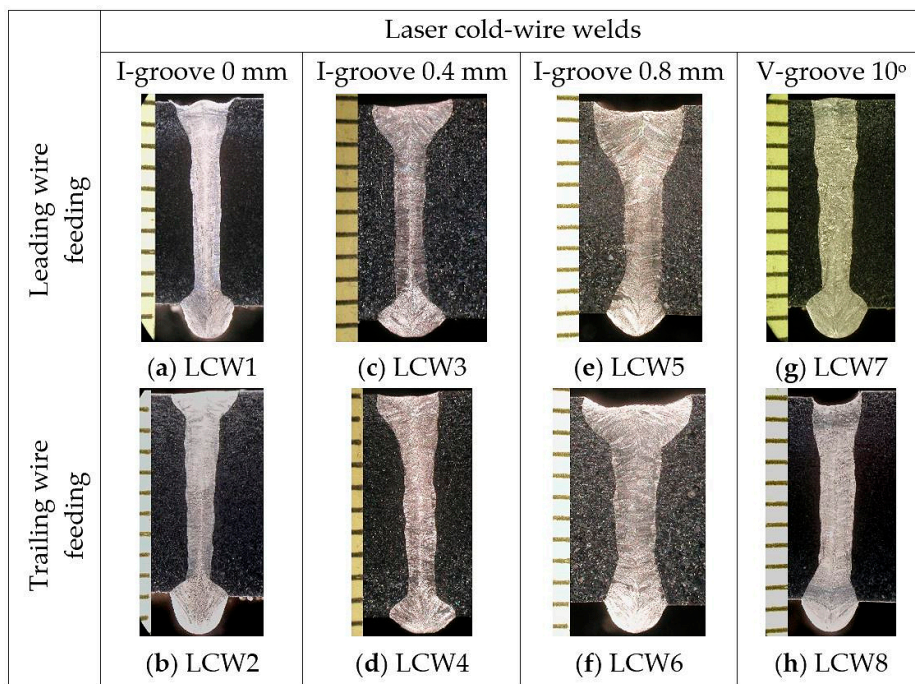


Figure 8. Weld cross-sections (a–h) from laser cold-wire welding tests.

Table 4. Summary of cross-sectional areas of laser arc-hybrid (LAH) and laser cold-wire (LCW) test welds. Welding energy input values per weld length [kJ/mm]: LAH1&2 = 0.57; LAH3&4 = 0.77; LAH5&6 = 0.64; LCW1-6 = 0.55; LCW7&8 = 0.46.

Weld Identification	Melted Base Metal Area [mm ²]	Melted Filler Metal [mm ²]	Weld Metal Area [mm ²]	Base Metal Dilution [%]	Filler Metal Portion [%]
LAH1	19.5	5.1	24.6	79	21
LAH2	25.8	5.4	31.2	83	17
LAH3	16.7	8.2	24.9	67	33
LAH4	19.9	8.6	28.5	70	30
LAH5	17.1	9.3	26.4	65	35
LAH6	19.5	9.9	29.4	66	34
LCW1	14.2	3.1	17.3	82	18
LCW2	15.1	4.1	19.2	79	21
LCW3	13.5	5.2	18.7	72	28
LCW4	12.3	5.1	17.4	71	29
LCW5	16.2	8.2	24.4	66	34
LCW6	17.1	8.6	25.7	67	33
LCW7	8.6	11.3	19.9	43	57
LCW8	9.0	10.2	19.2	47	53

When comparing the cross-sectional areas of the weld metal and melted base metal of the test samples made in an I-groove configuration with a 0.4 mm wide root gap and the samples with a V-groove configuration in Table 4, it can be seen that the values are higher for laser arc-hybrid welds than for the corresponding laser cold-wire welds. The higher values result from the higher welding energy and enhanced melting capability of the laser-arc hybrid process. Depending on the wire feeding rate, which was 5, 11.5 and 15 m/min, the gas metal arc process contributes additional welding energy of several kilowatts (2.3/6.7/7.1 kW) compared to laser cold-wire welding process, where the laser beam is the only source of welding energy. It should be noted, however, that there is little difference in the base metal and filler metal proportions in the test welds made in I-groove configuration with 0.8 mm root gap (see LAH3&4 versus LCW5&6 in Table 4). This finding is related to the use of a defocused laser beam for welding the wider root gap of 0.8 mm. Defocusing with a focal point position value of +20 mm produces a \varnothing ~1.2 mm wide laser spot diameter, which is 50% wider than the laser spot diameter used in the other welding trials, where the focal point position value was set to -4 mm (spot \varnothing 0.8 mm). In the case of the laser cold-wire welding, the use of a wider laser spot diameter results in melting of the base metal over a wider area and consequently there is a broader weld cross-section profile.

3.1. Mixing Behavior in Laser-Arc Hybrid Test Welds

As noted earlier, conventional dilution calculations based on the weld cross-sectional area are not always suitable for thicker weld cross-sections, which motivated more detailed examination of the mixing of the filler metal in the test welds. Mixing in the vertical direction from the weld surface to the root and the uniformity of the mixing, that is, how homogeneously the filler metal is distributed across the whole weld cross-section, were of particular interest. EDS mapping and stepwise line characterization were used to reveal possible differences in chromium distribution between the over-alloyed filler metal and base metal.

Figure 9 shows EDS mapping results for the laser-arc hybrid test welds. The images show chromium distribution in weight-% for each test weld cross-section. The chromium distribution is visualized using colour contouring. Greenish colours present the chromium weight-% content level of the base metal and dark red shows chromium weight-% content close to that of the filler metal. Yellow and orange colours are chromium weight-% content levels between these extremes. The mixing results from EDS stepwise characterization are presented as transversal filler metal mixing profiles

(measurement lines 1 to 4) calculated according to Equation (1). Figure 10 presents tabular data for average values of filler metal mixing determined at the measurement lines ML1–ML4 of the laser-arc hybrid test welds.

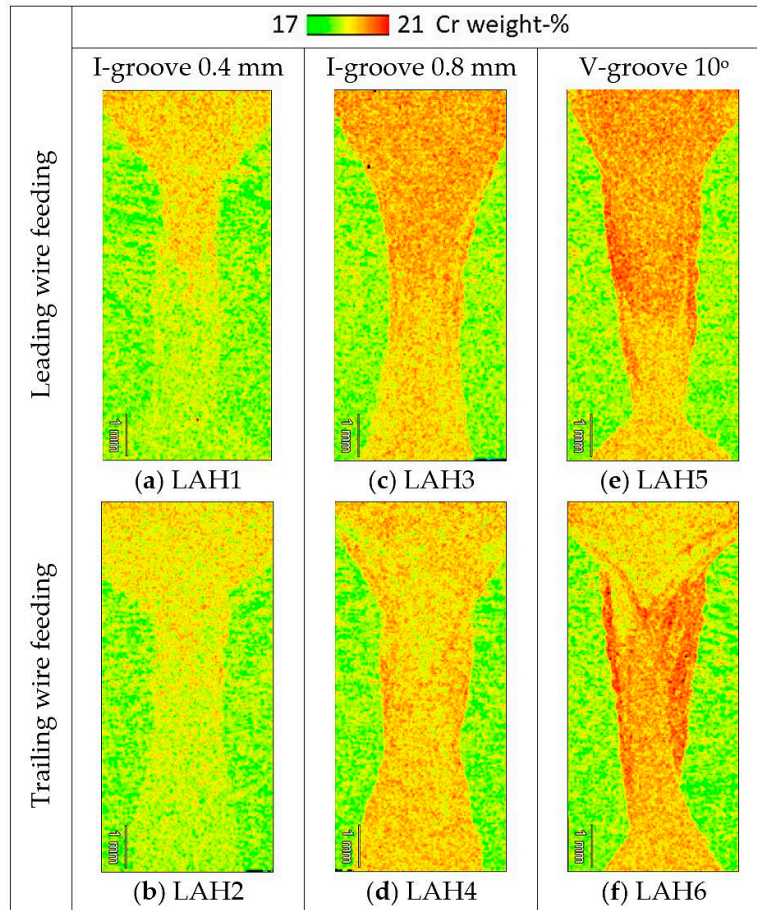


Figure 9. Energy dispersive spectroscopy (EDS) mapping images (a–f) showing the distribution of chromium in laser arc-hybrid test welds.

The images in Figure 9 show a clear difference in filler metal mixing between the weld surface part (upper half) and the weld root part (lower half) of the weld cross-sections of the I-groove weld with 0.4 mm root gap (Figure 9a,b). The same behaviour can be seen for both leading and trailing filler wire feeding. More reddish colour contouring indicates that more intensive mixing has occurred on the weld surface with leading wire feeding; on the other hand, trailing wire feeding seems to have provided slightly better mixing from the weld midsection towards the weld root. Figure 10 shows that the average filler metal mixing-% values of test welds LAH1 and LAH2 are around 38% and 31–34% for the upper half of weld cross-section and ~26% and ~25–28% for the lower half, respectively.

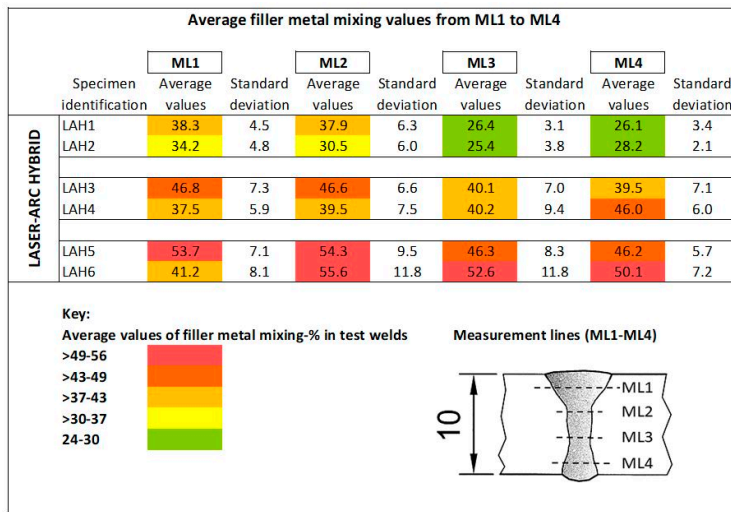


Figure 10. Average values of filler metal mixing-% from the data of measurement lines ML1–ML4 in laser-arc hybrid test welds.

When the root gap is widened from 0.4 mm to 0.8 mm, mixing becomes noticeably better throughout the weld cross-section. The results of both leading and trailing wire feeding with 0.8 mm root gap (Figure 9c,d) show enhanced mixing behaviour across the whole weld cross-section in terms of higher chromium contents and enhanced distribution. The use of trailing wire feeding (Figure 9d) shows slightly better mixing at the weld root portion than leading wire feeding (Figure 9c). Mixing at the weld surface portion of the weld displays the opposite behaviour with slightly better mixing for leading wire feeding. The mixing results from EDS stepwise characterization show the same trend. Average filler metal mixing values in the weld root portion (ML4) of test weld LAH4 (trailing wire feeding) and LAH3 (leading wire feeding) are 46% and 39.5%, respectively (Figure 10). At the weld surface part (ML1), corresponding average values are 37.5% and 46.8%, respectively. If the mixing profiles in Figures 11d and 12d are examined, it can be noticed that the mixing profile at the measurement line 4 (ML4) is smoother in LAH4 than in LAH3. The majority of mixing %-values of ML4 of weld LAH4 are between ~45% and 50%, whereas in weld LAH3 mixing %-values show greater fluctuation and are between ~35% and 45%. The mixing at the weld surface part (upper half) seems, however, to be more homogenous in weld LAH3, which was made with leading wire feeding, than weld LAH4, made with trailing wire feeding. When the mixing profiles of ML2 near the weld surface in Figures 11b and 12b are compared, it can be seen that the mixing profile is smoother and shows less variation in weld LAH3 than weld LAH4. Trailing wire feeding with the laser-arc hybrid process melts more base metal than leading wire feeding (see Table 4) and the observation of less homogeneously distributed filler metal in the weld surface part of the weld with trailing wire feeding can be partly attributed to the higher local base metal dilution at the weld surface part of the weld. In Figure 9d, a wedge-shaped fusion area can be seen near the weld surface. The inside area and tip of the wedge contain spots of green and yellowish colours indicating chromium content levels of the base metal.

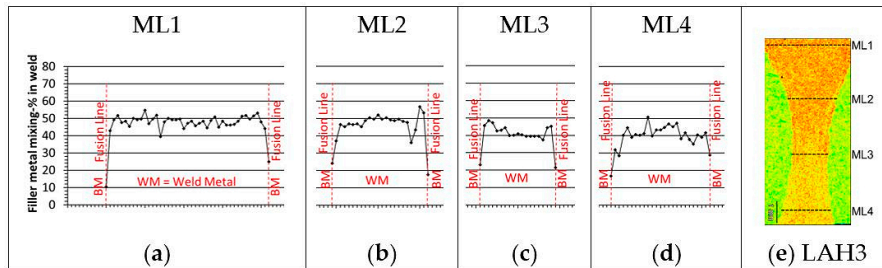


Figure 11. Filler metal mixing results from EDS stepwise characterization. (a–d) Filler metal mixing-% profiles of measurement lines 1–4 (ML1–ML4) from test weld LAH3 (e). In figures (a–d) one step between adjacent measurement points in the horizontal axis equals 100 micrometres.

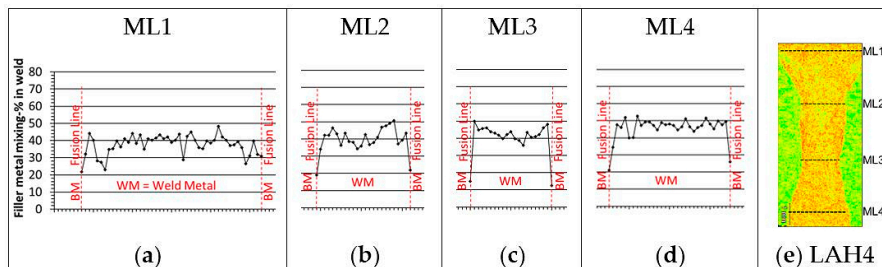


Figure 12. Filler metal mixing results from EDS stepwise characterization. (a–d) Filler metal mixing-% profiles of measurement lines 1–4 (ML1–ML4) from test weld LAH4 (e). In figures (a–d) one step between adjacent measurement points in the horizontal axis equals 100 micrometres.

When laser-arc hybrid welds were produced in single-pass V-groove configuration, average filler metal mixing values of measurement lines ML1 to ML4 had the highest mixing values of the laser-arc hybrid test welds. From Figure 10, it can be seen that in weld LAH5, which was made using leading wire feeding, the average filler metal mixing values are ~46% at the bottom part of the groove area (ML3 and ML4) and ~54% at the surface part (ML1 and ML2). The test weld LAH6, which was made using trailing wire feeding, shows ~56% average mixing level values at one third thickness of the joint (ML2) and when measuring deeper in the joint at ML3 and ML4, average values were ~53% and 50%, respectively. When examining Figure 9e and particularly Figure 9f, it can be noticed that chromium as regards weight-% is not homogeneously distributed in the mid-section area of both weld LAH5 and LAH6. Red and orange colours indicating high chromium weight-% levels can be clearly seen near the fusion lines at the mid-thickness range of both welds. The filler metal mixing profiles of weld LAH5 and LAH6 in Figures 13 and 14 support the above observation. Large spikes can be seen in the mixing profiles of Figure 13b,c and Figure 14b,c with high local values of 60–75% in the mid-thickness area of weld cross-sections LAH5 and LAH6. In addition, it can be seen that test weld LAH6 has similar mixing behaviour near the weld surface as earlier described in test weld LAH4. Both weld LAH6 and LAH4 were produced using trailing wire feeding.

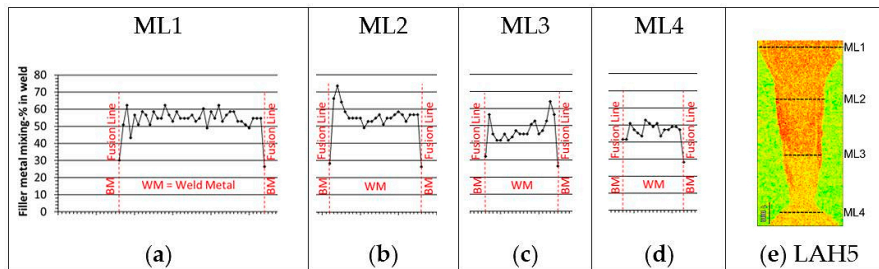


Figure 13. Filler metal mixing results from EDS stepwise characterization. (a–d) Filler metal mixing-% profiles of measurement lines 1–4 (ML1–ML4) from test weld LAH5 (e). In figures (a–d) one step between adjacent measurement points in the horizontal axis equals 100 micrometres.

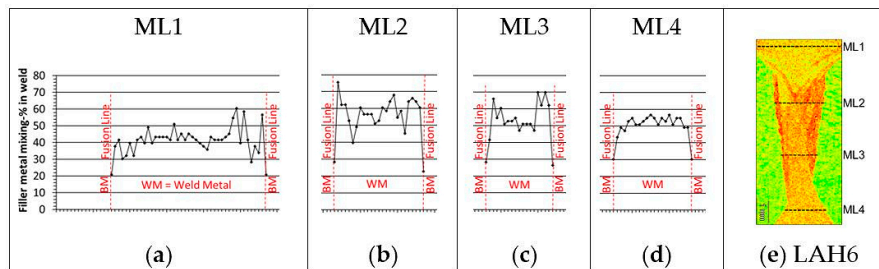


Figure 14. Filler metal mixing results from EDS stepwise characterization. (a–d) Filler metal mixing-% profiles of measurement lines 1–4 (ML1–ML4) from test weld LAH6 (e). In figures (a–d) one step between adjacent measurement points in the horizontal axis equals 100 micrometres.

As a whole, test welds LAH3 and LAH4 exhibited the best overall results of the laser-arc hybrid test welds, corresponding to homogenous filler metal distribution throughout the whole weld cross-section. If intensive and homogenous mixing in the root portion is preferred, test weld LAH4 with trailing wire feeding showed more even mixing behaviour than test weld LAH3.

Sohail et al. [17] used modelling and simulations in mixing and fluid flow studies for full penetration laser-gas metal arc hybrid welding of 10 mm thick closed butt-joints with leading and trailing torch configuration. In their studies, the longitudinal sections of the simulated weld pool showed different behaviour of flow patterns and temperature contours between the trailing and leading torch. In the leading torch configuration, the modelling results indicated a solidifying peninsula growing horizontally at the mid-thickness range of weld pool, which partly sectioned the melt pool to upper and lower half. The mentioned solidification peninsula may obstruct the circulation of the melt flow between the weld surface and root, which in turn may reduce the mixing of weld metal. This melt pool behaviour with solidification peninsula was not seen in the trailing torch simulations. Consequently, with the trailing torch configuration the mixing at the root portion of weld was observed to be more intensive than with the leading torch. The mentioned observations in the reference [17] may also explain why the trailing wire feeding results of laser-arc hybrid experiments presented in this work showed enhanced mixing behaviour near the weld root portion compared to the corresponding results achieved with the leading wire feeding.

3.2. Mixing Behavior in Laser Cold-Wire Test Welds

Figure 15 shows EDS mapping results for the laser cold-wire test welds. The images in Figure 15 show chromium distribution in weight-% for each test weld cross-section. Figure 16 presents tabular data for average values of filler metal mixing determined at the measurement lines ML1–ML4 of the laser cold-wire test welds. Examination of Figure 15a–e shows a clear difference in filler metal

mixing between the weld surface part (upper half) and the weld root part (lower half) of the weld cross-sections when the root gap of the I-groove was closed or 0.4 mm. In Figure 16, average filler metal mixing values in test welds LCW3 and LCW4 are around ~32–36% in the lower half of the weld cross-sections (ML3–ML4), whereas the level in the upper half of the weld is much higher, ~48–54%. The same mixing behaviour can be seen for both leading and trailing filler wire feeding. Comparison of the EDS-mapping images of welds LCW3 and LCW4 in Figure 15c,d indicates that slightly more intensive mixing occurred in the lower half of the joint in weld LCW3, which was produced with leading wire feeding.

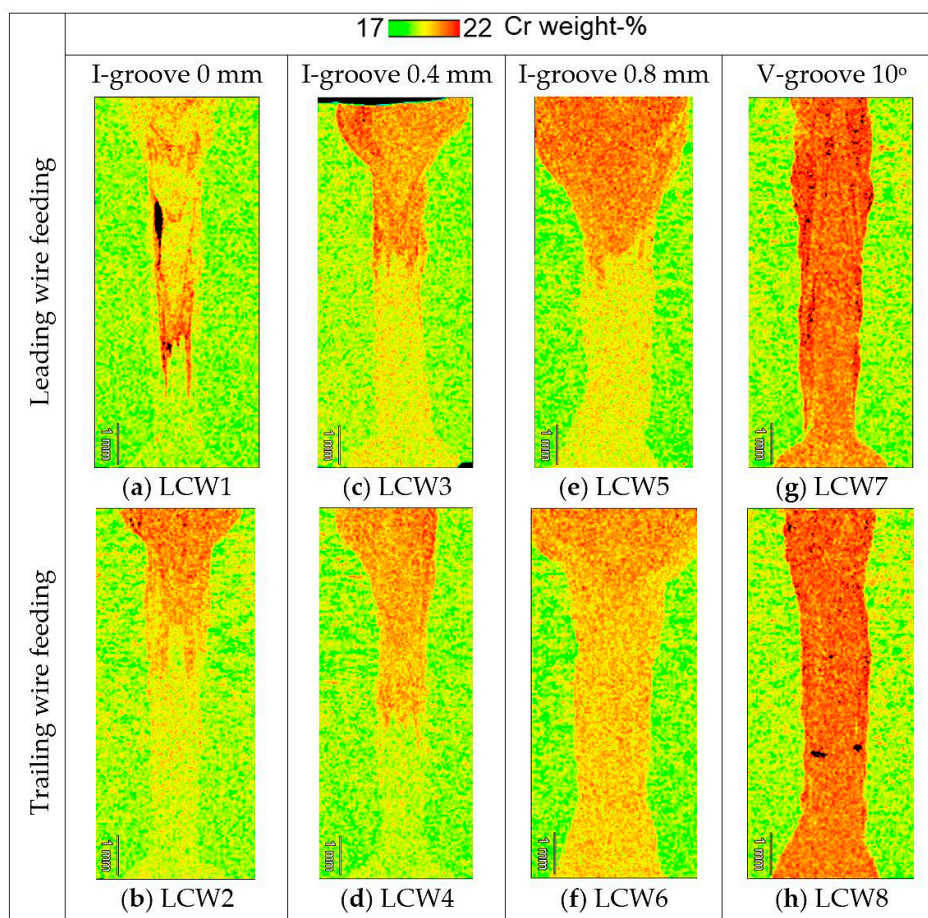


Figure 15. EDS mapping images (a–h) showing the distribution of chromium in laser cold-wire test welds.

Average filler metal mixing values from ML1 to ML4									
Specimen identification	ML1		ML2		ML3		ML4		Standard deviation
	Average values	Standard deviation	Average values	Standard deviation	Average values	Standard deviation	Average values	Standard deviation	
LASER COLD-WIRE	LCW1	41.6	9.9	42.3	11.9	46.6	20.3	29.1	3.0
	LCW2	50.4	7.4	37.4	7.1	28.0	3.0	26.8	2.6
	LCW3	53.6	8.0	52.4	14.2	35.5	3.5	36.2	3.0
	LCW4	52.5	6.8	48.6	10.3	32.2	3.8	32.3	4.3
	LCW5	56.5	9.1	46.1	13.8	33.1	5.3	34.8	4.7
	LCW6	47.2	8.7	43.9	5.6	39.3	7.4	41.9	7.3
	LCW7	62.4	11.0	62.7	12.8	59.9	12.0	58.0	12.2
	LCW8	67.3	4.6	63.6	7.9	59.9	15.0	60.0	14.3

<p>Key: Average values of filler metal mixing-% in test welds</p> <ul style="list-style-type: none"> >62-68 >56-62 >49-56 >43-49 >37-43 >30-37 24-30 		<p>Measurement lines (ML1-ML4)</p>
--	--	---

Figure 16. Tabular data presenting average values of filler metal mixing-% from the data of measurement lines ML1–ML4 in laser cold-wire test welds.

When the root gap was widened to 0.8 mm, leading wire feeding still has a clear difference in mixing between the upper and lower half of the weld cross-section, Figure 15e. However, the results of trailing wire feeding with 0.8 mm root gap show enhanced mixing behaviour across the whole weld cross-section in terms of higher chromium weight-% and more homogenous distribution, Figure 15f. Figure 16 shows average filler metal mixing values between 39% and 42% for test weld LCW6 at measurement lines ML3 and ML4. In addition, Figure 17d, which presents the mixing profile for the weld root portion, shows homogenous mixing at the bottom of the groove.

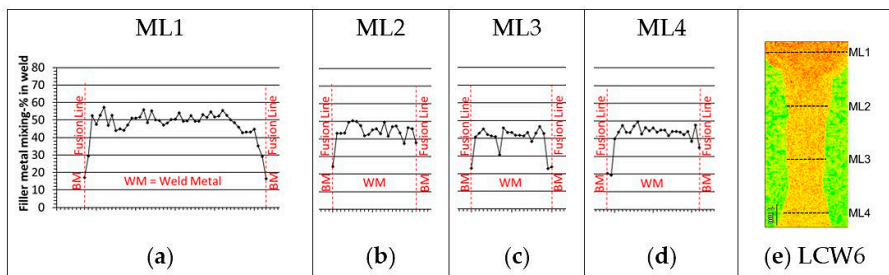


Figure 17. Filler metal mixing results from EDS stepwise characterization. (a–d) Filler metal mixing-% profiles of measurement lines 1–4 (ML1–ML4) from test weld LCW6 (e). In figures (a–d) one step between adjacent measurement points in the horizontal axis equals 100 micrometres.

In the closed square butt weld with zero root gap, the filler metal mixing behaviour was remarkably inhomogeneous. In Figure 15a,b, distinctive colour contrast can be seen between high chromium and low chromium weight-% areas. Figure 18 shows mixing profiles derived from the EDS-line scans and micrographs taken at the same locations (Figure 18a). Local inhomogeneous mixing is clearly visible in the EDS chromium mapping image of the zero root gap test weld LCW1. Mixing profiles at the measurement lines 2 and 3 (Figure 18d,e) point out acute local changes in weld metal chemical composition. Micrographs (Figure 18b,c) reveal that composition variations in the weld metal have

induced a change in weld solidification mode from primary austenite to primary ferrite solidification. Microstructural solidification features of both modes can be seen side-by-side and solidified islands of primary ferrite are present in locations where the weld metal contains a high amount of filler metal. Large local spikes in the mixing profiles indicate that the difference between the high and low mixing value levels could be almost 45%-units.

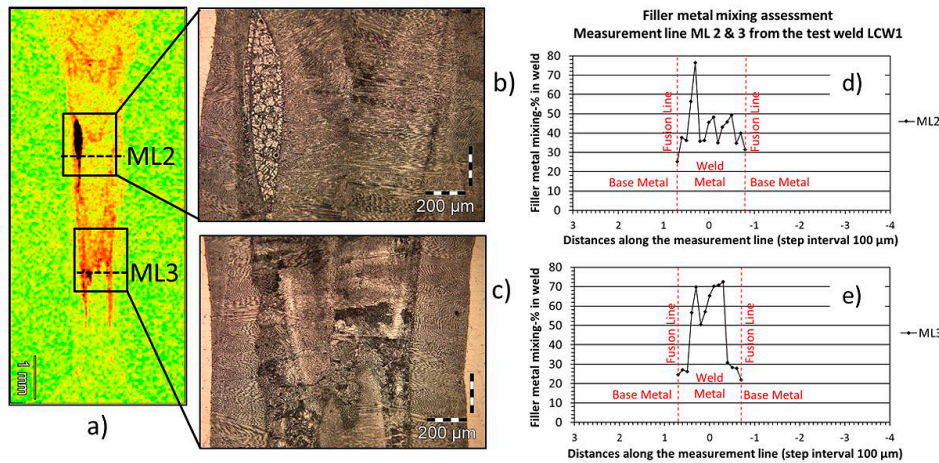


Figure 18. Example of mixing behaviour in a laser cold-wire weld produced in I-groove configuration with closed gap. Micrographs (b,c) and filler metal mixing profiles (d,e) at corresponding locations (a) showing inhomogeneous mixing occurred in laser cold-wire test weld LCW1.

The results given in Figure 16 show that the V-groove weld configuration gave the highest average filler metal mixing values of the laser cold-wire welding trials. Average filler metal mixing values in percent were in the range 58–62% and 60–67% at measurement lines 1 to 4 of the test welds LCW7 and LCW8, respectively. Comparison of leading and trailing wire feeding based on the chromium weight-% mapping images of Figure 15g–h and the filler metal mixing profiles in Figures 19 and 20 indicates that the mixing homogeneity is best in weld LCW8, which was made with trailing wire feeding. Overall, test welds LCW6 and LCW8 gave the best results, corresponding to homogenous filler metal distribution across the whole weld cross-section. Both LCW6 and LCW8 were produced using trailing wire feeding.

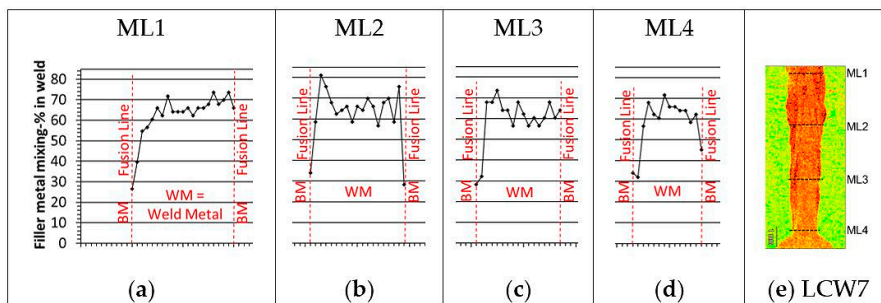


Figure 19. Filler metal mixing results from EDS stepwise characterization. (a–d) Filler metal mixing-% profiles of measurement lines 1–4 (ML1–ML4) from test weld LCW7 (e). In figures (a–d) one step between adjacent measurement points in the horizontal axis equals 100 micrometres.

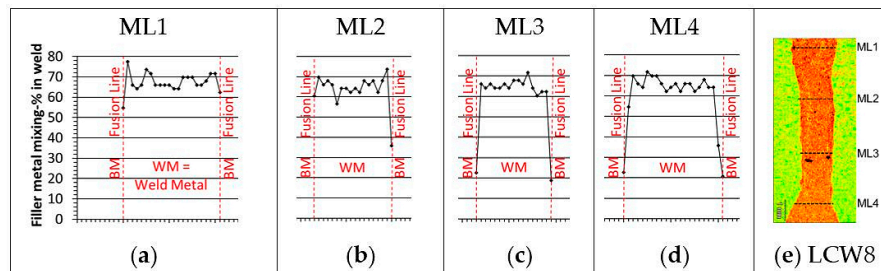


Figure 20. Filler metal mixing results from EDS stepwise characterization. (a–d) Filler metal mixing-% profiles of measurement lines 1–4 (ML1–ML4) from test weld LCW8 (e). In figures (a–d) one step between adjacent measurement points in the horizontal axis equals 100 micrometres.

3.3. Mixing Behavior Comparison between Laser-Arc Hybrid and Laser Cold-Wire Processes

In square butt welds with narrow root gap (0.4 mm) the difference in mixing between the upper and lower halves of the joint thickness was more discernible in the weld samples produced with laser cold-wire welding than with laser-arc hybrid welding. When the root gap was 0.8 mm, the weld made with laser cold-wire welding and leading wire feeding still showed inhomogeneous mixing between the upper and lower halves of the joint. With trailing wire feeding, on the other hand, more even mixing behaviour was found. Corresponding samples for laser-arc hybrid welding and 0.8 mm root gap showed more even mixing behaviour with leading wire feeding compared to the laser cold-wire process. Trailing wire feeding with 0.8 mm root gap produced the best mixing of the laser-arc hybrid test welds and, especially at the weld root, the average mixing-% was somewhat higher than in corresponding laser cold-wire test welds. With the V-groove welds, the laser cold-wire process with trailing wire feeding exhibited superior mixing behaviour in terms of more homogenous filler metal distribution from the weld surface to the weld root. The V-groove welds with laser-arc hybrid welding, in turn, showed high average mixing-% values in all four measurement lines (ML1–ML4) from the weld surface to root but the overall homogeneity of the fusion zone mixing was only moderate.

In the case of the laser-arc hybrid process, the electromagnetic force, that is, the Lorentz force, is known to act in the weld pool due to the electric current and the magnetic field induced. The Lorentz force is one of the driving forces for fluid flow in the weld pool during arc welding. The Lorentz force pushes liquid metal downward from the surface of the centre axis of the melt pool and liquid metal is circulated along both sides of the weld pool boundaries and rises back to weld surface [23]. In the laser-arc hybrid welds, the Lorentz force could have been augmenting weld metal mixing with convective fluid flow, which would cause a stirring effect in the melt pool.

3.4. Practical Aspects

The mixing studies indicate that both welding processes benefit from the use of larger groove cross-sections. The use of a wider root gap in the I-groove welds, for example, helped to introduce filler metal into the bottom of the groove. In practice, with open square preparation where a wide root gap is used in thick-section welding, the diameter of the laser beam spot needs to be wide enough and the power density of the beam must simultaneously be sufficient to ensure both proper melting of the joint fusion faces and to enable keyhole formation. It should be noted that the mixing results for the thick-section welds described in this work represent one transversal cross-section sample per test weld joint produced. Welding in general and laser-arc/cold wire-based keyhole welding in particular, are dynamic processes. Consequently, some natural variation in mixing and the resulting weld metal composition along the solidified weld joint can be expected even if all the welding experiments are carried out in the proper parameter window and in a robust manner. However, the results presented

offer some indication of how mixing can be considered in welding parameter planning for thick section welding with laser-arc or laser cold wire-based processes.

4. Conclusions

Laser-arc hybrid and laser cold-wire welding tests were conducted on 10 mm thick butt-welded joints of AISI 316L austenitic stainless steel base metal using an overmatching type 2205 duplex stainless steel filler metal. The objective of the work was to study filler metal mixing behaviour in laser-arc hybrid welding and laser cold-wire welding. The following variables and their effect on mixing behaviour were of interest: leading and trailing filler wire feeding and butt-joint preparation, namely I-groove and V-groove type welds.

The following conclusions can be drawn from the results of the laser-arc hybrid welding tests:

- i Open square preparation (I-groove) with a 0.4 mm root gap in a 10 mm thick butt joint showed a clear difference in filler metal mixing between the upper half and lower half of the weld cross-section. Average filler metal mixing values in percent were within the range ~31–38% in the upper half of the weld cross-section but only ~25–28% in the lower half of the weld.
- ii Increasing the cross-sectional groove area by using a root gap of 0.8 mm in a square butt weld (I-groove) enhanced filler metal mixing across the whole weld cross-section. This change was particularly evident in the root portion of the test welds, where average mixing values in percent were between ~40–46%.
- iii With laser-arc hybrid welding, V-groove type welds with trailing and leading wire feeding had the highest filler metal mixing values (averages from 41% to 56%) but the homogeneity of the mixing was not as good as I-groove welds with 0.8 mm wide root gap.
- iv In all test welds, trailing filler wire feeding produced stronger filler metal mixing in the root portion than leading filler wire feeding.
- v Near the weld surface, the average filler metal mixing-% values were smaller when using trailing wire feeding (i.e. trailing torch) than leading wire feeding (i.e. leading torch). This result was probably caused by larger local base metal dilution near the weld surface when a trailing torch configuration was used.

Following conclusions can be drawn from the results of the laser cold-wire welding tests:

- i In closed square (zero root gap) welds, filler metal mixing behaviour was observed to be remarkably inhomogeneous with both leading and trailing wire feeding compared to the welds with wider gaps. Large local spikes in mixing profiles were found and the difference between the high and low mixing values could be almost 45%-units. Acute local changes in the chemical composition of the weld metal induced changes in the weld solidification mode, which had separate islands of both primary austenite and primary ferrite solidification microstructures.
- ii A clear difference was noticed in filler metal mixing between the upper half and lower half of the weld cross-sections in the case of the I-groove weld with 0.4 mm root gap for both leading and trailing filler wire feeding. When the root gap was widened to 0.8 mm, leading wire feeding still showed a noticeable difference in mixing between the upper and lower half of the weld cross-section. Corresponding results with trailing wire feeding, however, showed enhanced mixing behaviour across the whole weld cross-section with greater homogeneity and higher mixing values. Average filler metal mixing values in percent were in the range ~39–47% for the entire weld cross-section.
- iii Utilization of V-groove preparation with trailing wire feeding gave the best filler metal mixing in terms of both homogeneity and high mixing values. Average filler metal mixing values in percent were in the range ~60–67% for the entire weld cross-section.

Overall, the results of the mixing studies indicate that both welding processes benefit from the use of a larger groove cross-section. The use of trailing wire feeding showed more robust mixing behaviour

with V-groove preparation for the laser cold-wire process and with I-groove preparation with a 0.8 mm root gap for the laser-arc hybrid process.

Author Contributions: Methodology, M.K.; Investigation, M.K.; Manuscript writing, MK; Manuscript reviewing, V.K., H.E., A.S.; Supervision, V.K., H.E.

Acknowledgments: The authors would like to thank Pertti Kokko for his assistance with the welding experiments, Antti Heikkinen for help with the metallographic preparations, Toni Väkiparta for carrying out the EDS-measurements and Peter Jones for help with the English language. The authors would also like to acknowledge the DigRob project of Business Finland for financial support.

Conflicts of Interest: The authors declare no conflict of interest.

References

1. Kawahito, Y.; Wang, H.; Katayama, S.; Sumimori, D. Ultra high power (100 kW) fibre laser welding of steel. *Opt. Lett.* **2018**. [[CrossRef](#)] [[PubMed](#)]
2. Katayama, K.; Kawahito, Y.; Kinoshita, K.; Matsumoto, N.; Mizutani, M. Weld penetration and phenomena in 10 kW fibre laser welding. In Proceedings of the 26th International Congress on Applications of Lasers & Electro-Optics, Orlando, FL, USA, 29 October–10 November 2007; pp. 253–359.
3. Vollertsen, F.; Grünenwald, S.; Rethmeier, M.; Gumenyuk, A.; Reisinger, U.; Olschok, S. Welding thick steel plates with fibre lasers and GMAW. *Weld. World* **2010**, *54*, R61–R70. [[CrossRef](#)]
4. Nielsen, S.E. High power laser hybrid welding—Challenges and perspectives. *Phys. Proc.* **2015**, *78*, 24–34. [[CrossRef](#)]
5. Kristensen, J.K. Applications of laser welding in the shipbuilding industry, Part IV Applications of laser welding. In *Handbook of Laser Welding Technologies*; Katayama, S., Ed.; Woodhead Publishing Limited: Cambridge, UK, 2013; pp. 596–611. [[CrossRef](#)]
6. Dilthey, U.; Keller, H.; Ghandehari, A. Laser beam welding with filler metal. *Steel Res.* **1999**, *70*, 199–202. [[CrossRef](#)]
7. Dilthey, U.; Wiesschemann, A. Perspectives offered by combining a laser beam with arc welding procedures. *Weld. Int.* **2003**, *16*, 711–719. [[CrossRef](#)]
8. Jokinen, T.; Karhu, M.; Kujanpää, V. Welding of thick austenitic stainless steel using Nd:yttrium–aluminum–garnet laser with filler wire and hybrid process. *J. Laser Appl.* **2003**, *15*, 220–224. [[CrossRef](#)]
9. Salminen, A.S.; Kujanpää, V.P. Effect of wire feed position on laser welding with filler wire. *J. Laser Appl.* **2003**, *15*, 1–9. [[CrossRef](#)]
10. Ohnishi, T.; Kawahito, Y.; Mizutani, M.; Katayama, S. Butt welding of thick, high strength steel plate with a high power laser and hot wire to improve tolerance to gap variance and control weld metal oxygen content. *Sci. Technol. Weld. Join.* **2013**, *18*, 314–322. [[CrossRef](#)]
11. Peng, W.; Jiguo, S.; Shiqing, Z.; Gang, W. Control of wire transfer behaviors in hot wire laser welding. *Int. J. Adv. Manuf. Technol.* **2016**, *83*, 2091–2100. [[CrossRef](#)]
12. Kujanpää, V.P.; Helin, J.P.; Moisio, T.J.I.; Bruck, G.J. Composition and Microstructure of Laser Beam Welds Between Dissimilar Metals. *J. Laser Appl.* **1990**, *2*, 24–30. [[CrossRef](#)]
13. Westin, E.; Stelling, K.; Gumenyuk, A. Single-pass laser-GMA hybrid welding of 13.5 mm thick duplex stainless steel. *Weld. World* **2011**, *55*, 39–49. [[CrossRef](#)]
14. Tsukamoto, S.; Zhao, L.; Sugino, T.; Arakane, G. Distribution of wire feeding elements in laser-arc hybrid welding. In Proceedings of the 26th International Congress on Applications of Lasers & Electro-Optics, Orlando, FL, USA, 29 October–10 November 2007; pp. 498–505.
15. Karhu, M.; Kujanpää, V.; Gumenyuk, A.; Lammers, M. Study of Filler Metal Mixing and Its Implication on Weld Homogeneity of Laser-Hybrid and Laser Cold-Wire Welded Thick Austenitic Stainless Steel Joints. In Proceedings of the 32nd International Congress on Applications of Lasers & Electro-Optics, Miami, FL, USA, 6–20 October 2013; pp. 252–261.
16. Zhao, L.; Sugino, T.; Arakane, G.; Tsukamoto, S. Influence of welding parameters on distribution of wire feeding elements in CO₂ laser GMA hybrid welding. *Sci. Technol. Weld. Join.* **2013**, *14*, 457–467. [[CrossRef](#)]
17. Sohail, M.; Karhu, M.; Na, S.-J.; Han, S.-W.; Kujanpää, V. Effect of leading and trailing torch configuration on mixing and fluid behaviour of laser-gas metal arc hybrid welding. *J. Laser Appl.* **2017**, *29*, 042009. [[CrossRef](#)]

18. Nima, Y.; Masoud, M.; Reza, R.; Radovan, K. Hybrid laser/arc welding of 304L stainless steel tubes, part 2—Effect of filler wires on microstructure and corrosion behaviour. *Int. J. Pres. Ves. Pip.* **2018**, *163*, 45–54.
19. Gook, S.; Gumenyuk, A.; Rethmeier, M. Hybrid laser arc welding of X80 and X120 steel grade. *Sci. Technol. Weld. Join.* **2014**, *19*, 15–24. [[CrossRef](#)]
20. Karhu, M.; Kujanpää, V. Solidification Cracking Studies in Multi Pass Laser Hybrid Welding of Thick Section Austenitic Stainless Steel, Part II Steels and Stainless Steels. In *Book Hot Cracking Phenomena in Welds III*, 1st ed.; Lippold, J., Boellinghaus, T., Cross, C., Eds.; Springer-Verlag: Berlin/Heidelberg, Germany, 2011; pp. 161–182. [[CrossRef](#)]
21. Kadoi, K.; Shinozaki, K. Effect of Chemical Composition on Susceptibility to Weld Solidification Cracking in Austenitic. *Met. Mater. Trans. A* **2017**. [[CrossRef](#)]
22. Lippold, J.C. *Book Welding Metallurgy and Weldability*, 2nd ed.; John Wiley & Sons, Inc.: Hoboken, NJ, USA, 2015; p. 14.
23. Kou, S. *Book Welding Metallurgy*, 2nd ed.; John Wiley & Sons, Inc.: Hoboken, NJ, USA, 2003; pp. 103–107.



© 2019 by the authors. Licensee MDPI, Basel, Switzerland. This article is an open access article distributed under the terms and conditions of the Creative Commons Attribution (CC BY) license (<http://creativecommons.org/licenses/by/4.0/>).

ACTA UNIVERSITATIS LAPPEENRANTAENSIS

831. KALLIOLA, SIMO. Modified chitosan nanoparticles at liquid-liquid interface for applications in oil-spill treatment. 2018. Diss.
832. GEYDT, PAVEL. Atomic Force Microscopy of electrical, mechanical and piezo properties of nanowires. 2018. Diss.
833. KARELL, VILLE. Essays on stock market anomalies. 2018. Diss.
834. KURONEN, TONI. Moving object analysis and trajectory processing with applications in human-computer interaction and chemical processes. 2018. Diss.
835. UNT, ANNA. Fiber laser and hybrid welding of T-joint in structural steels. 2018. Diss.
836. KHAKUREL, JAYDEN. Enhancing the adoption of quantified self-tracking wearable devices. 2018. Diss.
837. SOININEN, HANNE. Improving the environmental safety of ash from bioenergy production plants. 2018. Diss.
838. GOLMAEI, SEYEDMOHAMMAD. Novel treatment methods for green liquor dregs and enhancing circular economy in kraft pulp mills. 2018. Diss.
839. GERAMI TEHRANI, MOHAMMAD. Mechanical design guidelines of an electric vehicle powertrain. 2019. Diss.
840. MUSIIENKO, DENYS. Ni-Mn-Ga magnetic shape memory alloy for precise high-speed actuation in micro-magneto-mechanical systems. 2019. Diss.
841. BELIAEVA, TATIANA. Complementarity and contextualization of firm-level strategic orientations. 2019. Diss.
842. EFIMOV-SOINI, NIKOLAI. Ideation stage in computer-aided design. 2019. Diss.
843. BUZUKU, SHQIPE. Enhancement of decision-making in complex organizations: A systems engineering approach. 2019. Diss.
844. SHCHERBACHEVA, ANNA. Agent-based modelling for epidemiological applications. 2019. Diss.
845. YLIJOKI, OSSI. Big data - towards data-driven business. 2019. Diss.
846. KOISTINEN, KATARIINA. Actors in sustainability transitions. 2019. Diss.
847. GRADOV, DMITRY. Experimentally validated numerical modelling of reacting multiphase flows in stirred tank reactors. 2019. Diss.
848. ALMPANOPOULOU, ARGYRO. Knowledge ecosystem formation: an institutional and organisational perspective. 2019. Diss.
849. AMELI, ALIREZA. Supercritical CO2 numerical modelling and turbomachinery design. 2019. Diss.
850. RENEV, IVAN. Automation of the conceptual design process in construction industry using ideas generation techniques. 2019. Diss.
851. AVRAMENKO, ANNA. CFD-based optimization for wind turbine locations in a wind park. 2019. Diss.

852. RISSANEN, TOMMI. Perspectives on business model experimentation in internationalizing high-tech companies. 2019. Diss.
853. HASSANZADEH, AIDIN. Advanced techniques for unsupervised classification of remote sensing hyperspectral images. 2019. Diss.
854. POPOVIC, TAMARA. Quantitative indicators of social sustainability applicable in process systems engineering. 2019. Diss.
855. RAMASAMY, DEEPIKA. Selective recovery of rare earth elements from diluted aqueous streams using N- and O –coordination ligand grafted organic-inorganic hybrid composites. 2019. Diss.
856. IFTEKHAR, SIDRA. Synthesis of hybrid bio-nanocomposites and their application for the removal of rare earth elements from synthetic wastewater. 2019. Diss.
857. HUIKURI, MARKO. Modelling and disturbance compensation of a permanent magnet linear motor with a discontinuous track 2019. Diss.
858. AALTO, MIKA. Agent-based modeling as part of biomass supply system research. 2019. Diss.
859. IVANOVA, TATYANA. Atomic layer deposition of catalytic materials for environmental protection. 2019. Diss.
860. SOKOLOV, ALEXANDER. Pulsed corona discharge for wastewater treatment and modification of organic materials. 2019. Diss.
861. DOSHI, BHAIRAVI. Towards a sustainable valorisation of spilled oil by establishing a green chemistry between a surface active moiety of chitosan and oils. 2019. Diss.
862. KHADIJEH, NEKOUEIAN. Modification of carbon-based electrodes using metal nanostructures: Application to voltammetric determination of some pharmaceutical and biological compounds. 2019. Diss.
863. HANSKI, JYRI. Supporting strategic asset management in complex and uncertain decision contexts. 2019. Diss.
864. OTRA-AHO, VILLE. A project management office as a project organization's strategizing tool. 2019. Diss.
865. HILTUNEN, SALLA. Hydrothermal stability of microfibrillated cellulose. 2019. Diss.
866. GURUNG, KHUM. Membrane bioreactor for the removal of emerging contaminants from municipal wastewater and its viability of integrating advanced oxidation processes. 2019. Diss.
867. AWAN, USAMA. Inter-firm relationship leading towards social sustainability in export manufacturing firms. 2019. Diss.
868. SAVCHENKO, DMITRII. Testing microservice applications. 2019. Diss.



ISBN 978-952-335-416-6
ISBN 978-952-335-417-3 (PDF)
ISSN-L 1456-4491
ISSN 1456-4491
Lappeenranta 2019